



**COLD ROLLED TEXTURE
OF
LOW CARBON BCC STEEL**

MASTER OF ENGINEERING (1999)
(Mechanical Engineering)

McMaster University
Hamilton, Ontario

TITLE: **The Development of Texture at Intermediate Stages of
Cold Rolling in Low Carbon Steel.**

AUTHOR: **Ken Shaw, B.Sc. (University of Toronto), B.Eng.
(McMaster University)**

SUPERVISOR: **Professor R. Sowerby**

NUMBER OF PAGES: **iv, 116**

Abstract

Much of the literature on cold rolled texture focuses on the various textures that are present after a standard amount of cold roll reduction, usually 70-90 %. Also mentioned is the effect that total cold roll reduction has on the final cold roll texture. However, very little investigation has focused on the development of texture at various intermediate stages of cold roll reduction. This thesis describes the texture evolution during the cold rolling of two commercial steels that are used extensively in stamping operations. The cold rolling mill was a 5 stand, 4 high continuous mill located at Dofasco Steel Inc. in Hamilton, Ontario. The author at the time was in a position to have the mill stopped, and have samples cut from the strip at the entry and exit to the mill and also between each roll stand. This was done on six occasions, three times each for each of the two different steels. The samples were prepared for metallographic examination in a diffractometer, and pole figures were generated using software supplied by Los Alamos Research Laboratories, New Mexico. The pole figures defined how the texture evolved as the steel strip progressed through the mill. The Los Alamos software also enabled crystallite orientation distribution functions (CODF's) to be generated. Amongst other things the CODF allows textures to be described in terms of the dominant ideal crystallographic orientations. In turn these ideal orientations were qualitatively related to the level of the normal anisotropy parameter (\bar{r}) in recrystallized samples of the two steels. The \bar{r} -value has been used extensively in the steel industry as a measure of formability, in particular the deep drawability. The experimental results from this investigation are generally in agreement with published work that has modelled the texture evolution in cold rolled, low carbon steels.

Acknowledgements

Much gratitude is given to Prof. R. Sowerby of McMaster University whose contribution to this thesis is immensely appreciated and whose patience over the years taken to write it is without limit. Thanks also to Dofasco's Research department, in particular Ivan Fernandez, for providing the time and expertise to obtain the data on which this thesis stands.

Table of Contents

Chapter 1 – Introduction

Chapter 2 – Literature Review

Chapter 3 – Procedure

Chapter 4 – Data/Experimental Results

Chapter 5 – Discussion of Results

Chapter 6 - Conclusions

Bibliography

Appendix A - Euler angles versus Miller indices

Appendix B - Raw data, 2 of the 6 sets.

Chapter 1 - Introduction

1.1 - Steel Texture

For many years now it has been accepted by academics that the crystalline orientation of grains, or texture, plays a significant role in determining how steel responds to manufacturing processes. As well, for years now, academics have also suggested how the manufacturing of steel can be adjusted to achieve a desired texture that will facilitate further value-added manufacturing processes such as steel forming and stamping. However, there has always been a significant gap between the controlled conditions of the academic laboratory and the not so very pristine, not so very controlled conditions of the shop floor. Until recently (late 1980's), maintaining correct manufacturing conditions to achieve an optimum texture, had a lower priority for the plant manager than maintaining more important mechanical properties such as correct yield strength or correct dimensionality.

It would be wise here at the onset to first define what we mean by texture. When this thesis refers to texture, it is referring to the sub-surface texture defined by the preferred three dimensional orientation of the individual grains that make up the polycrystalline steel solution. This texture develops during solidification of the molten steel. The process of solidification occurs by a mechanism of nucleation and growth, i.e. minute nuclei, or seed crystals, are formed in various parts of the melt which then grow at the expense of the surrounding liquid until the whole volume is solid. During the freezing process the nuclei grow more rapidly along certain crystallographic directions, and this results in the formation of long branch-like crystals known as dendrites. Eventually the outward growth of a dendrite is halted when contact is made with neighboring growths and then the remaining liquid freezes in the interstices between the dendrite arms. Every contact surface then becomes the boundary between two crystals, so that each original nucleus produces a crystal or grain of its own, separated from the neighboring grains by grain boundaries. The grain boundary is simply a narrow transition region, of a few atom diameters width, in which the atoms adjust from the crystal orientation of the one grain to that of the other [10]. After solidification from the melt the orientation of these crystals (grains) is predominately random. Consequently, the steel is considered to have no texture. The steel, however, undergoes further processing.

It is hot rolled where grains are both broken down and re-grown at the same time. There is a quench where the cubic crystals transform from Face Centered Cubic (FCC) to Body Centered Cubic (BCC). There is cold rolling where the grains are broken down, and there is annealing where the grains are allowed to re-crystallize. All these operations contribute to a statistical preference of the individual grains for certain orientations. The steel is then considered to have texture.

1.2 – The Importance of Texture

If steel has texture then it is anisotropic. To appreciate this, consider a multi-layered cubic crystal. The atoms of this cubic arrangement lie on different crystallographic planes, {100}, {110}, {111}, {211}, etc. The distance between consecutive {100} planes is not the same as the distance between consecutive {110} planes or {111} planes, etc. The critical shear stress that is required for one plane to slip across another plane is inversely proportional to the distance that separates the planes. Hence there are preferred slip planes for each metal. In heavily textured metals these planes will be aligned (rather than randomly orientated), and therefore their orientation with respect to some externally applied load (and hence stress) will dictate the magnitude of load to cause slip. The magnitude of the load could be either higher or lower than the corresponding load to cause slip in a randomly orientated (isotropic) sample.

Anisotropy also manifests itself in the resulting strain distribution in a deformed metal. For example, consider cutting a tensile specimen from the plane of a sheet of metal. It might be anticipated that during the course of a tensile test the width and thickness strains would be the same i.e. the material is isotropic. However in many instances the strains are different and this provides a mechanical means of defining the degree of anisotropy, as described in the next section. At the same time it reveals how anisotropy might be used to enhance a manufacturing process. If the material shows a resistance to thinning i.e. the thickness strain is less than the width strain, such a property would be beneficial in stamping operations that require considerable deep drawing e.g. automobile oil pans. In other words deeper draws could be obtained in a single stage operation without excessive thinning of the material.

1.3 – How Texture is measured

The example just given is a very common application of steel anisotropy, i.e. comparing the ease of straining in the plane of the steel sheet with the ease of straining in the through-thickness direction. For

this reason a standard means of quantifying the degree of anisotropy is the “plastic strain ratio” or more simply, “r-value”. It is defined as

$$r = \frac{\text{natural width strain}}{\text{natural thickness strain}}$$

and measured from tensile tests on specimens cut at different orientations from the plane of a rolled sheet. A practice that originated in the steel industry is the definition of two quantities based on the measured r-values. One is the so called “normal anisotropy” defined by

$$\bar{r} = \frac{1}{4} (r_0 + r_{90} + 2r_{45})$$

where a high \bar{r} value has been shown to be desirable for improved deep drawability. In the above r_0 , r_{45} , and r_{90} represent the r-values as measured from tensile specimens cut at 0, 45, and 90 degrees with respect to the rolling direction of sheet. The second anisotropic parameter is termed “planar anisotropy” and defined by

$$\Delta r = \frac{1}{2} (r_0 + r_{90} - 2r_{45})$$

It indicates the “ear” formation in a cupping test i.e. the deep drawing of cylindrical cups from circular blanks. All steels show four fold symmetrical earing. If $\Delta r \approx 0$ then drawn cups are flat topped, but if Δr is positive ears form in the 0 and 90 degree directions while ears form in the ± 45 degree directions if Δr is negative. In commercial steel stampings it seems to be of little concern whether Δr is positive, negative, or zero. In deep drawing quality steels \bar{r} tends to be between 2 and 3, but at the same time these steels show marked earing.

Another means of measuring the amount of anisotropy is, of course, to measure the intensity (i.e. the population presence) of various crystallographic orientations. This is done using crystallographic methods and aided by computer analysis. The results are presented either in the form of pole figures or crystallite orientation distribution functions (CODF's). These will be explained further in Chapters 2 and 3.

1.4 - Effect of Texture

The global market and its associated increased competition have caused much social and economic upheaval. The steel industry has had to respond. An example is the automobile/steel industry partnership. The 1990's have introduced a new phrase to the above partnership: “full service suppliers”.

The vehicle manufacturers are no longer interested in just buying steel with correct mechanical and dimensional properties from the steel manufacturer. They are now looking to enter into partnerships with "value added" material providers. One such "value added" commodity that the steel company now provides to the auto industry is computer simulation of various metal forming processes, such as stamping and hydro-forming.

The "engine" underlying the computer simulation is the Finite Element Method (FEM). The FEM divides the automobile part into a grid of "elements" which form a model of the real structure [27]. Each of the elements is a simple shape such as a triangle, rectangle, or cube. To each of these elements, the finite element program applies information regarding the mechanical properties of the material, thereby generating the governing equation for the model in the form of a stiffness matrix. Included in this information is some representation of the yield surface for the steel. The FEM will assemble the stiffness matrices for all the elements to form the global stiffness matrix for the entire model. This stiffness matrix is solved for the unknown plastic strains, given the known press forces and tool/die boundary conditions. Depending on whether the FEM is "extrinsic" or "intrinsic" determines if the final strain is solved for in one strain step or a number of small strain steps.

It is beyond the scope of this thesis to discuss the various FE formulations. However a basic requirement for the formulations is a model that will adequately describe the yielding behavior. For isotropic metals it is often assumed that the material yields in accordance with the von-Mises criterion. For anisotropic metals a model proposed in 1948 by Hill [34] has been widely employed. The model is an extension of the von-Mises yield criterion, and in its simplest form embodies a single r -value to describe the state of anisotropy i.e. the material is assumed to be planar isotropic but to possess normal anisotropy. Many other anisotropic yield functions have been proposed, a popular model is due to Hosford [35] (see also the book by Hosford and Caddell [36]). In its simplest form this is also an extension of the von-Mises criterion and embodies a single r -value but assumes a non-quadratic function of the stresses. More recently a model due to Barlat and his co-worker [37] has gained favor. In the general case this model embodies a number of different parameters in the yield function, each of which can exert a strong influence on the shape of the yield locus. It is the shape of the yield locus that is of paramount importance in any FE solution, since the shape dictates the calculated strain evolution. Regardless of the yield criterion adopted,

more often than not the yield model is assumed with little or no experimental justification of its applicability.

1.5 - Investigation of Texture

To provide the full service expected of it by the automotive industry, the steel company must now have a due respect for steel texture. Consequently, plant managers must now recognize that texture is a significant characteristic of steel and as well, recognize and appreciate the various components of the steel making process that influences texture development.

Focus on texture development within the steel manufacturing process is typically confined to the recrystallization that occurs during the annealing stage subsequent to cold rolling. The final orientation of the crystalline lattice is very dependent on the re-crystalline conditions. However, it has been shown by many researchers [1,18,24,25,26], that the post cold rolling texture going into the re-crystalline phase has significant effect on the final texture.

Much of the literature on cold rolled texture focuses on the various textures present after a standard amount of cold roll reduction, usually between 70-90 %. They also mention the effect of total cold roll reduction on the final cold roll texture. However, very little investigation has focused on the development of texture at various intermediate stages of cold roll reduction. This writer had the opportunity to request that a cold mill be stopped in a controlled manner as it cold reduced flat steel strip. Steel samples could then be taken from between each of the cold mill stands (refer to chapter 3 for details), then sent to the laboratory and analyzed in the x-ray diffractometer. These results form the basis of this thesis that investigates the development of texture at intermediate stages of cold rolling under commercial, production conditions. Chapter 2 provides a selected literature review focusing on the nature of deformation in single crystals, the nature of deformation in polycrystalline structures, and the stability of the crystallite orientation within the polycrystalline structure. Chapter 3 describes the cold rolling mills that were used for this investigation, the conditions under which the investigation was run, as well as the preparation of the steel samples and the process for the determination of the textures.

Chapter 4 is an attempt to present the results of the investigation in as graphic a manner as possible in the form of 3-dimensional column charts. Examples of the actual pole figures and CODF's can be found in Appendix B. Chapter 5 is the discussion in which, it is hoped, some cause and effect will be

determined between cold rolling and texture development. Finally, Chapter 6 itemizes the conclusions developed by this investigation and suggests a number of areas for future work.

Chapter 2 - Literature Review

Much of the current knowledge on cold worked textures arose in the 1930's [19, 20, 21, 22], after the value of X-ray diffraction (as well as the important Bragg relationship, $\lambda = 2d \sin(\delta/2)$ ¹) in the study of crystal structures was established in the 1920's. These investigators borrowed the "pole figure" method used in crystallography to represent crystal symmetry, and established it as a valid method to investigate the discrete orientations of the crystallites of deformed metals.

2.1 – Pole Figures

A pole figure is a stereographic projection which shows the variation in density of a plane normal (or pole) with orientation for a selected set of crystal planes. Intensities are plotted as multiples of the intensity expected from a randomly oriented specimen [7]. One disadvantage of the pole figure is that it gives information only about the distribution of plane normals but does not contain information about rotation around these normals. A pole figure from one of the samples tested will be shown in chapter 3 (section 3.3.1) and various features will be discussed.

2.2 – CODF's

In this section on CODF's considerable reference has been made to Sowerby, et al, p.26 [7]. They have noted that it is clear that three angles are required to fully describe the orientation of a crystallite with respect to a physical reference frame. This is shown in Appendix A where the orientation is specified by the Euler angles ψ , θ , and ϕ with respect to the specimen axes. In rolled sheet the most obvious choice of axes is the normal, transverse and rolling directions. The crystallite orientation distribution function (CODF) expresses the probability that a crystallite has the orientation described by the Euler angles. For cubic crystals, Roe [17] and Bunge [28] independently proposed a general method of solution for obtaining the CODF from a limited number of conventional pole figure distributions. The resulting CODF can be

¹ Where λ is the wavelength of the x-ray source, d is the distance of separation between successive crystallographic planes, and δ is the angle between the incident beam and the normal to the plane.

represented graphically by plotting the probability that a crystallite has a given orientation in Euler space and taking constant sections of one of the Euler angles, most usually constant ϕ sections. Ideal orientations $(hkl)[uvw]$ (refer to Miller indices in the following section) are represented as single points in each of these sections and charts can be prepared to facilitate the interpretation of the resulting CODF's [2]. The CODF provides a powerful tool to accurately track the development of texture from the random hot rolled state to the discrete orientations of the anisotropic cold rolled state.

2.3 – Miller Indices

The standard method to describe a crystallographic plane or direction is by referring to the Miller indices for the plane or direction in question. It may be helpful then to provide a brief explanation of these indices. For this explanation I have referred to Smallman, pp. 19-20 [10]. The Miller index system is a notation in which three axes, X, Y and Z are chosen, parallel to the three edges of the crystal cell. To specify a crystal plane it is necessary to determine its intercept on the three axes X, Y and Z, then take the reciprocals of these intercepts and multiply out the common denominator, say "n". The reciprocal of the intercept will be in the form $h/n, k/n, l/n$, so that when the integers hkl are enclosed in brackets, they give the Miller indices of the plane (h, k, l) .

The indices (123), for example, or more generally (hkl) , represent not only that plane for which the values of h, k and l have been determined, but the whole family of planes parallel to this particular one. Often it is necessary to specify all planes of a given crystallographic type, e.g. all the cube faces, not merely those parallel to (100) and this is indicated by enclosing the indices obtained in the usual way in different brackets. Thus the class of all cube faces is denoted by $\{100\}$, which includes (100), ($\bar{1}00$), (010), (0 $\bar{1}0$), (001), and (00 $\bar{1}$) respectively; the over-bar defines a negative direction.

To define a direction it is necessary to construct a line through the origin parallel to the required direction, and then to determine the co-ordinates of a point on this line in terms of lengths of cell edges. The co-ordinates found in this way are then reduced to whole numbers, and to distinguish these indices from those given to the planes they are enclosed in square brackets. For example, if the co-ordinates are $X=a, Y=-2a, Z=a/3$ (where "a" is a cell length), the line is a $[3\bar{6}1]$ direction. Again, to specify all directions of a given crystallographic type, the indices are enclosed by a different set of brackets. Thus to

indicate all directions parallel to the crystallographic axes (i.e. [100], [100], [010], [010], [001], and [001]), it is sufficient to designate them as $\langle 100 \rangle$.

To distinguish a specific direction on a crystallographic plane one combines the above two sets of indices as follows. To focus on the [110] direction on the (001) plane, it is referred to as (001)[110]. The general designation for a direction on a plane is $(hkl)[uvw]$. To refer to the set of equivalent crystallographic directions and planes, the designation $\{hkl\}\langle uvw \rangle$ is used.

It is useful to note that for a cubic system the Miller indices for a plane are also the Miller indices for the direction of the normal to the plane. This is useful when one wants to determine if a specific direction lies within a certain plane. If the mathematical dot product (also known as the cosine product) is taken between the Miller indices of the direction in question with the plane in question, and if the result is zero, then that specific direction does indeed lie within that plane.

2.4 - Nature of deformation in individual grains

A start at understanding plastic deformation of metal is to first examine a single crystal. It is well known that here the main mechanism is a simple shear parallel to certain crystallographic planes and in a particular direction [7]. Three well-established laws govern slip behavior within individual crystals: (i) the direction of slip is almost always that along which the atoms are most closely packed, (ii) slip usually occurs on the most closely packed plane, (iii) from a given set of slip planes and directions, the crystal operates on that system (plane and direction) for which the resolved shear stress is the largest [10]. According to Schmid's law for yielding in a single crystal, slip will occur on the system that first achieves the critical value of resolved shear stress, τ^* . In a rod-shaped crystal under uniaxial tension σ , by stress transformation, $\tau = \sigma \cos(\phi) \cos(\lambda)$. Here ϕ and λ are the angles made by the slip plane normal and the slip direction respectively with the rod axis. Hence σ has to be increased (to some yield value σ_y) until the critical stress τ^* is achieved on the active system according to the above equation. The ratio σ_y / τ^* is known as the Schmid factor and clearly the quantity will depend on the orientation of the tensile axis with respect to the crystal structure [16].

Backofen [18] has extended Schmid's law for a single crystal and has applied it for a number of stress components. A "generalized" statement of Schmid's Law can be developed in which the shear stress

resolved on each slip system is given in terms of all applied stress components. One needs only to apply the Generalized Schmid Law to derive yield loci for various textures.

It must be noted that from experiments with single crystals, although the resolved shear stress is a maximum along lines of greatest slope in planes at 45° to the tensile axis [10], slip occurs preferentially along certain planes and directions. Thus to determine active slip systems one must first need to know the set of potentially active slip systems, then apply Schmid's Law only to this subset of slip systems.

Hatherly and Hutchinson [4] believe that theories on rolling texture development can be divided into two camps based on assumptions made concerning the nature of deformation in single crystals. The "imposed stress approach" or Sachs model holds that the crystal deforms on the slip system that has the largest resolved shear stress as described above. It does this without regard for the resulting shape change, or more importantly, without regard to the imposed shape restrictions. Sach's model provides a lower bound solution [13] to plastic deformation.

A different approach is the "imposed strain" theory or Taylor model, first described in 1923 [39]. F. Wever [20] is a proponent of this latter theory. The extension or compression of a single crystal by applied stress produces an alteration in the external shape. This does not necessarily conform to the change in shape produced by slip along the slip system bearing the largest resolved shear stress. This causes moments to develop which tend to rotate the active slip systems into the direction of flow of the metal caused by the external change in shape, i.e. the external shape deformation produces rotations in the crystal. Taylor's model provides an upper bound solution.

Dillamore and Kato [11] have made some calculations comparing the two models by predicting texture development for BCC metals, assuming pencil glide² as the mode of deformation. Their results provide greater support for Taylor's model than Sach's model and it is generally agreed that the former can be regarded as the more realistic of the two.

2.5 - Nature of deformation in polycrystalline structures

Clearly, the situation becomes more complex when a polycrystalline matrix is considered.

² Pencil glide refers to slip systems that operate by $\{hkl\}[111]$. It is the well defined close packed slip direction for BCC metals.

Specifically, inclusions and the influence of grain boundaries and the constraints imposed on individual grains by its neighbors are unknown. Wever [20] made the following propositions for the behavior of any crystallite in a polycrystalline aggregate that is subjected to a macroscopically homogenous deformation:

- 1) Those slip planes and directions of slip are selected for which the shearing stress is a maximum with respect to the external forces impressed.
- 2) The crystallite will rotate about an axis that is in the plane of slip, perpendicular to the direction of slip, and in a direction that will lessen the angle between the direction of flow of a particle and that of the next adjacent particle.

Taylor [14] made the assumption that within a polycrystalline structure that must accommodate a forced change in shape, all the crystals must undergo the same shape change by operation of at least five slip systems (it is to be noted that for incompressible flow an arbitrary imposed shape change requires, in general, the operation of five independent shears from all possible operative slip systems [7]).

2.6 - Slip systems available to BCC metals

Taylor [14] assumed that plastic deformation in BCC crystals was effected by slip on the $\{110\}\langle 111 \rangle$ system, and each grain within the aggregate undergoes the same strain. This assumption of uniform straining of each crystal ensures cohesion of the aggregate but ignores stress continuity across the grain boundaries. As mentioned above, it is generally agreed [9,10] that for a BCC lattice, the observed slip direction is $\langle 111 \rangle$ or "pencil glide". The slip plane most commonly observed is $\{110\}$ but there is also evidence that $\{112\}$ and $\{123\}$ are slip planes [10]. It can be seen there is no shortage of available slip systems to satisfy any imposed shape change. The problem lies in identifying the operative slip system, i.e. the slip system that actually operates when the metal deforms.

As stated above, Taylor [14] assumed that plastic deformation occurred by slip on the $\{110\}\langle 111 \rangle$ system. Therefore based on Taylor's model one must select 5 out of 24 possible systems, i.e. four possible planes each with six possible directions (actually three directions but doubled to include the negative and positive sense).

A model for plastic deformation based on Taylor's hypothesis must select at least 5 out of 24 possible slip systems. Taylor [14] hypothesized that the actual set of active glide shears is that in which their absolute sum is a minimum. The most common means of selecting between these available slip

systems is that pioneered by Taylor and that is to minimize the sum of their shear strains. Although the possible combination of slip systems can be staggering, computers can be used to arrive at a solution of deformed orientation. In a subsequent investigation Bishop and Hill [38] simplified Taylor's approach for finding the possible slip systems.

2.7 - Stability of Orientations

As with all natural processes, plastic deformation will tend towards a level of maximum stability. Slip directions in a deforming crystal rotate toward the axis of extension, whatever the shape change being imposed [18]. They seldom reach it, because eventually two or more of them become symmetrically oriented around the axis. At that point their rotations tend to cancel and the pattern they are in tends to become fixed. The stability of this pattern can be determined by looking at the Schmid factor for each of the crystal systems. Their sum will be a minimum, otherwise one or more systems will slip in order to achieve a minimum energy state. Consequently, one can assume that for a texture to be stable, it will accommodate an imposed shape-change and simultaneously position slip directions as close as possible to the axis of extension [18].

For illustration, Backofen [18] has generated a table, refer to Table 2.1 below, for cubic metals that lists the angles between ideal texture axes and slip directions.

Table 2.1

Structure	Slip direction	Axis		
		{111}	{100}	{110}
FCC	110	~33°	45°	60°
BCC	111	~70°	~54°	~33°

For BCC metals undergoing pencil glide under uni-axial tension, where texture orientation is considered relative to the axis of tension, a consideration of the angles would indicate that the stable oriented texture is [110]. In flat strip rolling where by convention, texture axes are considered relative to the normal to the plane of the strip, the extension axis is at right angles to the texture axis, so that the stable orientations are now [111] and [100].

In a polycrystalline material of initially random orientation, this predisposition to rotate towards the axis of extension would lead to textures that are symmetric around this axis. This phenomenon has led

to the term fiber textures. Some of the more practical fibers have been given designations as shown in Table 2.2 [6] where || RD and || ND mean parallel to the rolling direction and normal direction respectively.

Table 2.2

Fiber	Axis
α	$\langle 110 \rangle$ RD
γ	$\langle 111 \rangle$ ND
ζ	$\langle 110 \rangle$ ND
η	$\langle 001 \rangle$ ND

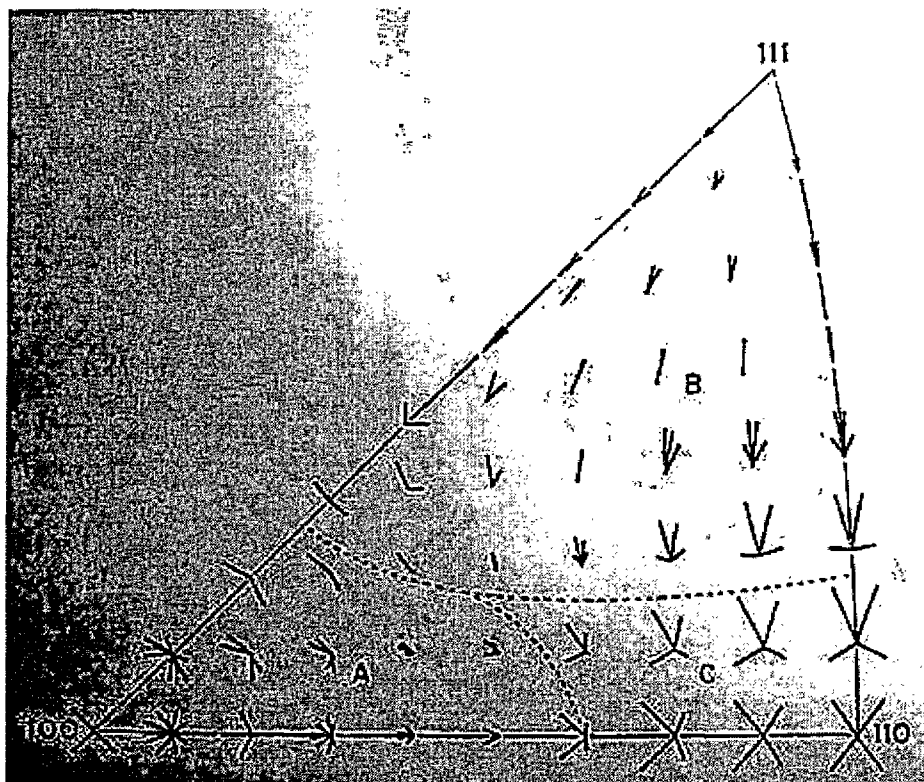
To conclude this section, and as a point of reference for comparative purposes, a number of investigators [1,4] have found that the commonly observed cold roll textures found for BCC metals are $\{100\}\langle 011 \rangle$, $\{111\}\langle 011 \rangle$, as well as $\{211\}\langle 011 \rangle$ and $\{111\}\langle 112 \rangle$. As will be discussed in subsequent chapters, it is not surprising that this investigation also observed the same cold roll textures. It should also be noted that no investigators, at least none encountered by this writer, have compared the cold roll texture that arises from one large, 70-80 % reduction step to the cold roll texture that arises from 4 or 5 smaller steps of approximately 30 % reduction.

2.8 – Modeled Cold Roll Textures

As mentioned above, Taylor [14] proposed a method whereby from a given crystallite orientation and a given imposed shape change, the resultant orientation can be predicted. Taylor's original paper was published in 1923, a time when the use of computers was not exactly wide spread. Going through all the calculations to find the minimum sum of the shear strains for any five of all possible slip systems, and then to repeat these calculations for each incremental shape change would be very intimidating. The use of computers has, naturally, reduced this task to a matter of seconds. An excellent early paper written on this topic is that by Chin et al [29]. The results of their computer calculations based on Taylor's theory are shown by the use of lattice rotation vectors. These vectors indicate the lattice rotation whereby the ends of the vector correspond to the positions before and after a given deformation. The different vectors emanating from a given orientation represent different combinations of five slip systems that satisfy Taylor's minimum shear criterion. Figure 2.1 from Chin's paper shows the results for $\{110\}\langle 111 \rangle$ slip

after 5 % axisymmetric compression, for fifty-two axial orientations distributed at 5 degree intervals throughout the standard stereographic triangle.

Fig. 2.1



This pattern of lattice rotation may be divided into three regions: region A in which the rotation is toward $[100]$; region B, toward $[111]$, and region C, toward either $[100]$ or $[111]$. Although some slip combinations in region C lead to $[110]$, the latter is not stable as continued activity of the same combinations will eventually move the axis toward $[100]$ or $[111]$. It can also be noted from the figure that $[100]$ is also not stable. However, close inspection of the vectors in region A shows that it is impossible for an axial orientation within A to rotate outside its boundary. Hence after heavy compression, all orientations

from A and some from C are expected to form a diffuse band in the [100] vicinity. By far the largest region is B. Here all orientations rotate to [111], which is a truly stable position. Thus the [111] texture component is expected to be rather sharp.

A more recent development in modeling texture change is the use of CODF's. A paper by Kestens and Jonas [5] illustrates the use of CODF's in the prediction of texture development during the recrystallization of the annealing stage. Keep in mind that the CODF is a graphical means of indicating the probability of finding a particular crystal orientation in three dimensions. The procedure is as follows. A sample of cold rolled material is obtained large enough to contain a representative number of crystallites (i.e. a 1000 or more). The CODF is obtained for the sample in the standard manner with a x-ray diffractometer and the associated software required to combine the obtained pole figures into a three dimensional composite. The information obtained from the CODF has effectively "discretized" the sample, i.e. what was approximately 1000 individual orientations is now "generalized" into fewer predominant or fundamental orientations (eg. orientations of $(\bar{1}01)$ [313], $(\bar{1}01)$ [212], and $(\bar{1}01)$ [$\bar{3}23$] would be considered as $(\bar{1}01)$ [212]). Once the sample anisotropy has been discretized, an incremental shape change is imposed (i.e. the incremental plastic strain components), and the predicted operative slip system identified. This incremental deformation and the resultant slip system causes the crystallite to rotate to a new predicted orientation. The whole procedure is repeated with a new set of five slip systems being identified and the incremental rotation of the crystallite calculated. This process is stopped when the desired level of deformation has been imposed. The discrete crystallites in their final rotated positions are then re-assembled to produce the CODF that illustrates the predicted texture of the deformed material.

Chapter 3 - Procedure

3.1 - Substrate

On six different occasions, the mill was stopped and samples taken at the entry to the mill (i.e. the hot band substrate), from between each of the stands, and at the exit from the mill. On three of the occasions the substrate was standard low carbon, Al-killed steel and on the three other occasions the substrate was IF, Ti-stabilized steels. Both types of material are used extensively in stamping operations due to their favorable formability characteristics. Formability increases with decreasing carbon content due to a decrease in the cementite content and the presence of a more favorable condition for grain growth. The essential difference between the two steels is the amount of carbon. The IF, Ti stabilized steel started out as standard Al-killed, low carbon steel but then underwent further processing. It was passed through a vacuum degasser that basically "sucked" out free carbon. Titanium was then added to further remove any free carbon from solution. The result is a solid solution in which the carbon content is so low as to be almost undetectable. Table 3.1 lists the chemical composition of the substrate used for the six trials.

Table 3.1

Trial #	Steel Type	C	Mn	Al	N	Cb	Ti
1,3,6	Al-killed low carbon	.045-.065	.20-.35	.02-.06	.008	.003	.01
2,4,5	Ti-IF	.004	.15-.20	.02-.06	.005	.005-.01	.05-.06

Steel companies maintain tight tolerances on the chemical composition for each steel heat, so the substrate used for trials 1,3, and 6 would be very similar, as also for trials 2,4,and 5. The cost difference between the two types of steel is approximately \$4.25 /cwt (i.e. per 100 lbs).

3.2 – Rolling Mill

The mill that was used for this investigation is the tandem 5 stand, 4 high, continuous, cold roll mill located at Dofasco Steel in Hamilton, Ontario. As early as 1931 Wever [20] suggested that the final

texture of the cold rolled material may be affected by such factors as the roll diameter, the reduction per pass, the number of passes, etc.. Gensamer and Mehl [21] refer to a paper by Sisson [23] in which Sisson's work seems to have shown conclusively that tension applied during rolling does not affect the degree or type of orientation developed. It had been hoped for the current investigation that opportunity would arise during the trials to investigate the affect, if any, of changing interstand tension on the final texture or on the rate of development of texture. Circumstances did not allow for this avenue of investigation. Due to the harsh realities of low inventories and back-orders, time did not allow for any deviation from standard rolling practices to perform mill trials. Consequently, a standard rolling schedule was adhered to for the three sets of Al-killed low carbon samples, and a second standard rolling schedule was adhered to for the three sets of Ti-stabilized, IF samples (refer to Table 3.2).

Table 3.2

	Entry Gauge (mm)	Reduction pattern (%)					Delivery Gauge (mm)	Tension pattern (ksi)					
Al-killed Low carbon	2.29	34	34	34	34	30	.280	5.7	22.7	22.7	22.7	22.7	11.4
Ti-stabilized IF	3.81	32	32	32	32	2	.826	5.4	15.6	15.6	15.6	15.6	10.7

These rolling schedules were derived strictly from a consideration of steel substrate limitations, mill limitations and flat strip dimensional control. Mill limitations (eg. maximum allowable vertical force, or maximum allowable motor torque), limit the amount of reduction that any one stand can accomplish. While dimensional control (eg. cold roll gauge, and degree of flatness), limit the amounts of reduction each stand can perform relative to the other four stands. The amount of strip tension between each stand is a compromise between the desired reduction in vertical force required on a stand (for a given amount of reduction, increasing interstand tension reduces the amount of vertical force required), and the tensile point of the steel. All these constraints result in a narrow allowable range in a rolling schedule.

A modern rolling mill has sophisticated closed loop computer control to maintain the various preset rolling mill conditions (i.e. gauge, force, torque, tension, shape, etc.). The Dofasco cold roll mill used for this investigation was state-of-the-art, with 20 process computers, 18 Programmable Logic Controllers (PLC's), and three Local Area Network's (LAN's). Any control system, no matter how sophisticated, is only as good as the sensors that provide it with critical feedback information. The Dofasco

mill has load cells on each stand to measure vertical force, tensiometers between each stand to measure tension, a total of four thickness gauges (both x-ray and γ -ray) at various locations along the tandem mill, a shape meter at the exit of the mill, and tachometers on each stand to measure rpm's. To implement the changes to the mill required by the control systems, each stand has hydraulic screwdowns rated at 100 rad/s¹ while the main drive motors had 60 rad/s response times.

Another significant difference between the two rolling schedules is that the Ti-stabilized IF substrate was rolled to gauge with only 4 of the 5 mill stands. The fifth stand had matte work rolls that did negligible reduction and only imprinted a matte finish onto the surface of the strip. The Al-killed low carbon substrate was rolled to gauge using all 5 stands (i.e. the fifth stand had the regular, bright finish work rolls). The use of the matte rolls was again dictated by market conditions. During the period in which the trials were run, the customer demand for IF steel with the appropriate gauge included a requirement for the rough surface texture that can only be generated by rolls with a matte finish. This difference of 4 stand rolling versus 5 stand rolling will unfortunately lead to some ambiguity in the conclusions that are reached in chapters 5 and 6.

For all 6 trials, standard work roll diameters were used. The ranges of work roll diameters allowed for each stand can be seen in Table 3.3,

Table 3.3

Stand	1	2	3	4	5
w.r. dia. range (mm)	480-522	522-542	498-527	494-545	495-527

3.3 – Trials

Coupons were punched from the samples using dies that do not affect the crystalline structure (this had been verified in the past). The coupons were then polished down to a 1000 grit using an automatic polisher and SiC paper and lightly etched in 2% Nital. The pole figures were obtained from a 50 kW, 200 mA Rigaku Diffractometer using a Mo x-ray source (wavelength, 0.7093 angstroms). The diffractometer generated the (200), (211), and (110) pole figures using software obtained from the Los Alamos National Research laboratories and installed on a Dofasco Research department computer. These three pole figures

¹ Where rad/s refers to the angular velocity in radians per second. Divide by 2π to get cycles/sec which is the frequency of the fastest signal that this controller can follow.

were in turn combined by the same software to generate the (111) pole figure. (Note that due to the limitations associated with Bragg's relationship and the given wavelength of the x-ray source it is not possible to generate a pole figure for all crystallographic planes.) From the appropriate pole figure, the intensity of the associated plane was obtained, eg. from the (111) pole figure the intensity at the center was read to determine the intensity of the {111} planes.; similarly for the {110} and {211} set of planes. For the {100} set of planes, the (200) pole figure was used. The two are comparable orientations for the purposes of this investigation. These data were then put into tabular form per amount of cold roll reduction (refer to chapter 4).

3.3.1 – Pole Figures

Figure 3.3.1.1 contains a pole figure from one of the tested samples. It is shown here to illustrate various features of a pole figure. The first observation is the difference between the "raw" incomplete pole

Fig. 3.3.1.1

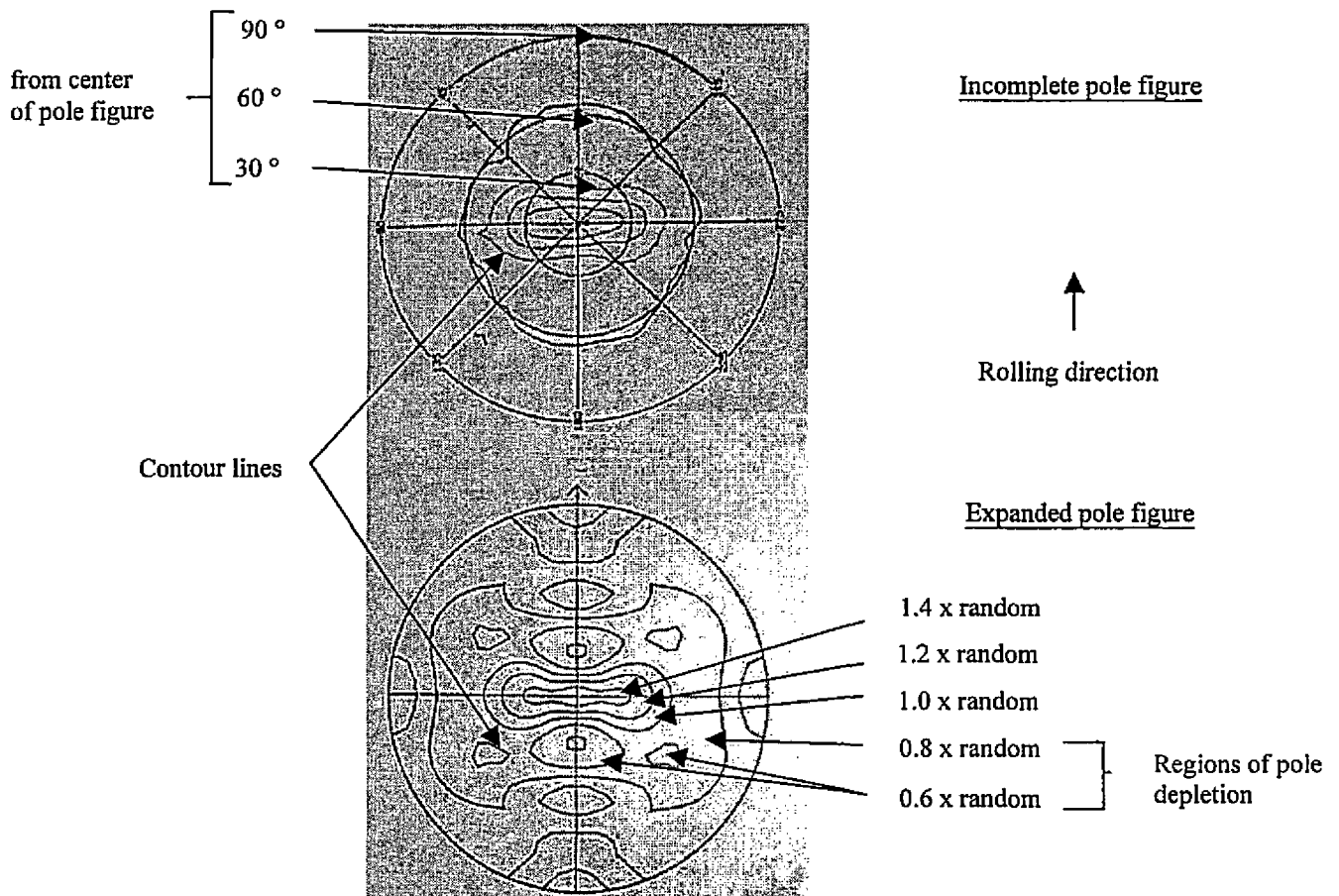
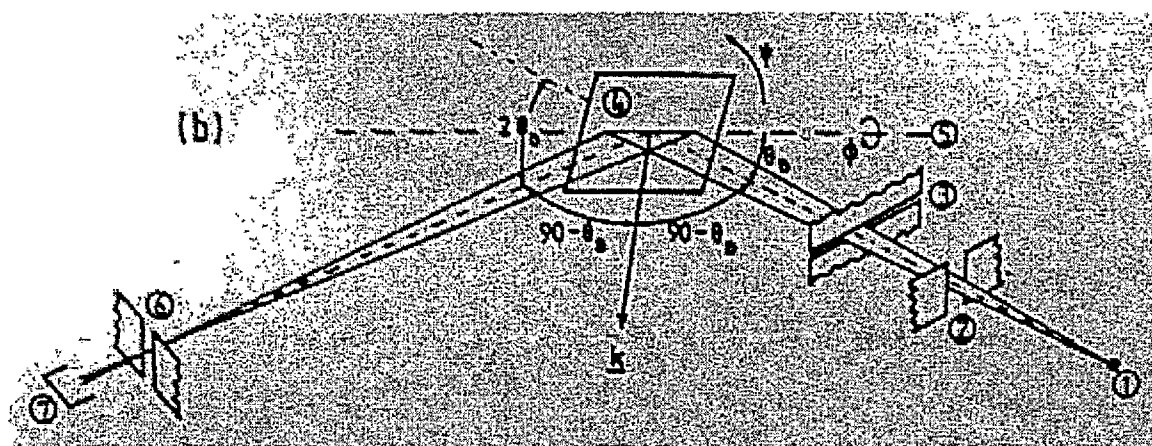


figure and the expanded pole figure. The pole figures obtained in this investigation were obtained using the Schulz Reflection method [30]. There is a limitation associated with this method that arises due to the geometrical setting of the sample in the goniometer. A defocusing occurs that is explained well by both Sowerby [7] and Hatherley [4]. Figure 3.3.1.2, which is borrowed from Hatherly, illustrates the physical arrangement of a typical x-ray diffractometer. A x-ray beam from the source (1) is restricted by

Fig. 3.3.1.2



divergence slits (2) and subsequently passes through a narrow horizontal slit (3) to the specimen (4). The major circle of the goniometer (5) is set so that its axis makes the Bragg angle, θ_B , with the central ray of the incident beam. The required diffraction condition is chosen by moving the arm holding the receiving slits (6) and counter (7) to the angle $2\theta_B$. When the angle ϕ is zero, i.e. the rolling direction points vertically and the normal direction to the plane of the sample surface now bisects the angle between the incident and diffracted beams, there is a semi-focussing effect which brings the diffracted beam to a point at the receiving slit. However, with increasing angle ϕ the irradiated area on the specimen becomes larger and as a result the point focus becomes spread out and not all of the beam passes through the receiving slit. This defocusing effect therefore causes a reduction in the measured intensity. The consequence is that information is obtained by the Schulz method only up to about $60 - 70^\circ$ (refer Fig. 3.3.1.1) and provides

only an incomplete pole figure. To obtain a complete pole figure, either a combined transmission-reflection method [31] is necessary or some form of composite specimen is used [32].

Another feature of note from Fig. 3.3.1.1. are the contour lines themselves. They are indicated as "n times random". When determining a pole figure from an unknown textured material, it is normal practice to also carry out a run on a specimen which is un-textured or "random". As Hatherly explains [4], this "random" specimen serves two important purposes. Since it has no texture any variation in the measured diffraction intensity may be attributed solely to the defocusing effect and so it provides a means or correction for defocusing. Secondly, it provides a logical reference intensity level with which to compare the textured material. Regions in the pole figure which show less than the random specimen intensity (i.e. < 1 times random) may be considered depleted in poles. The augmented intensity regions are readily quantified by contours of 1.5 times random, 2 times random, etc.

The upper pole figure in Fig. 3.3.1.1. is an example of an incomplete pole figure derived by the Schulz method as described above. If however, the information from more than one pole figure is available then an expanded pole figure can be generated as shown in the lower half of Fig. 3.3.1.1. The orientations associated with each pole figure are all related geometrically. Hence, a computer software algorithm can quickly combine such information to generate the expanded pole figure.

3.3.2 – CODF's

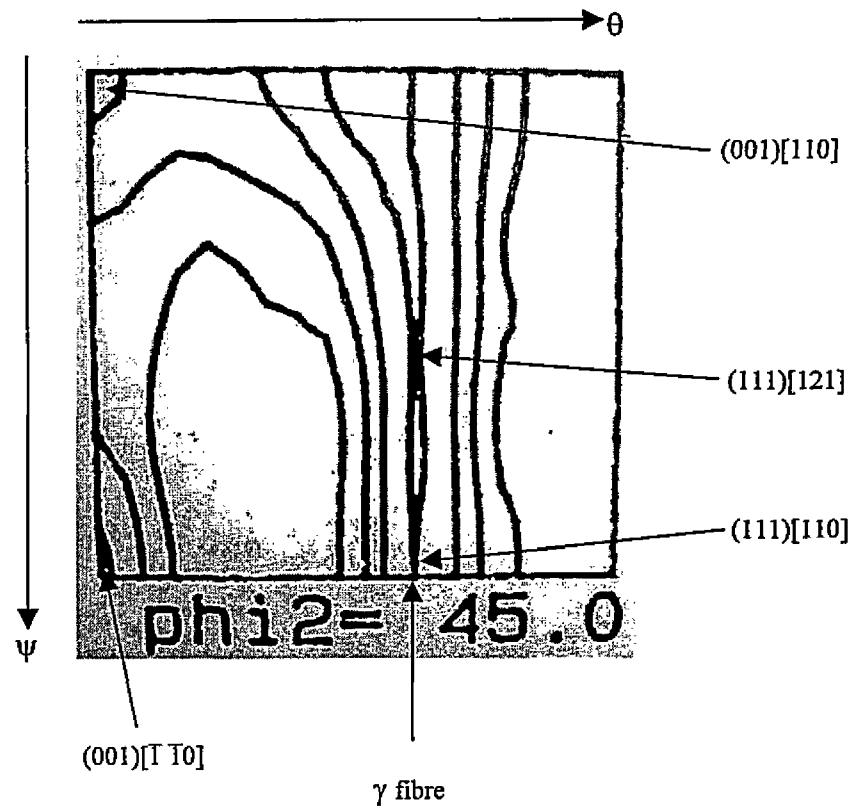
The CODF's were generated from the pole figures again using Los Alamos Laboratories software. The Los Alamos software that was available at Dofasco was an older version that "simply" generated CODF's from measured pole figures. More current versions of the same software can also predict deformation textures and their corresponding CODF's, as well as yield loci, and variations in r value.

The convention used in this thesis to describe orientation will be the Roe [17] definition of the Euler angles (i.e. ψ , θ , ϕ). The Los Alamos software actually generated two sets of CODF's. The one set are two dimensional slices at $5^\circ \psi$ intervals. The second set are slices at $5^\circ \phi$ intervals. The second set was used predominantly because it allowed easier identification of the various orientation fibres.

The frame of reference for the CODF's are the Euler angles relative to the rolling direction and to the rolling plane. To translate these angles to the Miller indices of the crystallographic orientation please refer to Appendix A where R. Sowerby has worked out the relationship between Euler angles and Miller

indices. The equations and charts provided by Davies, Goodwill, and Kallend [2] were also helpful for quick conversion (refer Appendix A). Figure 3.3.2.1 illustrates a typical CODF. It is a slice at $\phi = 45^\circ$. The Miller indices of various orientations are indicated in the figure.

Fig. 3.3.2.1



There is almost an unlimited amount of information available from the CODF chart. This investigation was focused on formability so attention was given to the $\{100\}$ plane and the $\{111\}$ plane. The literature agrees that the former has a negative effect while the latter has a positive effect on formability. Consequently, two fibres were of interest, the η fibre ($\{001\} \parallel ND$) (i.e. the normal to the $\{001\}$ plane is parallel to the normal to the rolled sheet), and the γ fibre ($\{111\} \parallel ND$) (i.e. the normal to the $\{111\}$ plane is parallel to the normal to the rolled sheet) [6]. On the η fibre, the only significant

intensity level occurred at (100)[011]. Consequently, only this orientation was monitored. For the γ fibre, four peaks occurred on a regular basis. They were (111)[112], (111)[121], (111)[011], and (111)[110].

3.3.3 – Metallography

The pole figures and CODF's that will be used in this thesis provide us with information at the microscopic or crystalline level. It is also useful to keep in mind what is happening at the macroscopic level, i.e. the change in the morphology of the grains. For this purpose the following six micrographs are included. They show the changes in the grain structure for Sample 1 with increasing cold roll reduction. They are taken from the sample surface. Micrographs were also taken at the sample centerline and compared against the micrographs from the sample surface. No significant difference was found, at any of the cold roll stages, between the morphology of the grains at the surface versus the morphology of the grains at the centerline.

Fig. 3.3.3.1. Optical micrograph showing a hot rolled structure which is composed of ferrite grains with very fine carbides at grain boundaries.

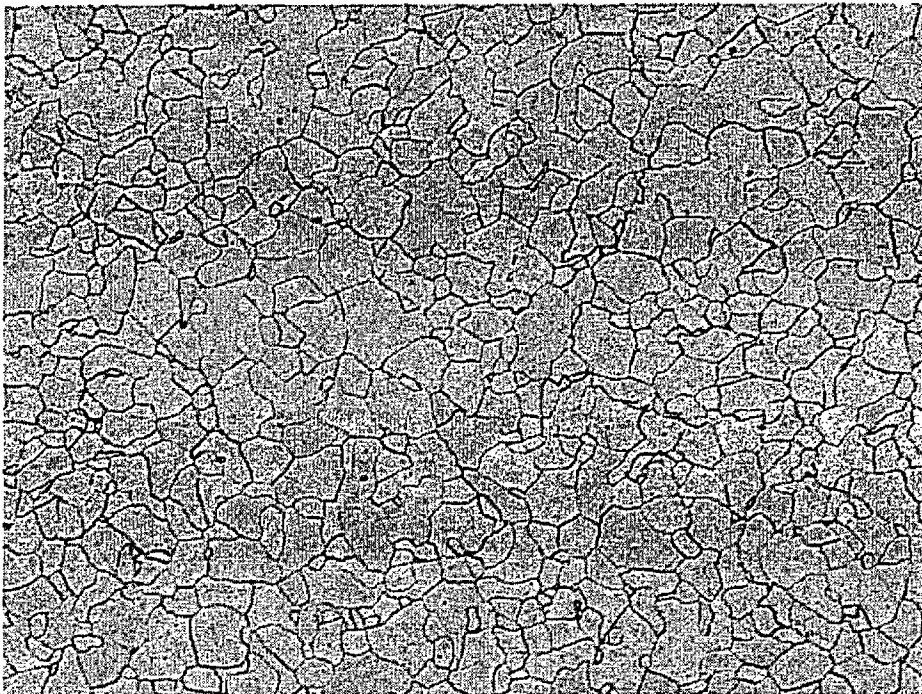


Fig. 3.3.3.2 Optical micrograph showing the structure of the hot rolled product after Cold Reduction of 31.3% through Stand #1.

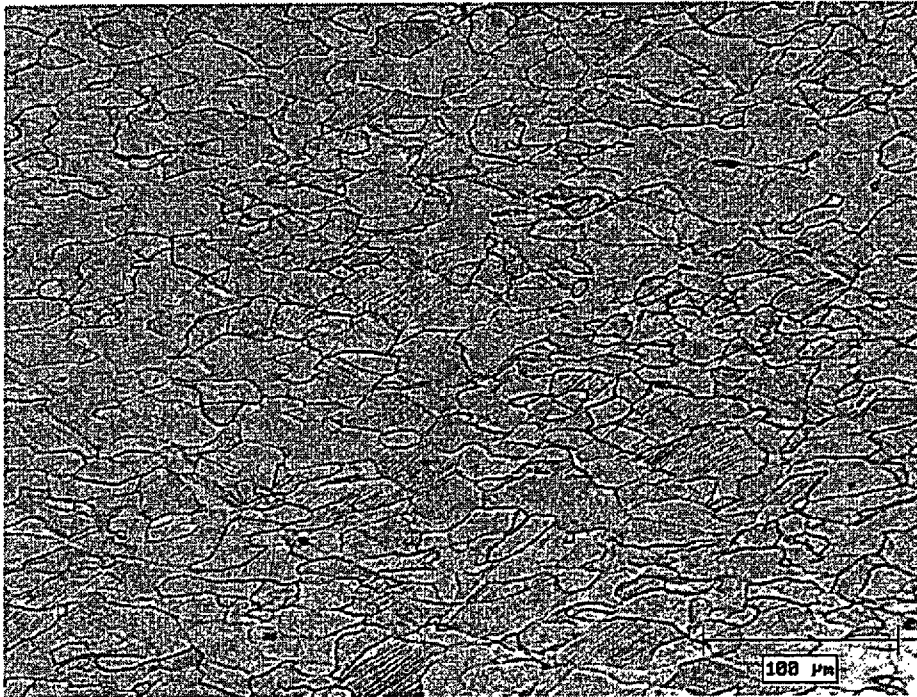


Fig. 3.3.3.3 Optical micrograph showing the structure of the hot rolled product after Second Cold Reduction of 31.0% through Stand #2.

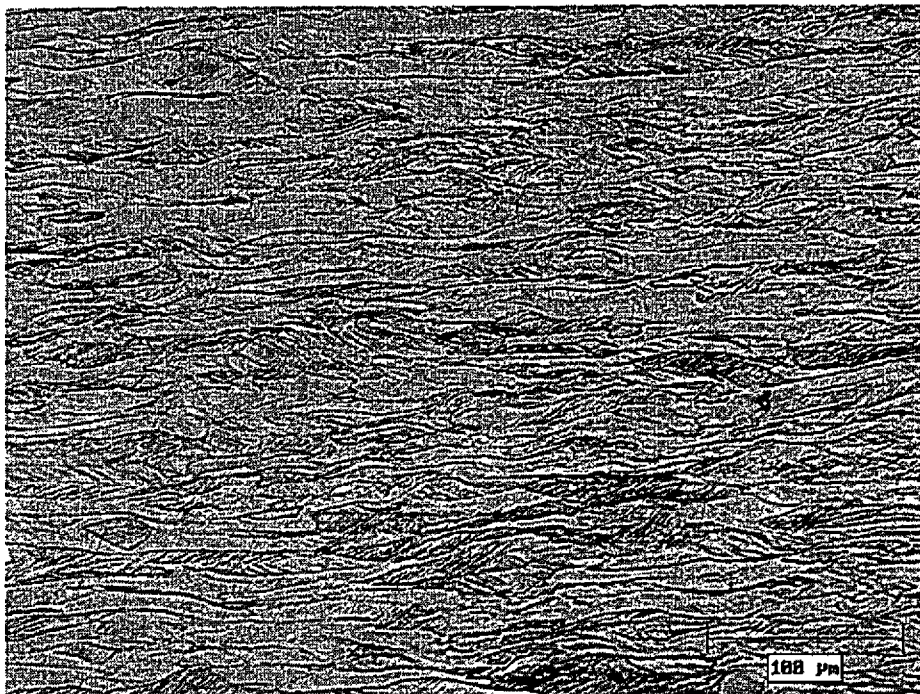


Fig. 3.3.3.4 Optical micrograph showing the structure of the hot rolled product after Third Cold Reduction of 31.3% through Stand #3.

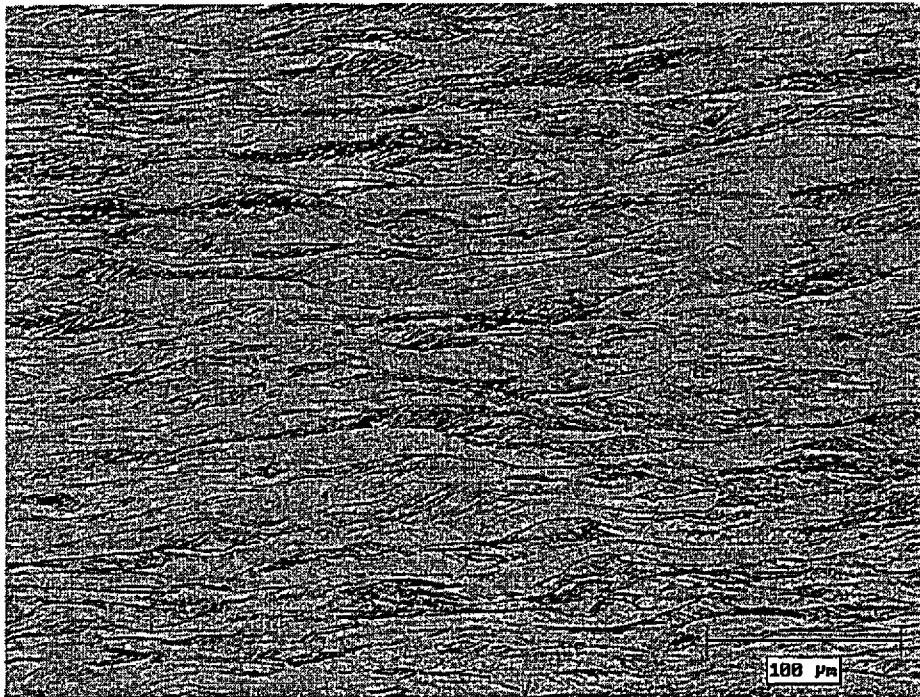


Fig. 3.3.3.5 Optical micrograph showing the structure of the hot rolled product after Fourth Cold Reduction of 32.4% through Stand #4.

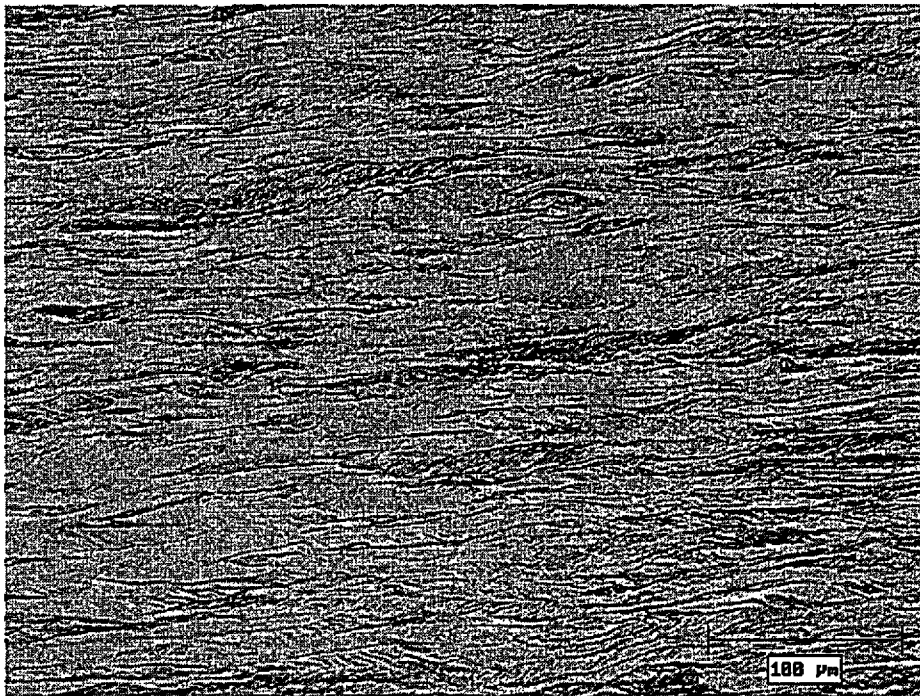
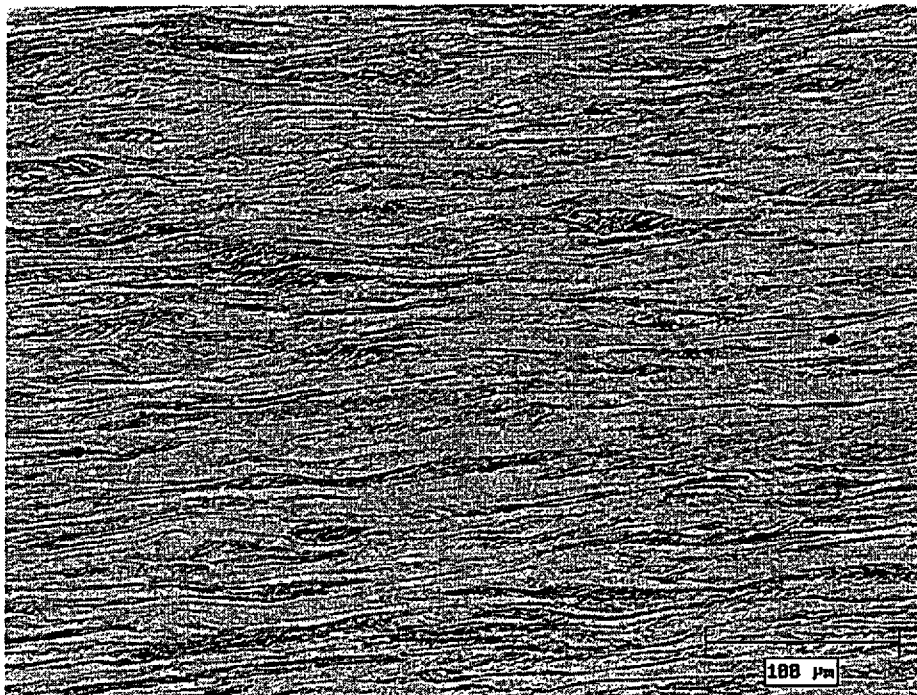


Fig. 3.3.3.6 Optical micrograph showing the structure of the hot rolled product after Fifth Cold Reduction of 1.7% through Stand #5.



Chapter 4 – Data/Experimental Results

This chapter summarizes the pole figures and CODF's in tabular and chart form. As mentioned in chapter 1, the intent of this work is to investigate the development of texture at the intermediate stages of cold roll reduction. Accordingly, the data will be presented in a manner to allow the reader, at a glance, to detect and compare any changes in the development of some of the more significant texture orientations, as the material was progressively cold worked. By not showing the actual pole figures and CODF's a wealth of information is forfeited. For those readers who are interested in comparing the pole figures and CODF's for themselves, two of the six sets can be found in Appendix B

Certain principal textures were the focus of this investigation, the "Cube-on-Face" (i.e. $\{100\}$) and the "Cube-on-Corner" (i.e. $\{111\}$). These two textures have the most influence on formability. Consequently, the following data compares the development primarily of these two textures. For completion, the other main texture, the Cube-on-Edge (i.e. $\{110\}$), is also followed but in the steels investigated, this texture has a minor presence. Figure 4.1, taken from Backofen [18], illustrates these three orientations where r, t, and z are the rolling, transverse, and through-thickness directions respectively.

Fig. 4.1

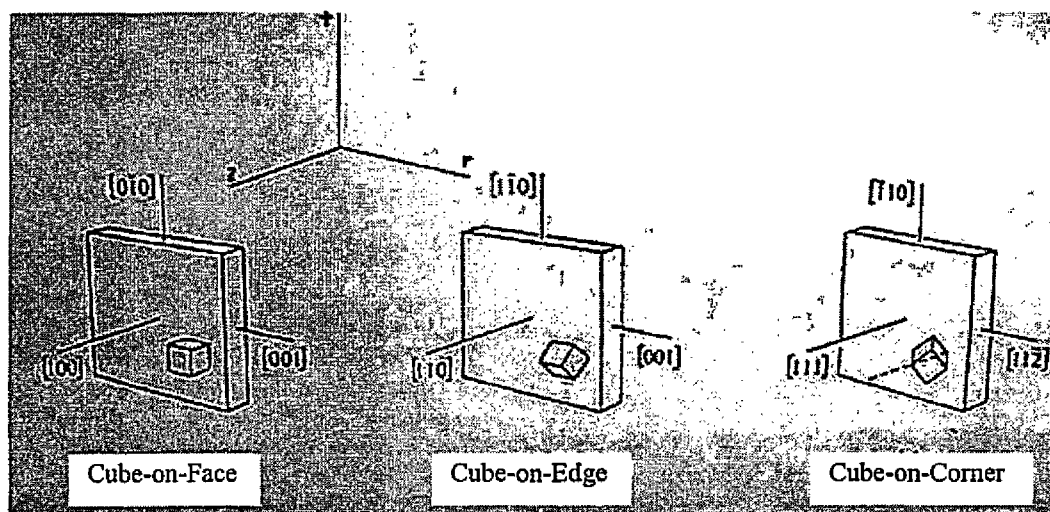


Table 4.1 below identifies the six sets of samples that were investigated, listing the steel type, entry and delivery gauges, as well as the reduction done on each stand.

Table 4.1

Sample #, Steel type, Initial gauge, Final gauge	% Reduction at each stand				
	1	2	3	4	5
# 1 IF 3.81 mm 0.826 mm	31.3	31.0	31.3	32.4	1.7
# 2 AK 2.29 mm 0.279 mm	32.5	34.1	34.3	38.0	32.1
# 3 IF 5.08 mm 0.927 mm	33.9	33.6	33.9	36.1	1.6
# 4 AK 2.29 mm 0.231 mm	34.5	37.3	37.7	40.4	33.8
# 5 AK 2.29 mm 0.292 mm	35.1	37.8	32.8	33.9	28.8
# 6 IF 3.81 mm 0.826 mm	31.4	31.5	31.4	31.7	1.6

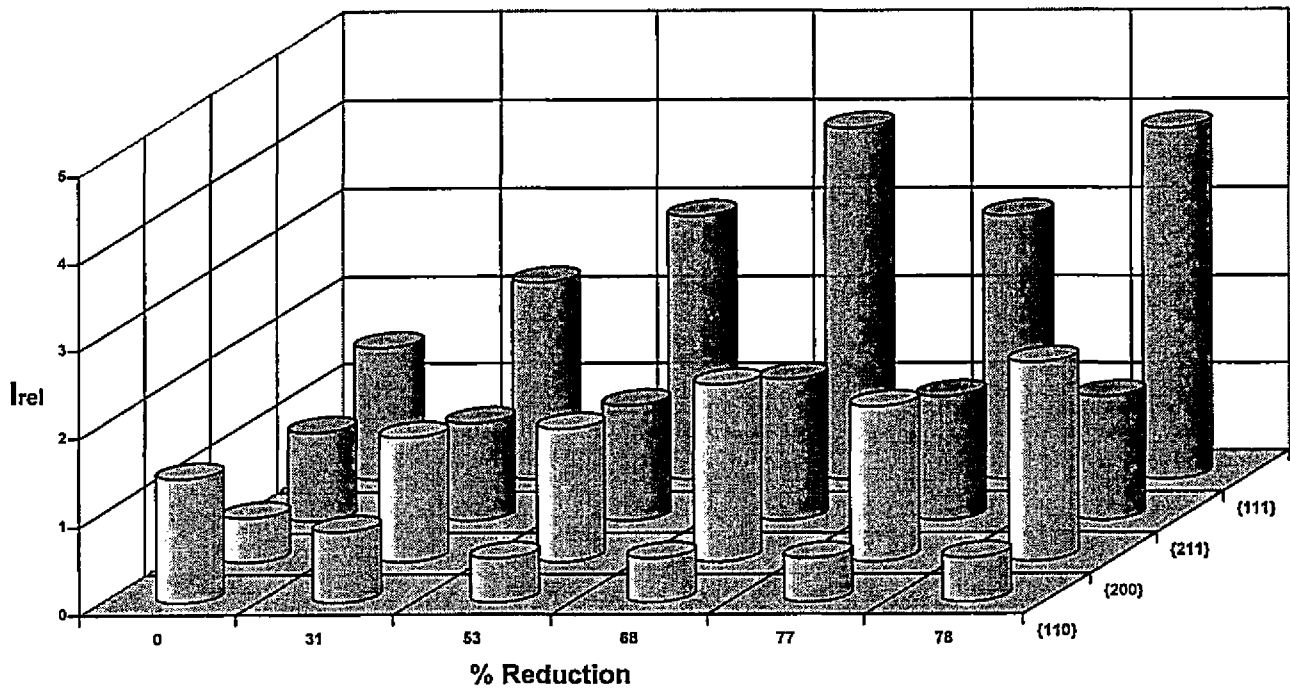
4.1 - Sample 1 - CC007B, 3.81, 0.8255, matte finish on fifth stand

4.1.1 - Pole Figure Analysis

Table 4.1.1 - Intensity of orientation at % reduction

	0	31	53	68	77	78
{110}	1.4	0.8	0.5	0.5	0.5	0.5
{200}	0.5	1.4	1.5	2.0	1.75	2.25
{211}	1.0	1.1	1.3	1.6	1.4	1.4
{111}	1.5	2.25	3.0	4.0	3.0	4.0

Fig. 4.1.1 - Intensity of orientation at % reduction



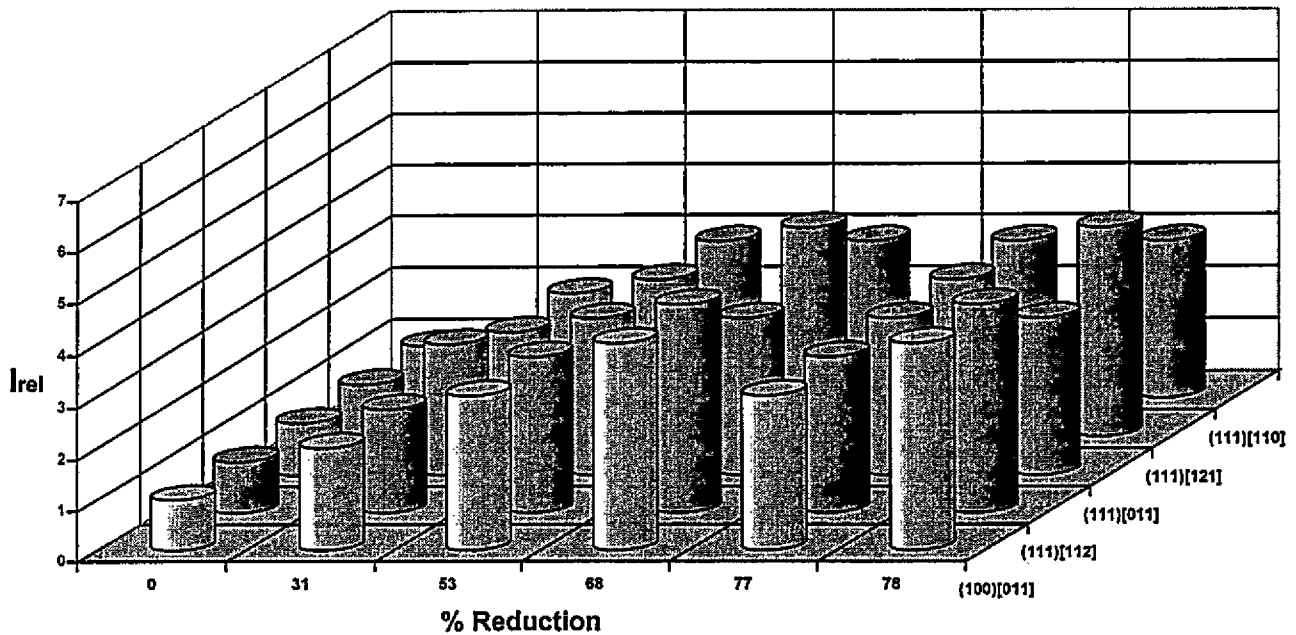
4.1 (continued) – sample 1, CC007B, 3.81, 0.8255, matte finish on fifth stand

4.1.2 - CODF Analysis

Table 4.1.2 - Intensity of orientation at % reduction

	0	31	53	68	77	78
(100)[011]	1.0	2.0	3.0	4.0	3.0	4.0
(111)[112]	1.0	2.0	3.0	4.0	3.0	4.0
(111)[011]	1.0	2.5	3.0	3.0	3.0	3.0
(111)[121]	1.0	2.0	3.0	4.0	3.0	4.0
(111)[110]	1.0	2.0	3.0	3.0	3.0	3.0

Fig. 4.1.2 - Intensity of orientation at % reduction



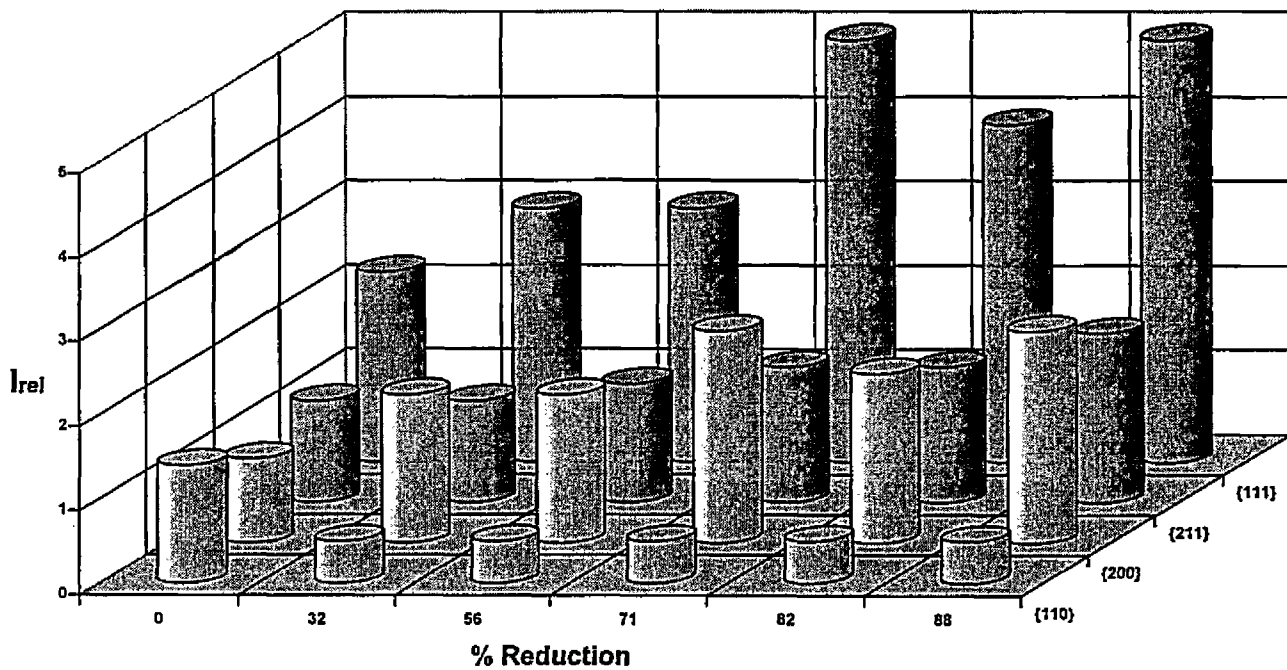
4.2 - Sample 2 - CC060, 2.286, 0.2794, bright finish on fifth stand

4.2.1 - Pole Figure Analysis

Table 4.2.1 - Intensity of orientation at % reduction

	0	32	56	71	82	88
{110}	1.4	0.5	0.5	0.5	0.5	0.5
{200}	1.0	1.75	1.75	2.5	2.0	2.5
{211}	1.2	1.2	1.4	1.6	1.6	2.0
{111}	2.25	3.0	3.0	5.0	4.0	5.0

Fig. 4.2.1 - Intensity of orientation at % reduction



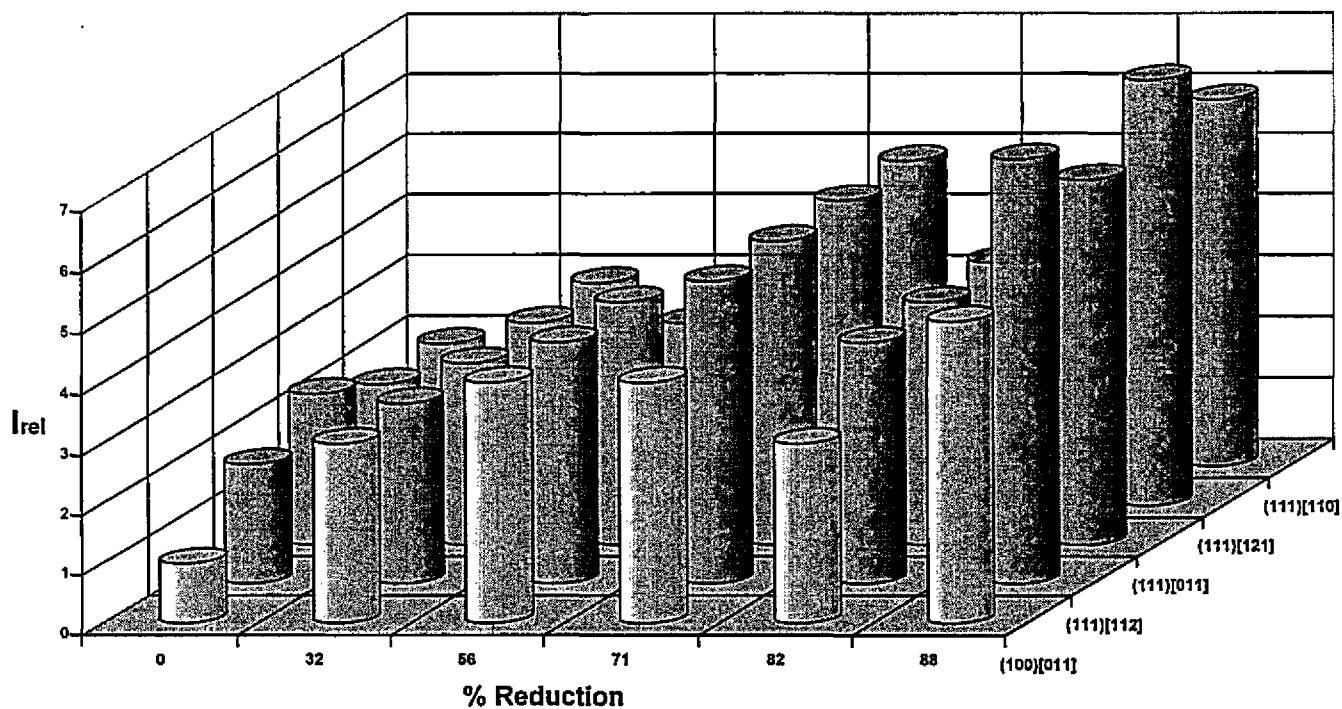
4.2 (continued) – sample 2, CC060, 2.286, 0.2794, bright finish on fifth stand

4.2.2 - CODF Analysis

Table 4.2.2 - Intensity of orientation at % reduction

	0	32	56	71	82	88
(100)[011]	1.0	3.0	3.0	4.0	3.0	5.0
(111)[112]	2.0	3.0	3.0	5.0	4.0	7.0
(111)[011]	2.0	3.0	4.0	5.0	4.0	6.0
(111)[121]	2.0	3.0	3.0	5.0	4.0	7.0
(111)[110]	2.0	3.0	3.0	5.0	4.0	6.0

Fig. 4.2.2 - Intensity of orientation at % reduction



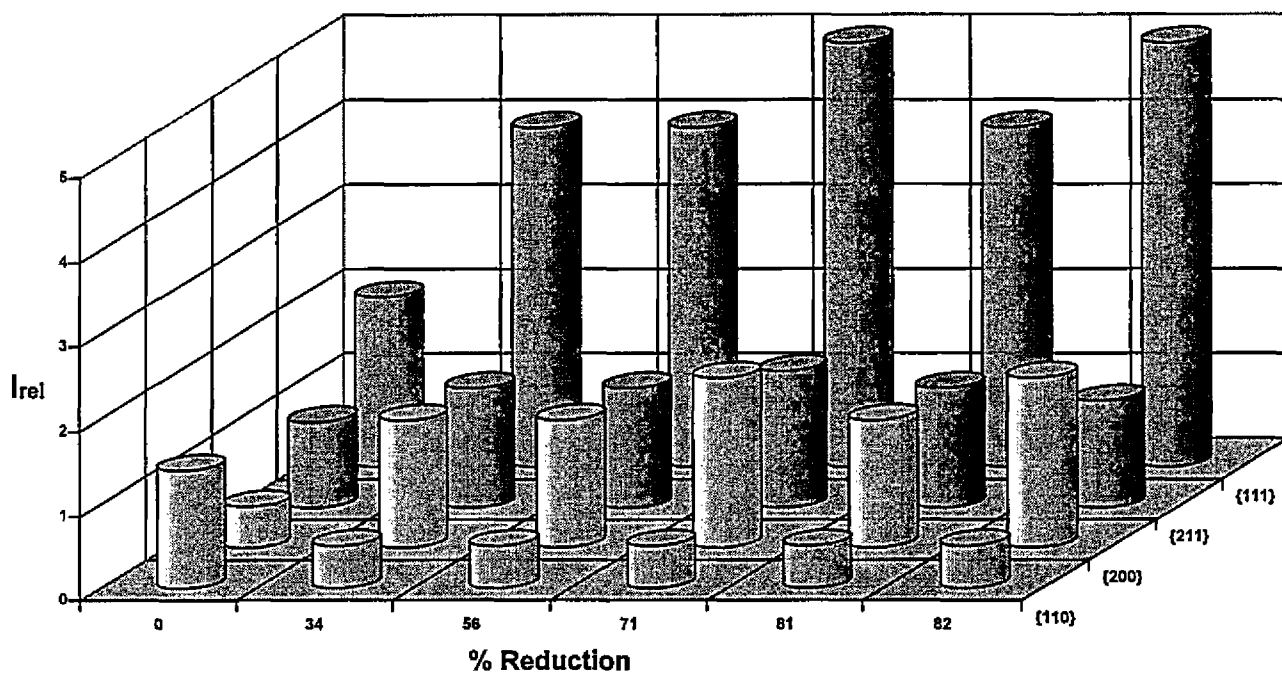
4.3 - Sample 3 - CC006B, 5.08, 0.9271, matte finish on fifth stand

4.3.1 - Pole Figure Analysis

Table 4.3.1 - Intensity of orientation at % reduction

	0	34	56	71	81	82
(110)	1.4	0.5	0.5	0.5	0.5	0.5
(200)	0.5	1.5	1.5	2.0	1.5	2.0
(211)	1.0	1.4	1.4	1.6	1.4	1.25
(111)	2.0	4.0	4.0	5.0	4.0	5.0

Fig. 4.3.1 - Intensity of orientation at % reduction



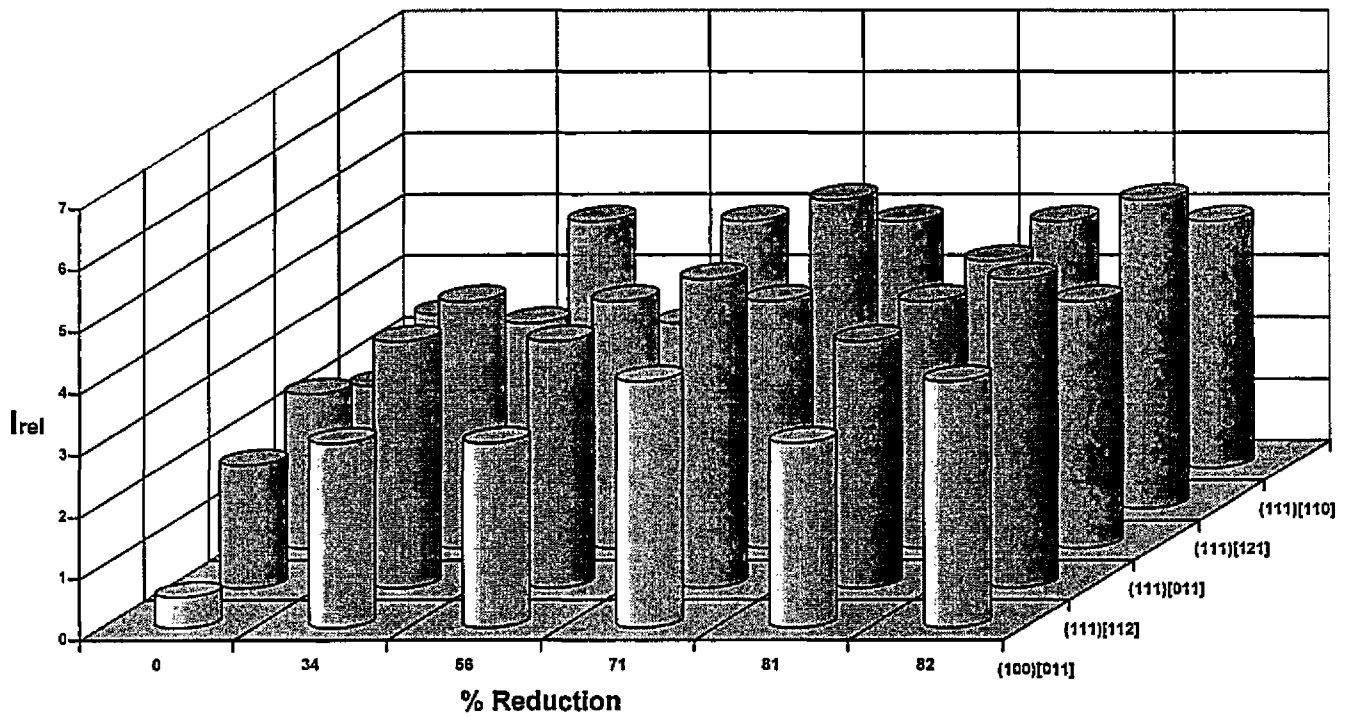
4.3 (continued)- sample 3, CC006B, 5.08, 0.9271, matte finish on fifth stand

4.3.2 - CODF Analysis

Table 4.3.2 - Intensity of orientation at % reduction

	0	34	56	71	81	82
(100)[011]	0.5	3.0	3.0	4.0	3.0	4.0
(111)[112]	2.0	4.0	4.0	5.0	4.0	5.0
(111)[011]	2.5	4.0	4.0	4.0	4.0	4.0
(111)[121]	2.0	3.0	3.0	5.0	4.0	5.0
(111)[110]	2.5	4.0	4.0	4.0	4.0	4.0

Fig. 4.3.2 - Intensity of orientation at % reduction



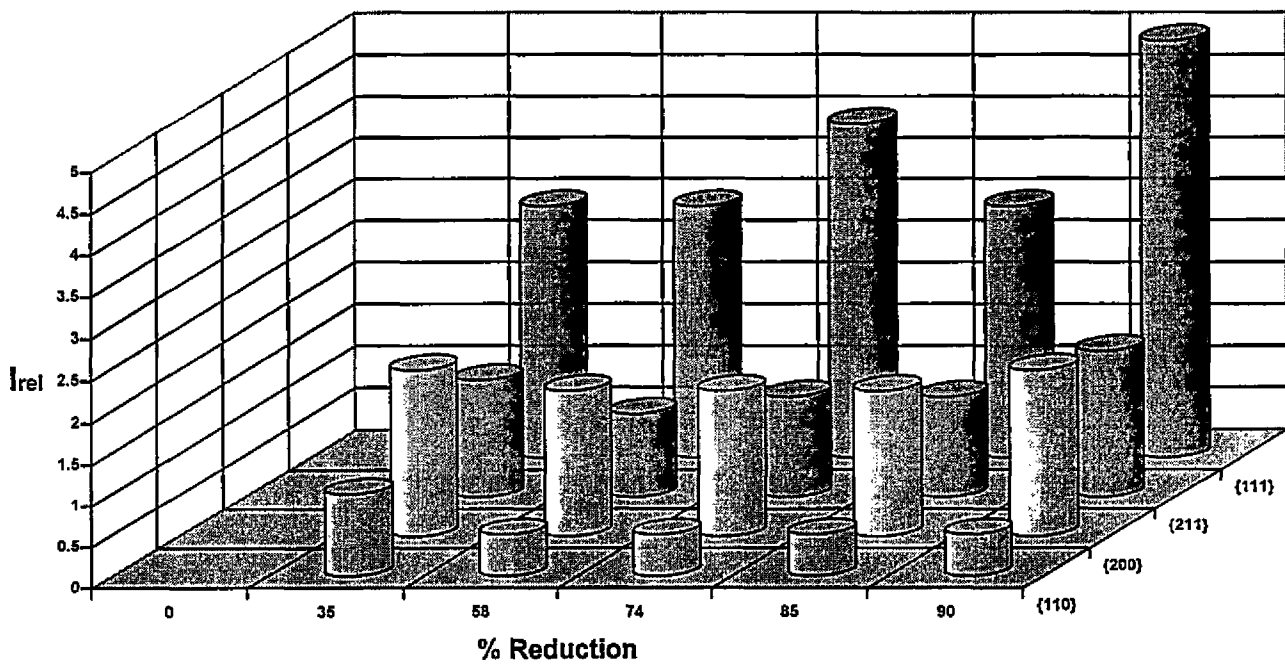
4.4 - Sample 4 - EA061, 2.286, 0.231, bright finish on fifth stand

4.4.1 - Pole Figure Analysis

Table 4.4.1 - Intensity of orientation at % reduction

		0	35	58	74	85	90
(110)	No sample	1.0	0.5	0.5	0.5	0.5	0.5
(200)	No sample	2.0	1.75	1.75	1.75	1.75	2.0
(211)	No sample	1.4	1.0	1.2	1.2	1.2	1.75
(111)	No sample	3.0	3.0	4.0	3.0	3.0	5.0

Fig. 4.4.1 - Intensity of orientation at % reduction



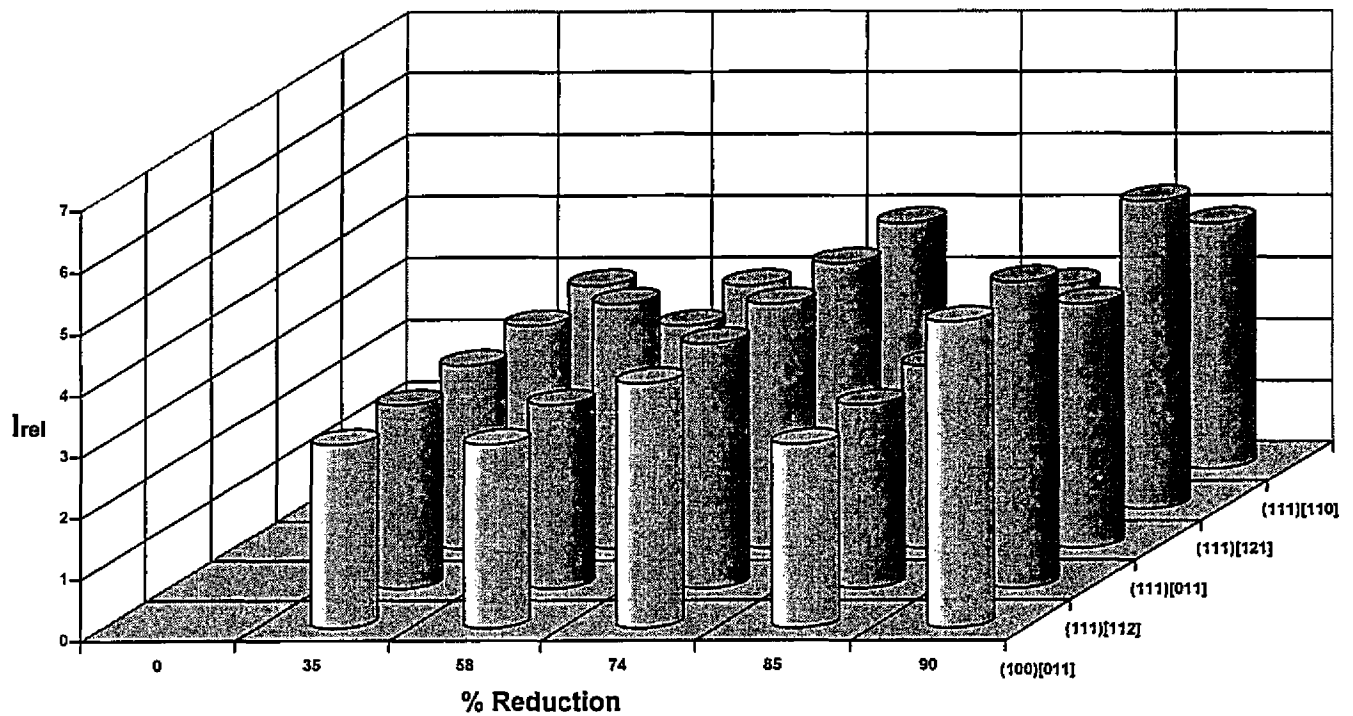
4.4 (continued)- sample 4, EA061, 2.286, 0.231, bright finish on fifth stand

4.4.2 - CODF Analysis

Table 4.4.2 - Intensity of orientation at % reduction

	0	35	58	74	85	90
(100)[011]	No sample	3.0	3.0	4.0	3.0	5.0
(111)[112]	No sample	3.0	3.0	4.0	3.0	5.0
(111)[011]	No sample	3.0	4.0	4.0	3.0	4.0
(111)[121]	No sample	3.0	3.0	4.0	3.0	5.0
(111)[110]	No sample	3.0	3.0	4.0	3.0	4.0

Fig. 4.4.2 - Intensity of orientation at % reduction



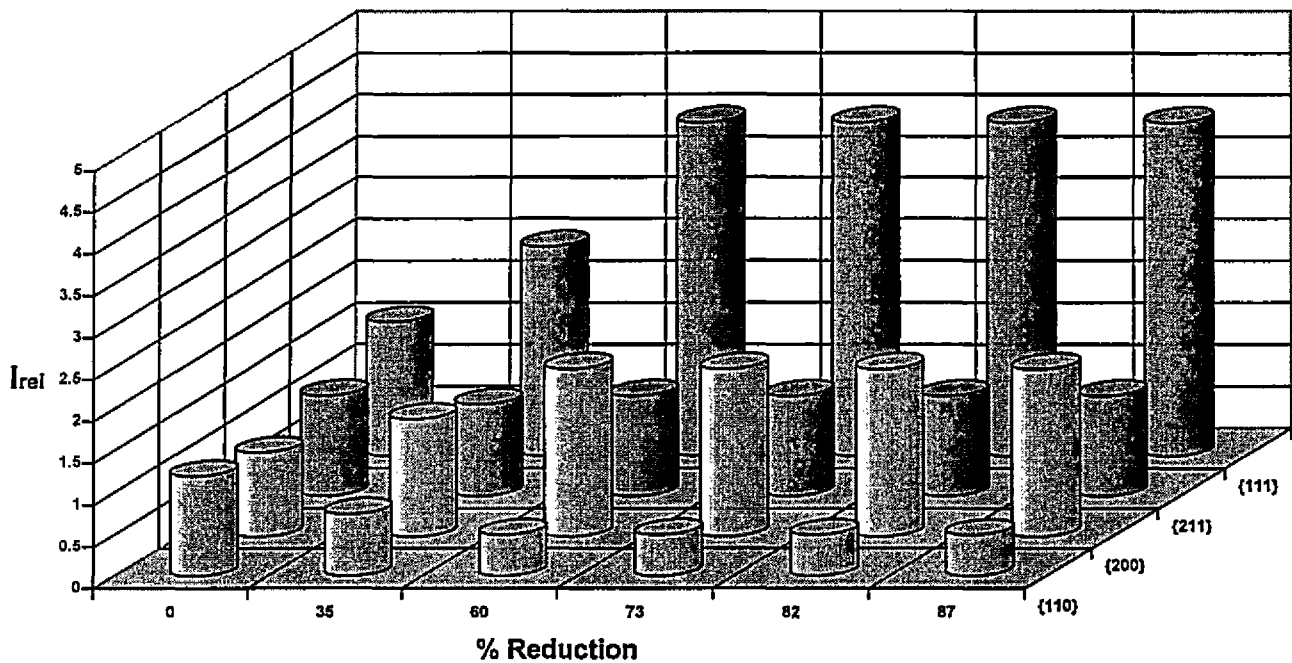
4.5 Sample 5 - CC060A, 2.286, 0.2921, bright finish on fifth stand

4.5.1 - Pole Figure Analysis

Table 4.5.1 - Intensity of orientation at % reduction

	0	35	60	73	82	87
(110)	1.2	0.75	0.5	0.5	0.5	0.5
(200)	1.0	1.4	2.0	2.0	2.0	2.0
(211)	1.2	1.1	1.2	1.2	1.2	1.2
(111)	1.6	2.5	4.0	4.0	4.0	4.0

Fig. 4.5.1 - Intensity of orientation at % reduction



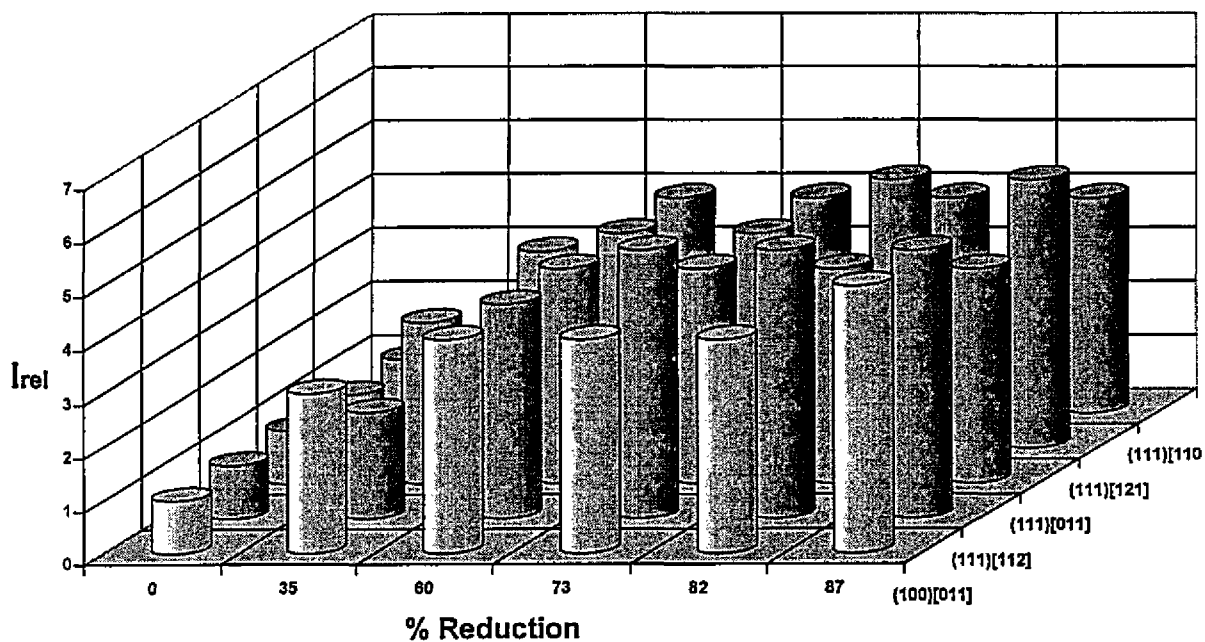
4.5 (continued)- sample 5, CC060A, 2.286, 0.2921, bright finish on fifth stand

4.5.2 - CODF Analysis

Table 4.5.2 - Intensity of orientation at % reduction

	0	35	60	73	82	87
(100)[011]	1.0	3.0	4.0	4.0	4.0	5.0
(111)[112]	1.0	2.0	4.0	5.0	5.0	5.0
(111)[011]	1.0	3.0	4.0	4.0	4.0	4.0
(111)[121]	1.0	2.0	4.0	4.0	5.0	5.0
(111)[110]	1.0	3.0	4.0	4.0	4.0	4.0

Fig. 4.5.2 - Intensity of orientation at % reduction



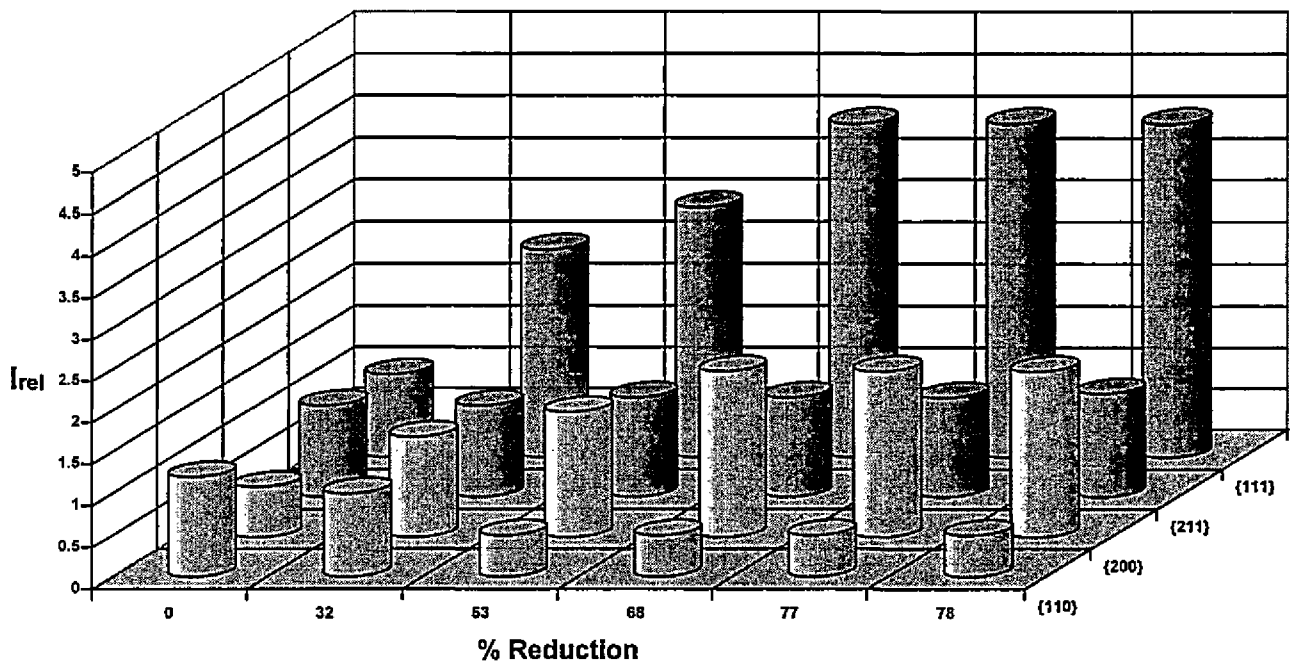
4.6 - Sample 6 - CC007B, 3.81, 0.8255, matte finish on fifth stand

4.6.1 - Pole Figure Analysis

Table 4.6.1 - Intensity of orientation at % reduction

	0	32	53	68	77	78
(110)	1.2	1.0	0.5	0.5	0.5	0.5
(200)	0.6	1.2	1.5	2.0	2.0	2.0
(211)	1.1	1.1	1.2	1.2	1.2	1.25
(111)	1.0	2.5	3.0	4.0	4.0	4.0

Fig. 4.6.1 - Intensity of orientation at % reduction



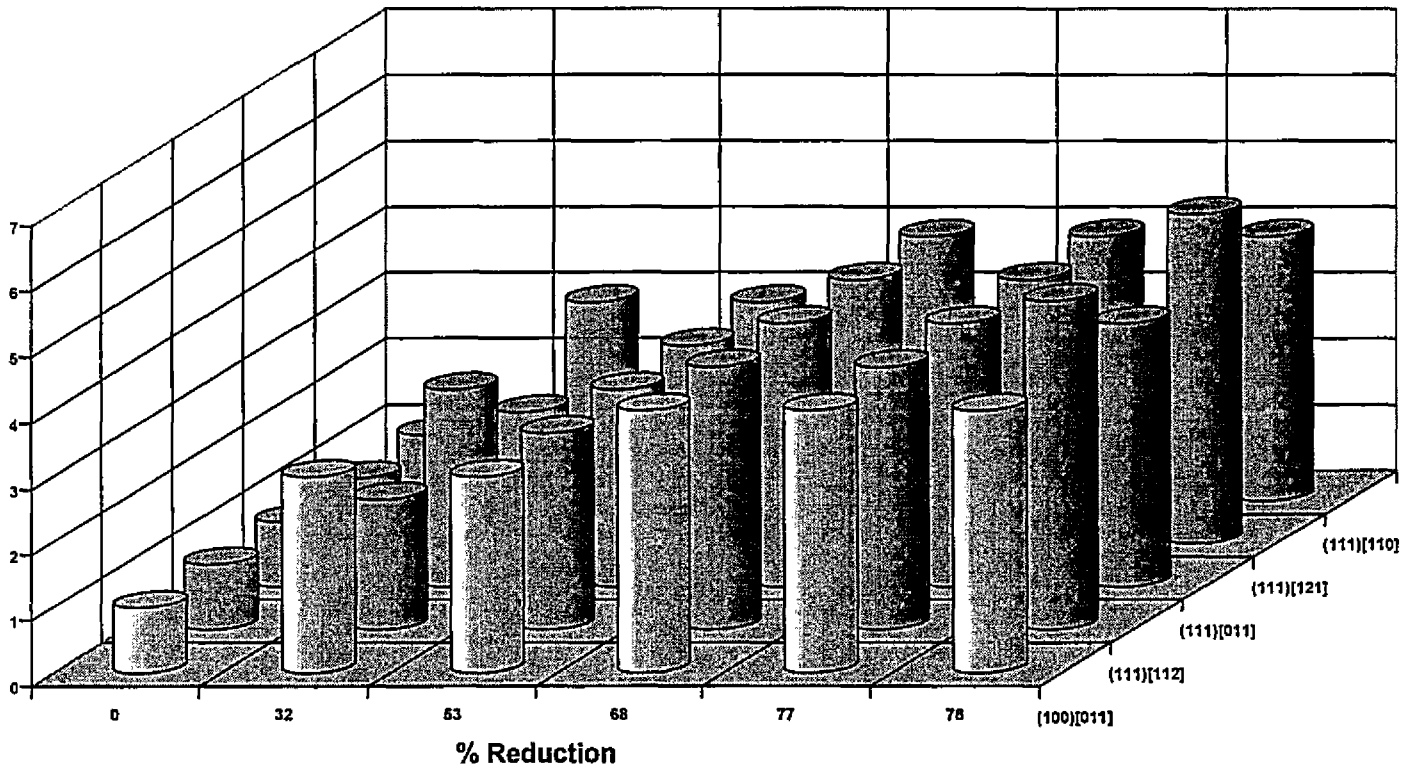
4.6 (continued)- sample 6, CC007B, 3.81, 0.8255, matte finish on fifth stand

4.6.2 - CODF Analysis

Table 4.6.2 - Intensity of orientation at % reduction

	0	32	53	68	77	78
(100)[011]	1.0	3.0	3.0	4.0	4.0	4.0
(111)[112]	1.0	2.0	3.0	4.0	4.0	5.0
(111)[011]	1.0	3.0	3.0	4.0	4.0	4.0
(111)[121]	1.0	2.0	3.0	4.0	4.0	5.0
(111)[110]	1.0	3.0	3.0	4.0	4.0	4.0

Fig. 4.6.2 - Intensity of orientation at % reduction



Chapter 5 – Discussion of Results

5.1 - Final Cold Roll Texture and Texture Stability

The results of this investigation find support from the literature [1,4,6], that for low carbon and ultra-low carbon steels, the significant cold rolled texture after approximately 70-90 % reduction, is a combination of the {111}, {100} and {211} orientations. The {110} orientation is virtually non-existent. Of the first three, the {111} orientation predominates. The following table shows the relative intensities of the final cold rolled texture, where the pole figure intensity has been averaged for the three samples of each type of material.

Table 5.1

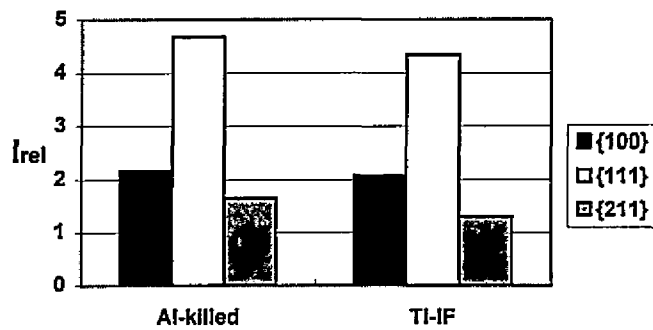
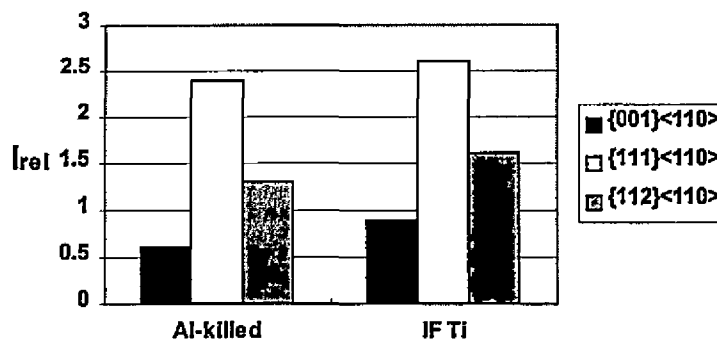


Table 5.1 can be compared to Table 5.2 reproduced by Mishra and Darmann [1] from a paper by Lotter *et al.* [33] that shows a comparison of relative intensities of fully processed material.

Table 5.2



The work of Lotter *et al.* agrees with this investigation with regard to the dominant intensity of the {111} texture, however, there is some difference with regard to the relative intensities of the {100} and {211} textures. The explanation could lie in the fact that Lotter's data were from fully processed material, i.e. after re-crystallization. As well, Lotter *et al.* used CODF's to measure the intensity of specific orientations, i.e., {001}<110>, {111}<110>, and {112}<110>. These specific orientations may have a different relative intensity than the corresponding family of planes, i.e., {001}, {111}, and {112}.

As mentioned above, the predominant texture in cold rolled material is the {111} crystallographic plane in the plane of the rolled sheet, for both the AK and IF steels. The next dominant texture is the {100} plane while the {110} plane has the lowest intensity of the three. This order of intensity exists, with small variations in levels but never in order, from the initial cold reduction pass of 30 %, through to the final pass resulting in a total cold roll reduction of 90 %. This order of intensity derived experimentally confirms what Backofen [8] explained theoretically (refer section 2.7 of this thesis) in terms of stability and minimum energy states.

5.2 - Effect of Cold Reduction on the Normal Strain Ratio

The following two tables, 5.3 and 5.4, list the average intensity of the {111}, and {200} texture for the AK and the IF steels of this investigation.

Table 5.3 – AK steel, average intensity

% reduction	32-35	56-60	71-74	82-85	87-90
{111}	2.83	3.33	4.33	3.67	4.67
{200}	1.72	1.83	2.08	1.92	2.17
Difference	1.11	1.50	2.25	1.75	2.50

Table 5.4 – IF steel, average intensity

% reduction	31-34	53-56	68-71	matte surface applied	
				78-82	78-82
{111}	2.92	3.33	4.33	3.67	4.33
{200}	1.37	1.5	2.0	1.75	2.08
Difference	1.55	1.83	2.33	1.92	2.25

Also listed in the two tables is the difference in intensity between the two orientations. There is a pattern to this difference with increased cold reduction. There is a dip at approximately 82 % reduction followed by at least a partial recovery with further reduction. These results indicate a preferential increase

of the {111} component over the {200} component up to approximately 82 % cold roll reduction, a small reversal, then a recovery of the {111} component. With the IF samples, where the final mill stand merely imprints a matte finish onto the surface of the strip with only negligible additional reduction, this recovery of the {111} component may be confined only to the surface of the flat strip (this is possibly an area of future investigation).

Various investigators [1,24,25] have shown that there is a maximum value of \bar{r} that occurs at approximately 70-80 % reduction as measured in fully processed steel. The literature notes that \bar{r} increases with increasing cold roll reduction, but only to a point. Further reduction beyond this point causes a slight decrease in \bar{r} . The literature also agrees (and can be shown theoretically by considering distances, and thus the forces, between the atoms in the planes, cf. Whitely and Wise [24]) that \bar{r} correlates directly with the presence of the {111} plane and indirectly with the {100} plane as measured in the fully processed steel. Consequently, this decrease in \bar{r} at 70-80 % reduction, they attribute to an increase in the intensity of the {100} texture rather than a decrease in the {111} texture intensity. Mishra and Darmann [1] add further that the above is true only for AK steel. In IF steels, the {001} component is present to a lesser extent and high \bar{r} values are obtained for reductions even up to 90 %.

It would be nice to directly compare the results of this investigation on cold rolled steel with the investigations in the literature that have looked at fully processed steel. Both this investigation and the literature show a dip at approximately 80 % reduction. This investigation sees a dip in the ratio of the {111} plane and the {100} plane. The literature sees a dip in the \bar{r} . However, we must be careful. Though it is generally agreed that there is a direct correlation between the measured \bar{r} value of fully processed steel and the measured intensities of the {111} and {100} planes lying in the plane of the rolled sheet after it has been cold rolled, it must be understood that this correlation is strictly an empirically derived relationship. A high \bar{r} value in the fully processed steel coincides with improved formability. Likewise the presence of {111} planes lying in the plane of the sheet and the absence of {100} planes lying in the plane of the sheet of the cold rolled steel can be shown to coincide with improved formability of the steel after it has been fully processed, i.e. annealed. Thus, only by association can it be concluded that a favorable \bar{r} value coincides with the presence of {111} planes and the absence of {100} planes lying in the plane of the cold rolled sheet.

Although Mishra and Darmann's [1] results were on fully processed steel, a comparison of tables 5.3 and 5.4 show agreement with them. There is less of a presence of the {100} component in the IF steel as compared to the AK steel. This explains why fully processed IF steels consistently show higher \bar{r} values than AK steels. There is a larger presence of the {111} orientation relative to the {100} orientation.

5.3 - CODF's

Mishra and Darman [1] have found that Ti-stabilized, IF material is characterized by a sharp {111}<112> orientation, again measured in fully processed material. In our investigation, on cold rolled material, there was minimal difference between Al-killed and Ti-stabilized IF material with regards to the presence of the {111}<112> orientation. This is illustrated by Fig.'s 5.1 and 5.2.

Fig. 5.1 - IF

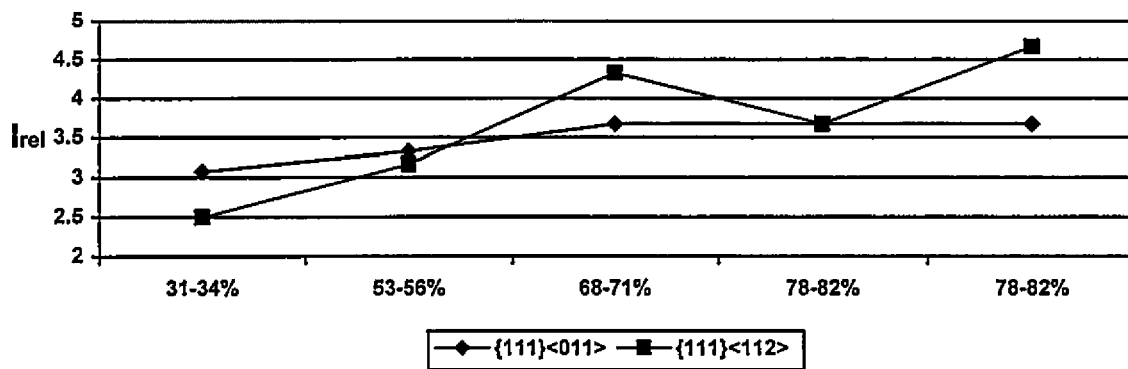
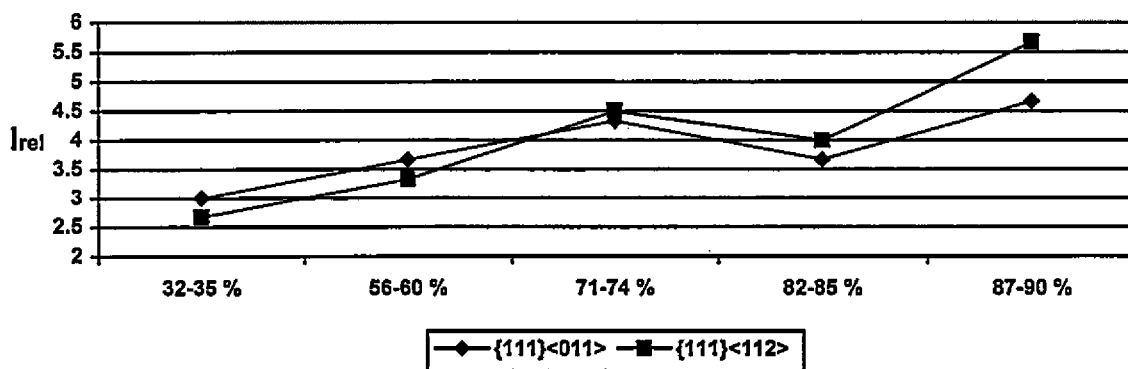


Fig. 5.2 - AK



This investigation indicates that at low reductions for both types of material, the $\{111\}\langle 110\rangle$ orientation predominates, while at higher cold roll reductions, the $\{111\}\langle 112\rangle$ orientation predominates. At approximately 60-65 % reduction, the relative strengths of the two orientations switches. This observation is partially corroborated by Li, Diak, and Saimoto [15] who have found a similar preferential growth of the $\{111\}\langle 112\rangle$ orientation in their simulation of a tandem cold roll mill. However, their results indicate that the preference for the $\{111\}\langle 112\rangle$ orientation starts immediately at the early reductions. It could be suggested that in our investigation the hot band substrate already contained a non-random presence of the $\{111\}\langle 011\rangle$ orientation. However, the CODF's of the hot band substrate for all six samples do not indicate any consistent non-random orientation that favors the $\{111\}\langle 011\rangle$ orientation.

5.4 - Surface texture

It was mentioned above (section 5.2) that the measured texture at the surface of the strip may not be consistent through the thickness of the strip. This investigation did not measure texture at the strip center, only at the surface. The results for the IF material indicated a significant change in texture as a result of the almost negligible additional reduction that occurred on the final rolling stand. One would have to conclude without any corroborative evidence that the observed change in texture is only a surface change due to the matte finish on the work rolls and is not consistent throughout the entire strip thickness. With the matte finish on the work rolls there is a different frictional interface causing higher than normal surface stress leading to localized crystallographic changes. The use of various matte finishes on the work rolls and even the effect of different work roll diameters could be the topic of further investigation.

5.5 - Slip mechanism

The observation by this investigation that the $\{111\}\langle 011\rangle$ orientation, at low reduction is the preferred orientation, but then replaced by the $\{111\}\langle 112\rangle$ orientation at higher reductions, provides good experimental support for Taylor's model for strain in the polycrystalline aggregate. The paper by Li, Diak, and Saimoto [15], describes the simulation of texture development in ultra-low carbon steel. The computer simulation uses the Taylor-Bishop-Hill full constraints model, that chooses, at each strain step, 5 out of 24 slip systems (refer to section 2.6 of this thesis) based on their Schmid factors. The results from their

simulation indicate that the $\{111\}\langle 110\rangle$ is a favorable orientation, but even more favorable, is the $\{111\}\langle 112\rangle$ orientation. This would explain why, in our investigation, at the early reductions, the $\{111\}\langle 110\rangle$ is favored, but then overtaken at the later reductions by the $\{111\}\langle 112\rangle$ orientation. Explained in terms of the Taylor model: with increased externally applied shape change, increased numbers of crystallites undergo a shape change such that 5 out of a possible 24 slips systems (whose total shear strain is a minimum) have been activated and which have incrementally favored the $\{111\}\langle 112\rangle$ orientation. In our investigation, at about 60 % reduction, enough crystallites have undergone a shape change and have oriented themselves in favor of the $\{111\}\langle 112\rangle$ texture.

Chapter 6 - Conclusions

1. This investigation provides support for the Taylor model of plastic strain for polycrystalline aggregates, as a valid explanation of the mechanism of texture development in cold rolling.
2. The predominant cold roll texture at all levels of reduction is {111} planes lying in the plane of the rolled sheet, followed by {100} and {211}. The texture {110} is almost non-existent.
3. There is a dip in the intensity of the {111} as well as the {100} textures at approximately 70 % reduction. This dip occurs in both Al-killed low carbon steel and Ti-stabilized IF steel. The intensity of both textures recovers at approximately 90 % reduction. There were no results for IF material at 90 % reduction.
4. A good indicator of the \bar{r} value that will develop in the fully processed steel is to compare the difference in intensity level of the {111} texture and the {100} texture in the corresponding cold roll material.
5. This difference in intensity level mentioned in point 4, is larger in IF steel than the Al-killed steel. This explains why IF steels have a higher \bar{r} value after recrystallization.
6. After approximately 70 % cold roll reduction the relative intensity between the {111} texture and the {100} texture is approximately 2.25. With increased cold roll reduction beyond 70 %, there is a minimal change in this relative intensity.

6.1 - Summary

Point 6 above is important and deserves elaboration. Mill and product constraints allow for few changes to the cold rolling schedule. Working within this limited window of opportunity yields minimal

variation in the final relative intensities of the two important orientations {111} and {100} in cold rolled steel. Consequently, at the commercial level, there is little opportunity for the metallurgical or process engineer to influence texture development and hence formability during the cold rolling stage.

6.2 - Further Investigation

- Investigate cold roll reduction of IF material up to 90 % reduction.
- Investigate through-thickness texture homogeneity at intermediate cold roll reductions.
- Investigate the effect of work roll surface roughness and work roll diameter on texture development.

References

1. S. Mishra, and C. Dürmann: *International Metals Reviews*, **27** (1982), 307.
2. G.J. Davies, D.J. Goodwill, and J.S. Kallend, *J. Appl. Cryst.*, **4** (1971), 67
3. R. Sowerby, 'A Mathematical Description of Texture in Metals', in 'Plasticity of Metals at Finite Strain: Theory, Experiment and Computation (ed. E.H. Lee and R.L. Mallett), 1981
4. M. Hatherly, and W.B. Hutchinson, 'An Introduction to Textures in Metals', Institute of Metals, 1988
5. L. Kestons, and J.J. Jonas, *ISIJ*, **37** (1997), 807
6. R. Grobterlinden, K. Imlau, R. Kawalla, U. Lotter, and C. Relp, *Steel Research*, **67** (1996), 456
7. R. Sowerby, C.S. Da C. Viana, and G.J. Davies, *Mat. Science and Eng.*, **46** (1980), 23
8. W.A. Backofen, W.F. Hosford Jr, and J.J. Burke, *ASM Trans.*, **55** (1962), 264
9. C.M. Van Der Walt, *Acta Metallurgica*, **17** (1969), 393
10. R.E. Smallman, 'Modern Physical Metallurgy', Butterworths, 4th ed., 1985
11. I.L. Dillamore, and H. Katoh, *Metal Science*, **8** (1974), 21
12. I.S. Brammar, T.R. Thomson, and R.M. Hobbs, *J. Aust. Inst. Met.*, **17** (1972), 147
13. U.F. Kocks, *Met. Trans.*, **1** (1970), 1121
14. G.I. Taylor, *J. Inst. Met.*, **62** (1938), 307
15. Jian Li, B. J. Diak, and S. Saimoto, Queen's University, paper not yet published
16. W. Johnson, R. Sowerby, and R. Venter, 'Plane Strain Slip Line Fields ...', Pergamon, 1982
17. R.J. Roe, *J. Appl. Phys.*, **6** (1965), 2024
18. W.A. Backofen, 'Deformation Processing', Addison-Wesley, 1972
19. C.S. Barrett, and L.H. Levenson, *Metals Technology*, (1940), 281
20. F. Wever, *Trans. A.I.M.I.*, **93** (1931), 51
21. M. Gensamer, and R.F. Mehl, *Trans. A.I.M.E* **120** (1936), 277
22. C.B. Post, *Trans. Amer. Soc. Metals*, **24** (1936), 679
23. W.A. Sisson, *Metals and Alloys*, **4** (1933), 193
24. R.L. Whiteley, and D.E. Wise, "Flat Products III", *A.I.M.E.*, 1962

25. I.S. Brammar, T.R. Thomson, and R.M. Hobbs, *J. Aust. Inst. Met.*, **17** (1972), 147
26. R.K.P. Singh, K.A. Padmanabhan, and S. Mishra, *ASME*, **2** (1994), 583
27. M.H. Lawry, "I-DEAS Master Series 2.0", Structural Dynamics Research Corporation, 1994
28. H.J. Bunge, *Z. Metallkd.*, **56** (1965), 872
29. G.Y. Chin, W.L. Mammel, M.T. Dolan, *Transactions of the Metallurgical Society of AIME*, **239** (1967), 1854
30. L. G. Schulz, *J. Appl. Phys.*, **20** (1949), 1039
31. B. D. Cullity, "Elements of X-ray Diffraction", Addison-Wesley, 1956
32. J. A. Elias and A. J. Heckler, *Trans. Metall. Soc. AIME*, **239** (1967), 1237
33. U. Lotter, W. Mueschenborn, R. Knorr, *Textures of Materials*, **2** (1978), 285
34. R. Hill, *Proc. Roy. Society*, 193A (1948), 281
35. W.F. Hosford, 7th North American Metalworking Research Conf., 191, SME (1979)
36. W.F. Hosford and R.M. Caddell, "Metal Forming:- Mechanics and Metallurgy" 2nd Ed., PTR Prentice Hall Inc., (1993)
37. F. Barlat, R.C. Becker, Y. Hayashida, Y. Maeda, M. Yanagawa, K. Chung, J.C. Brem, D.J. Lege, K. Matsui, S.J. Murtha, and S. Hattori, *Int. J. Plasticity*, **13** (1997), 383
38. J.W.F. Bishop and R. Hill, *Phil. Mag.*, **42** (1951), 414 and 1298
39. G.I. Taylor and C.F. Elam, *Proc. Roy. Soc. London*, A102 (1923), 643

Appendix A

The following diagram was duplicated from the paper by R. Sowerby, 'A Mathematical Description of Texture in Metals', found in the proceedings of the 'Plasticity of Metals at Finite Strain: Theory, Experiment and Computation' workshop, July 1981.

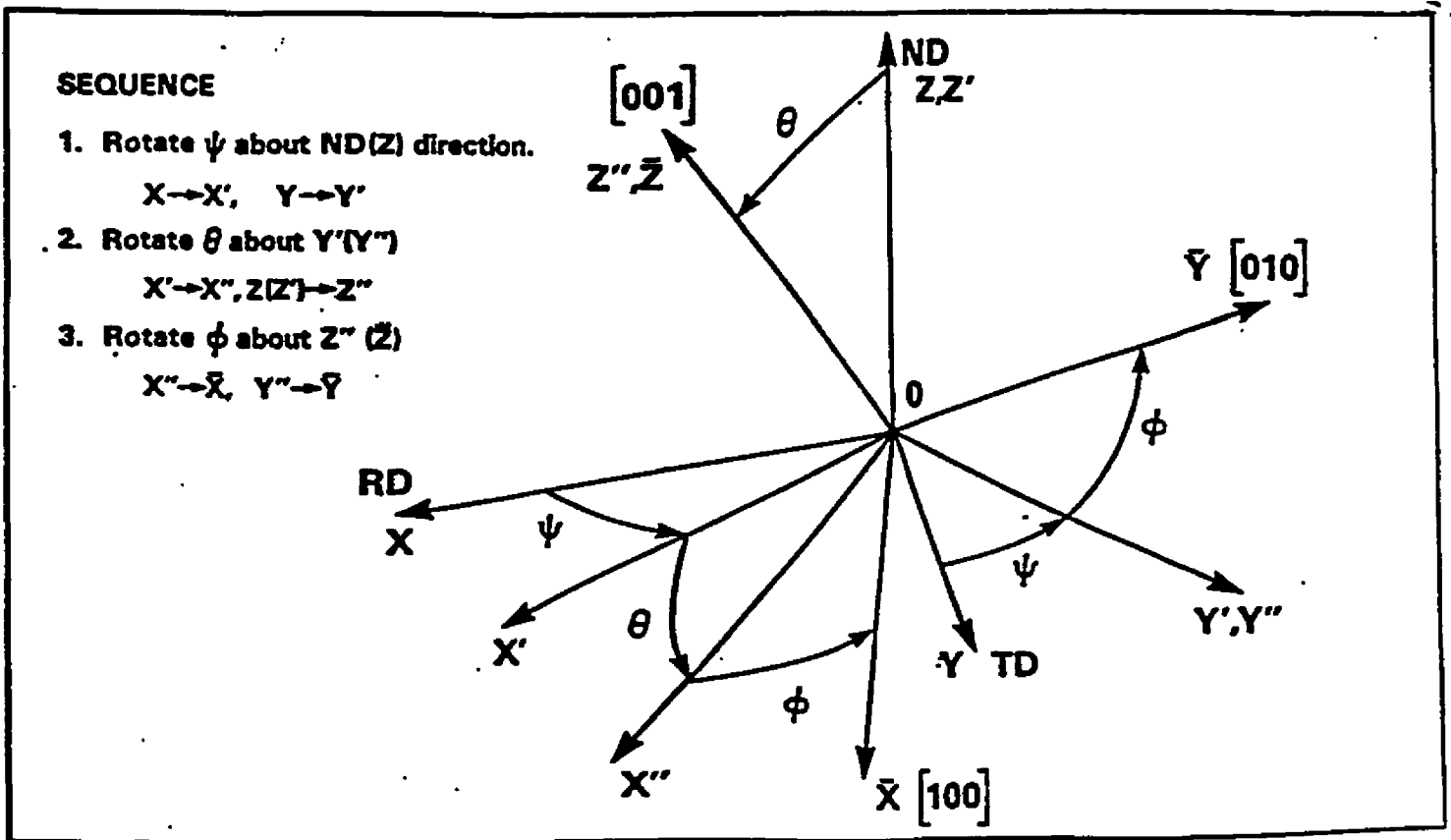


FIG. 1 - DEFINITION OF EULER ANGLES

It is also helpful to be able to relate Miller indices to Euler angles and vice versa, specifically when attempting to interpret the CODF results in terms of common orientations with known Miller indices. Equations taken from the paper by Davies, Goodwill, and Kallend [2] are useful for the above reason and are provided below.

If the Miller indices are provided as (hkl)[uvw], they correspond to the Euler angles as follows:

$$\cos \psi = \frac{w}{(u^2 + v^2 + w^2)^{1/2}} \cdot \frac{(h^2 + k^2 + l^2)^{1/2}}{(h^2 + k^2)^{1/2}} \quad (h, k \neq 0)$$

$$\cos \theta = \frac{l}{(h^2 + k^2 + l^2)^{1/2}}$$

$$\cos \phi = \frac{-h}{(h^2 + k^2)^{1/2}} \quad (h, k \neq 0)$$

For the special case in which $h=k=0$ then:

$$\cos (\psi + \phi) = \frac{u}{(u^2 + v^2 + w^2)^{1/2}}$$

Alternatively, an ideal orientation can be found from known Euler angles using

$$h = -\sin \theta \cos \phi \quad k = \sin \theta \sin \phi \quad l = \cos \theta$$

$$u = \cos \psi \cos \theta \cos \phi - \sin \psi \sin \phi$$

$$v = -\cos \psi \cos \theta \sin \phi - \sin \psi \cos \phi$$

$$w = \cos \psi \sin \theta$$

and rationalizing the resulting indices.

Appendix B

As described in chapter 3, samples were taken from the strip as it was processed through the tandem cold mill and texture measurements taken from the samples. This procedure was repeated on six different occasions for six different coils of steel. The results from these texture measurements for two of these six coils are contained in the following pages. The pages that follow are in sequence and are as follows:

<u>Label</u>	<u>Designation</u>
#1 – HB (211)	- coil #1 hot band (i.e. material entering the cold mill), (211) pole figure
#1 – HB (111)	- coil #1 hot band, (111) pole figure
#1 – HB (200)	- coil #1 hot band, (200) pole figure
#1 – HB (110)	- coil #1 hot band, (110) pole figure
#1 – HB	- coil #1 hot band, CODF
#1 – CR1 (211)	- coil #1 after first cold roll stand, (211) pole figure
#1 – CR1 (111)	- coil #1 after first cold roll stand, (111) pole figure
#1 – CR1 (200)	- coil #1 after first cold roll stand, (200) pole figure
#1 – CR1 (110)	- coil #1 after first cold roll stand, (110) pole figure
#1 – CR1	- coil #1 after first cold roll stand, CODF
#1 – CR2 (211)	- coil #1 after second cold roll stand, (211) pole figure
#1 – CR2 (111)	- coil #1 after second cold roll stand, (111) pole figure
#1 – CR2 (200)	- coil #1 after second cold roll stand, (200) pole figure
#1 – CR2 (110)	- coil #1 after second cold roll stand, (110) pole figure
#1 – CR2	- coil #1 after second cold roll stand, CODF

#1 – CR3 (211) - coil #1 after third cold roll stand, (211) pole figure
#1 – CR3 (111) - coil #1 after third cold roll stand, (111) pole figure
#1 – CR3 (200) - coil #1 after third cold roll stand, (200) pole figure
#1 – CR3 (110) - coil #1 after third cold roll stand, (110) pole figure
#1 – CR3 - coil #1 after third cold roll stand, CODF

#1 – CR4 (211) - coil #1 after fourth cold roll stand, (211) pole figure
#1 – CR4 (111) - coil #1 after fourth cold roll stand, (111) pole figure
#1 – CR4 (200) - coil #1 after fourth cold roll stand, (200) pole figure
#1 – CR4 (110) - coil #1 after fourth cold roll stand, (110) pole figure
#1 – CR4 - coil #1 after fourth cold roll stand, CODF

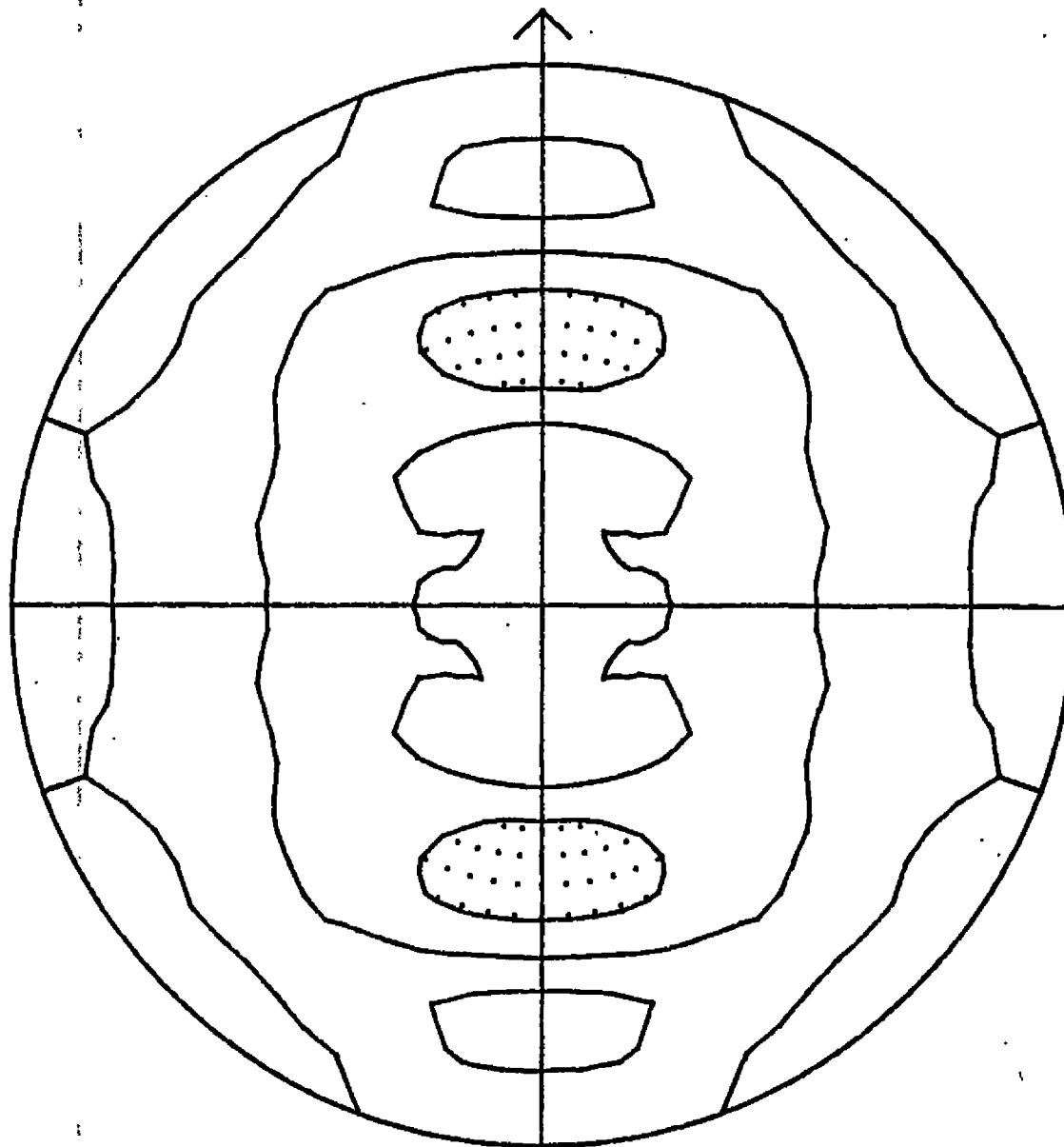
#1 – CR5 (211) - coil #1 after last cold roll stand, (211) pole figure
#1 – CR5 (111) - coil #1 after last cold roll stand, (111) pole figure
#1 – CR5 (200) - coil #1 after last cold roll stand, (200) pole figure
#1 – CR5 (110) - coil #1 after last cold roll stand, (110) pole figure
#1 – CR5 - coil #1 after last cold roll stand, CODF

#2 – HB (211) - coil #2 hot band (i.e. material entering the cold mill), (211) pole figure
etc. - see above but now for coil #2

A word of explanation for reading the following pole figures and CODF's: the version of the software that was used to generate the figures was not current. It was an older version that was not user friendly. Consequently, both the pole figures as well as the CODF's show only the contour lines with no labels. There is only a legend at the bottom of the figure that indicates the intensity values of the contour lines found on the figure, where the intensity values are given in terms of "n times random" (refer to section 3.3.1 for a definition of "times random"). It is left to the experience of the reader to relate the

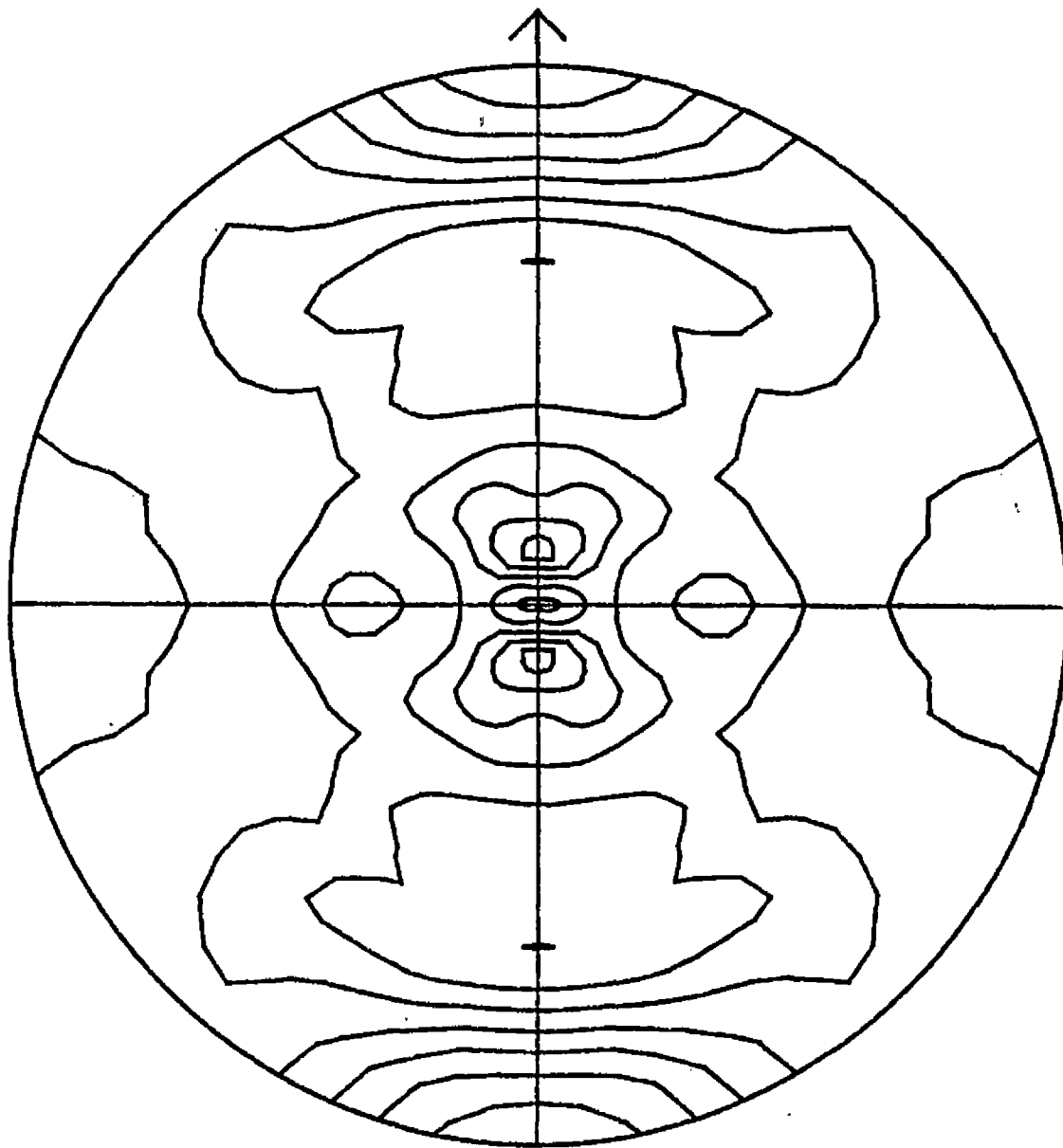
intensity value against the correct contour line. It is helpful to note that in the pole figures, the area that is designated with chain dotted lines is the area of lowest intensity.

To read the CODF's, the reader is completely on his own without even an area of chain dotted lines. The reader must rely on his or her knowledge of where high or low intensities should lie and use this knowledge as a starting point to relate the intensity level to the correct contour line. The designations ψ , θ , and ϕ^2 on the CODF's refer to the Euler angles ψ , θ , and ϕ respectively (refer to section 2.2 and Appendix A).



#1-HB
recalc. pole figure 23-NOV-95
(211) Stereographic Projection
Contours at .80 1.00 1.20

28-NOV-95
. Expanded



#1-HB

28-NOV-95

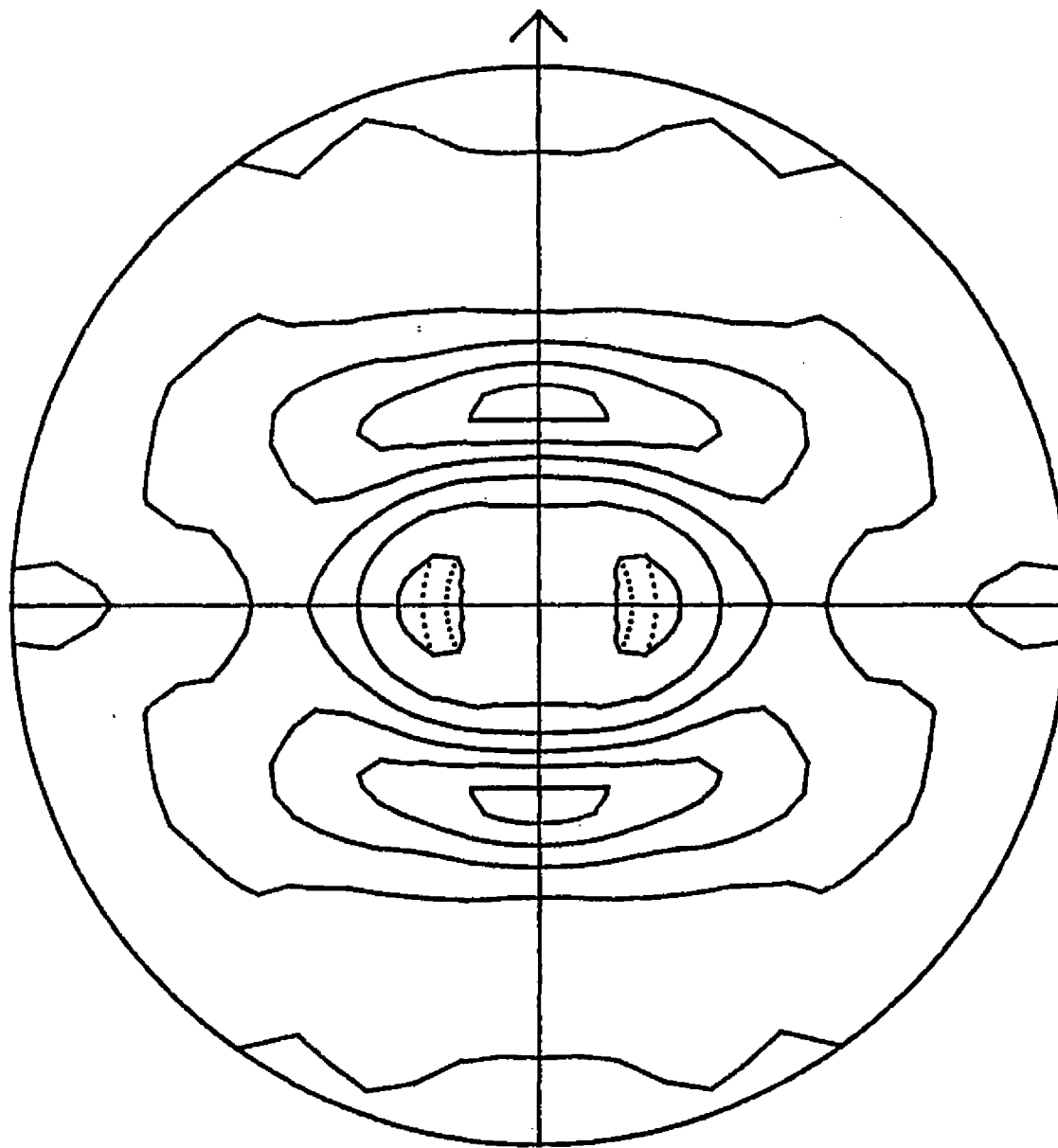
recalc. pole figure 23-NOV-95

. Expanded

(111) Stereographic Projection

0

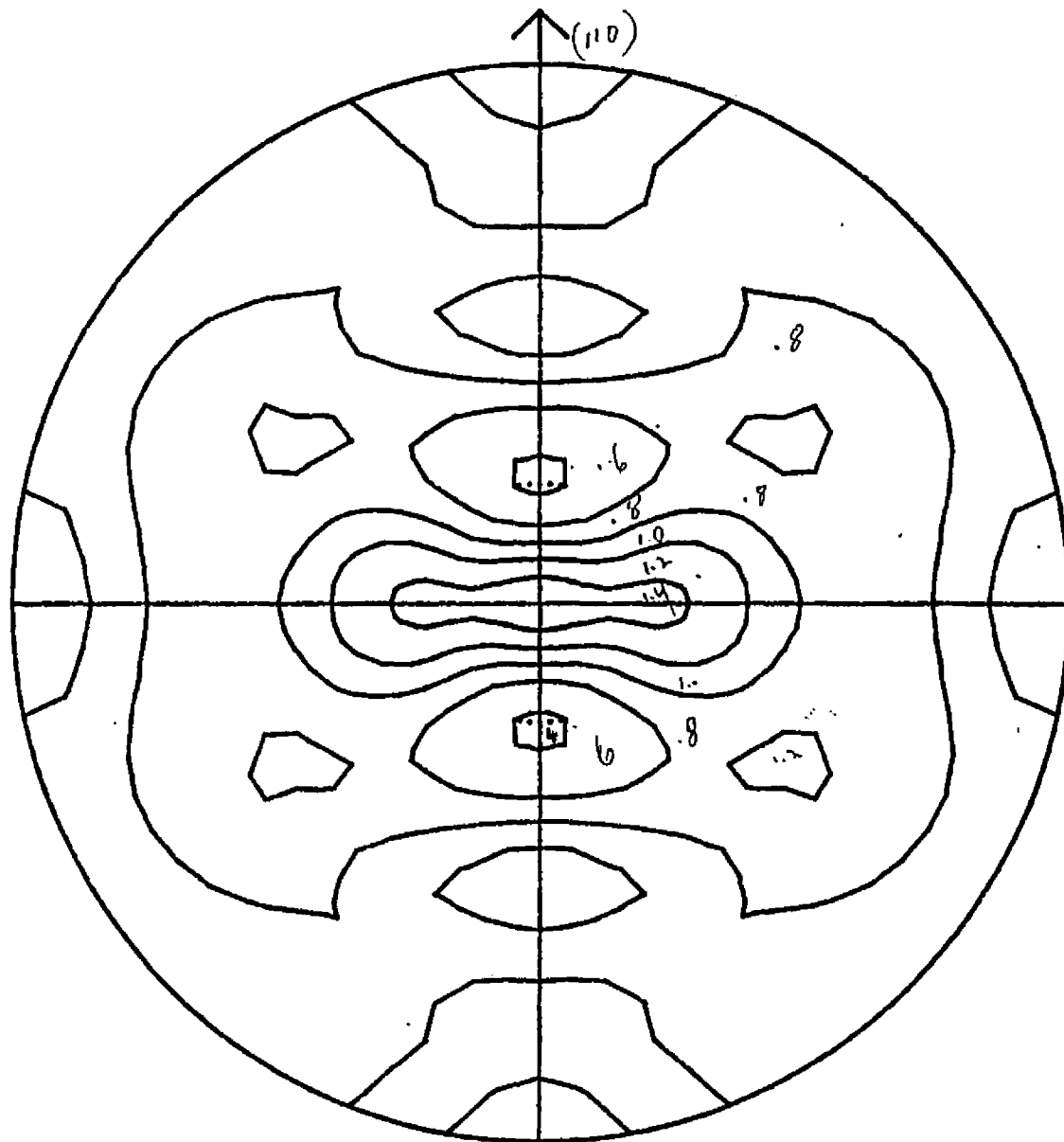
Contours at 50 75 1.00 1.25 1.50 1.75 2.00



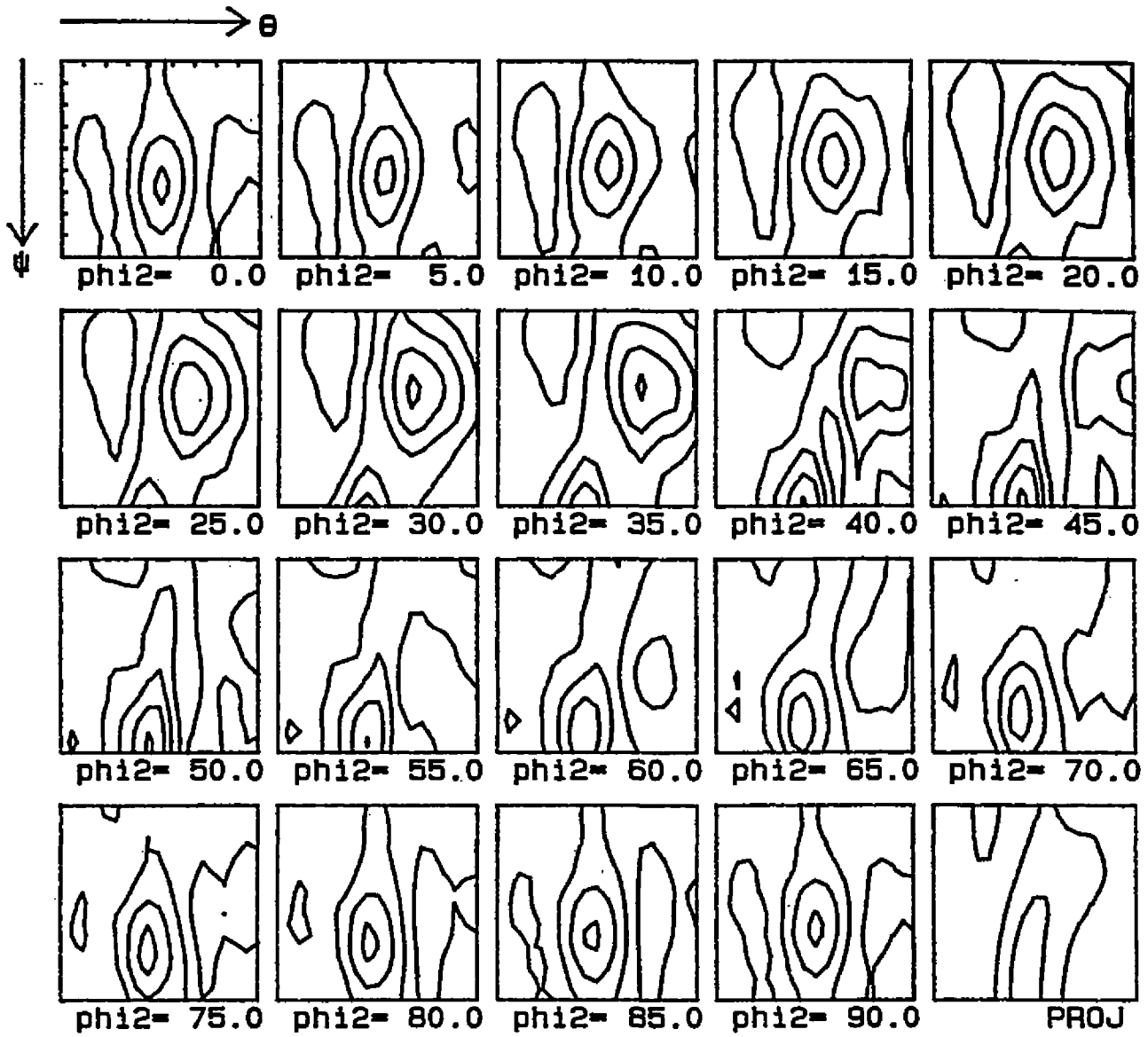
#1-HB
recalc. pole figure 23-NOV-95
(200) Stereographic Projection

28-NOV-95
, Expanded

--- -- : -- : 25 : 50 : 75

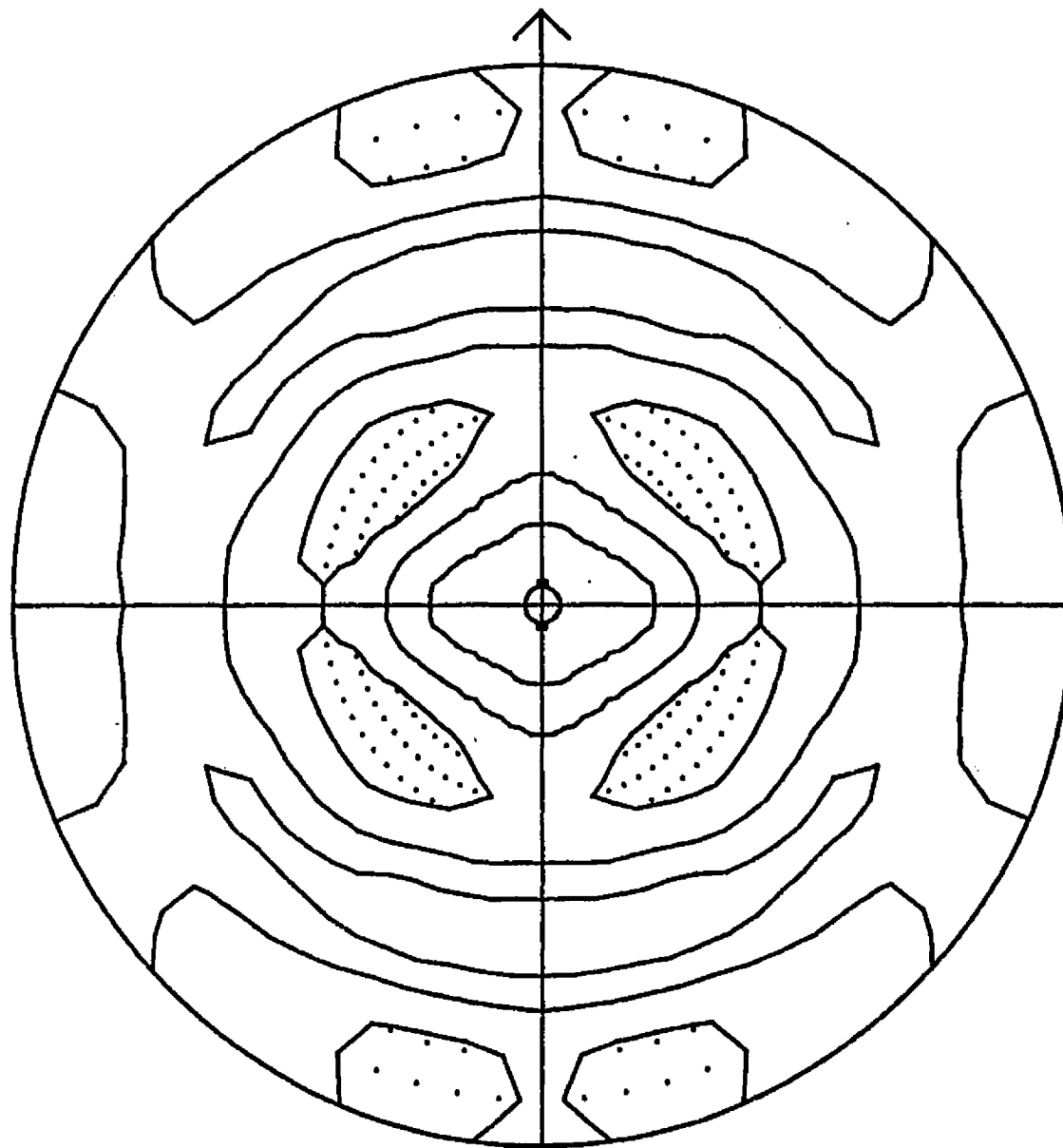


#1-HB 28-NOV-95
 recal. pole figure23-NOV-95 . Expanded
 (110) Stereographic Projection D
 Contours at .60 .80 1.00 1.20 1.40



#1-HB

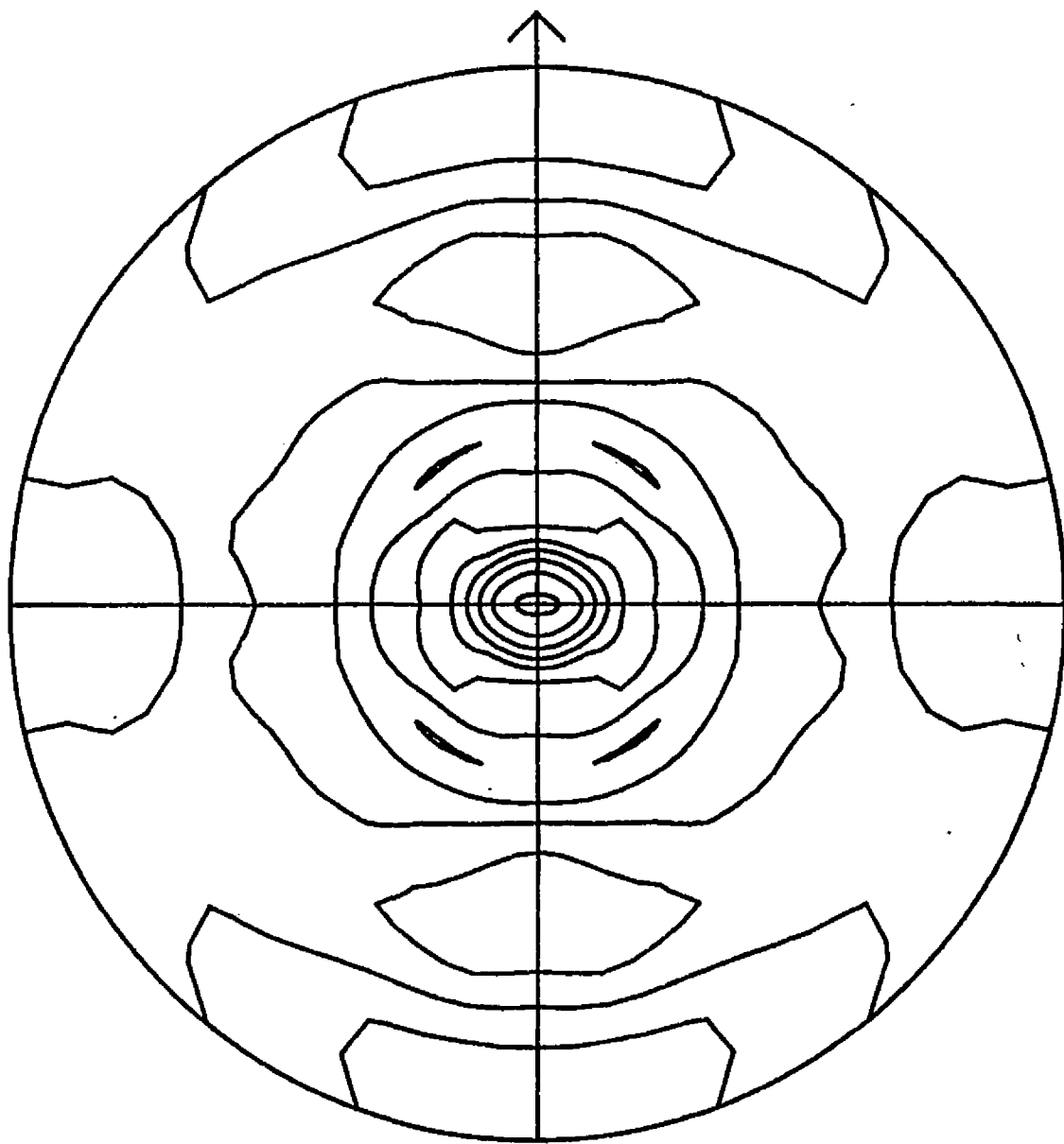
Contours at .50 1.00 1.50 2.00 2.50



#1-CR1
recalc. pole figure 24-NOV-95
(211) Stereographic Projection

24-NOV-95
, Expanded

0

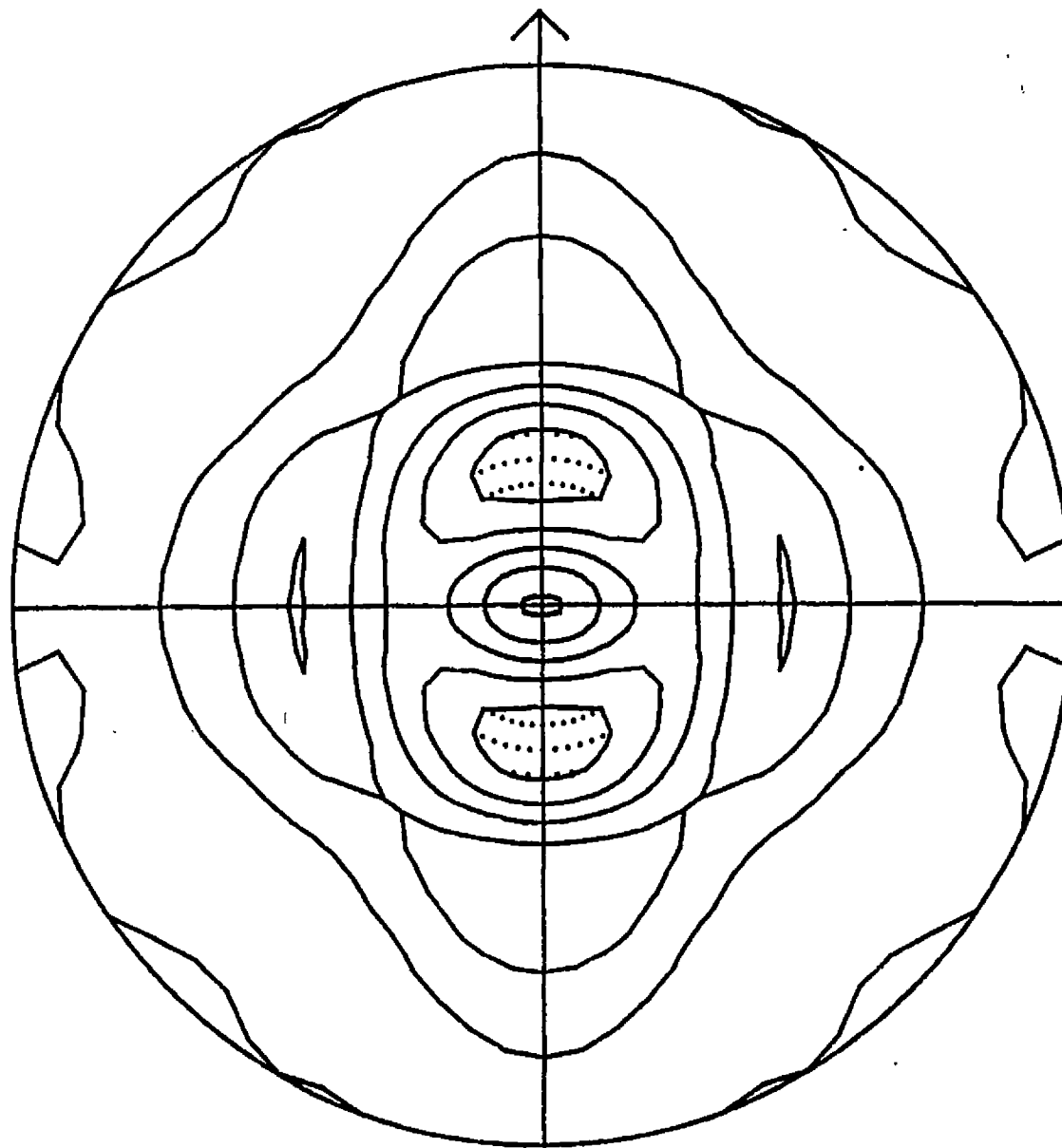


#1-CR1
recalc. pole figure 24-NOV-95
(111) Stereographic Projection

24-NOV-95
. Expanded

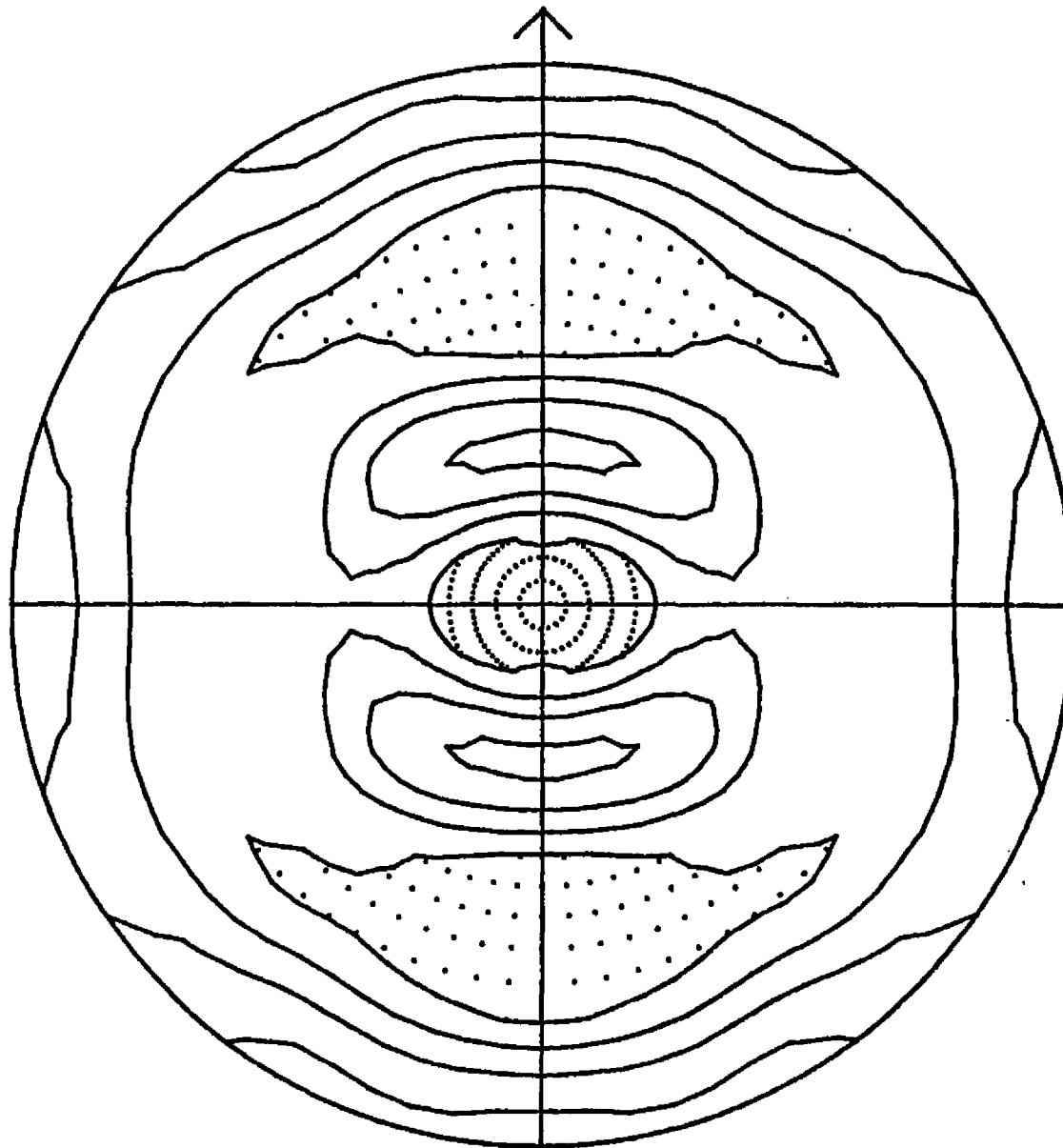
0

0 25 50 75 100 125 150 175 200 225 250



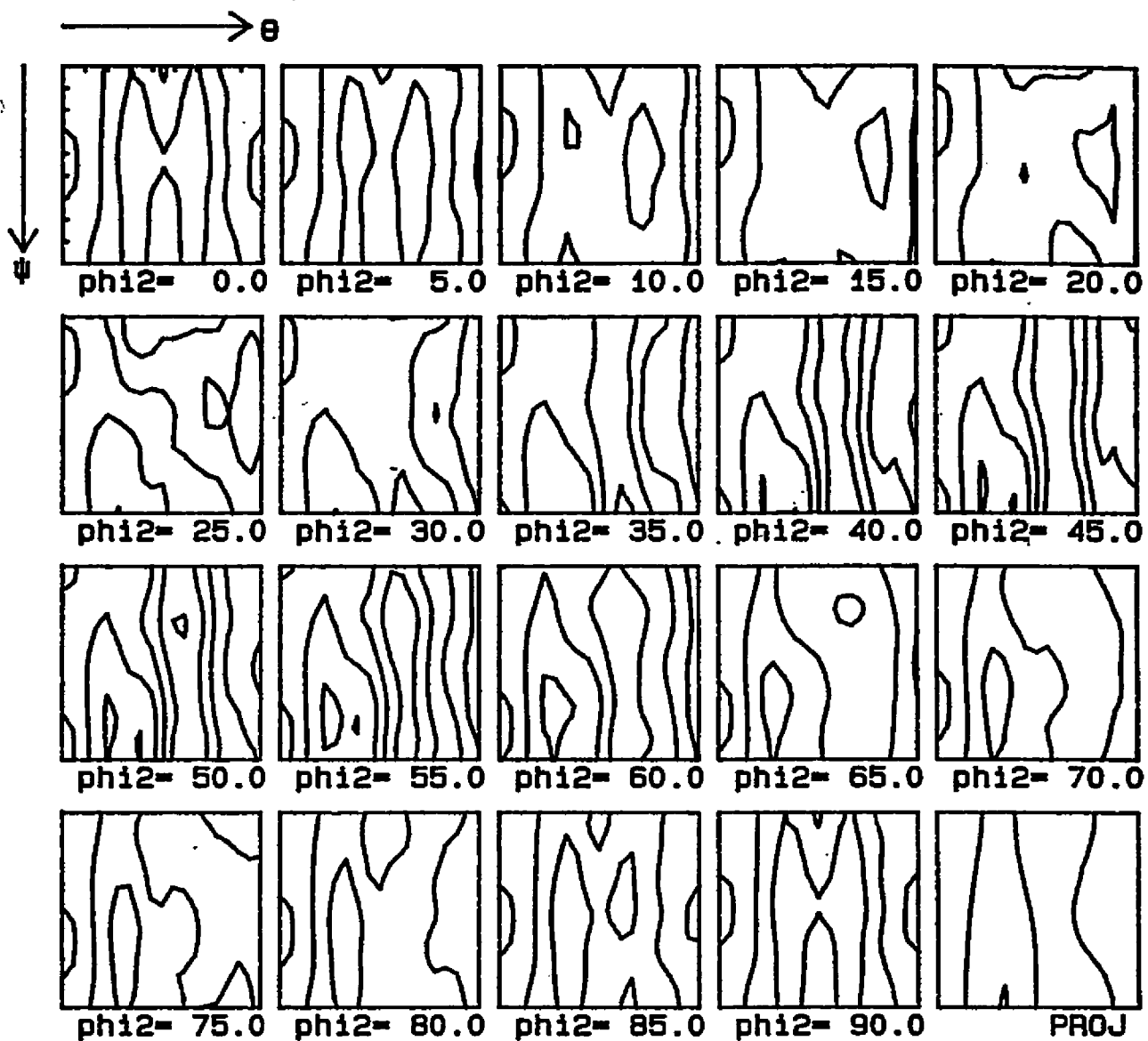
#1-CR1
recalc. pole figure24-NOV-95
(200) Stereographic Projection
Contours at .60 .80 1.00 1.20 1.40

24-NOV-95
. Expanded



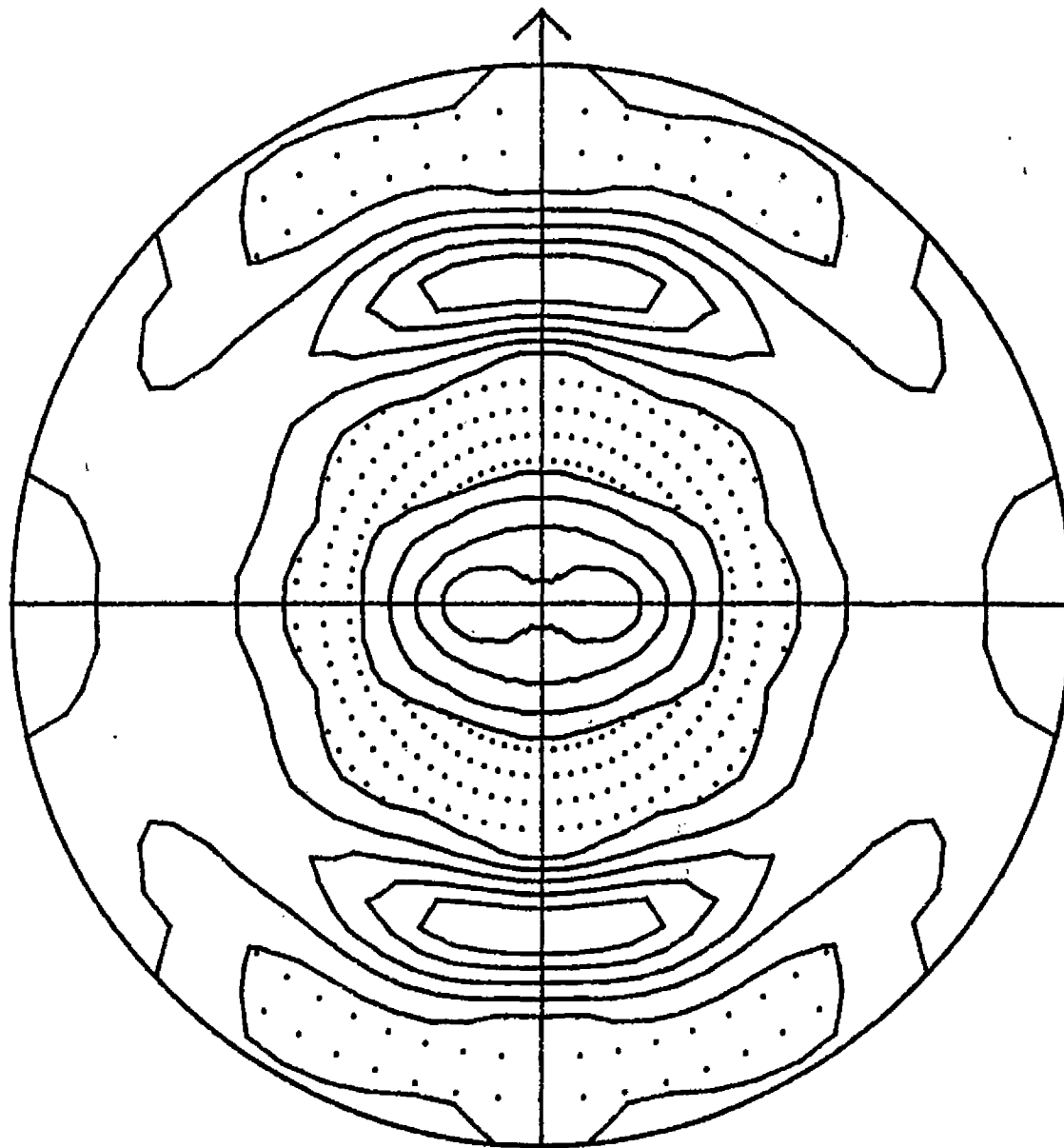
#1-CR1
recalc. pole figure 24-NOV-95
(110) Stereographic Projection
Contours at .80 1.00 1.20 1.40

24-NOV-95
. Expanded



#1-CR1

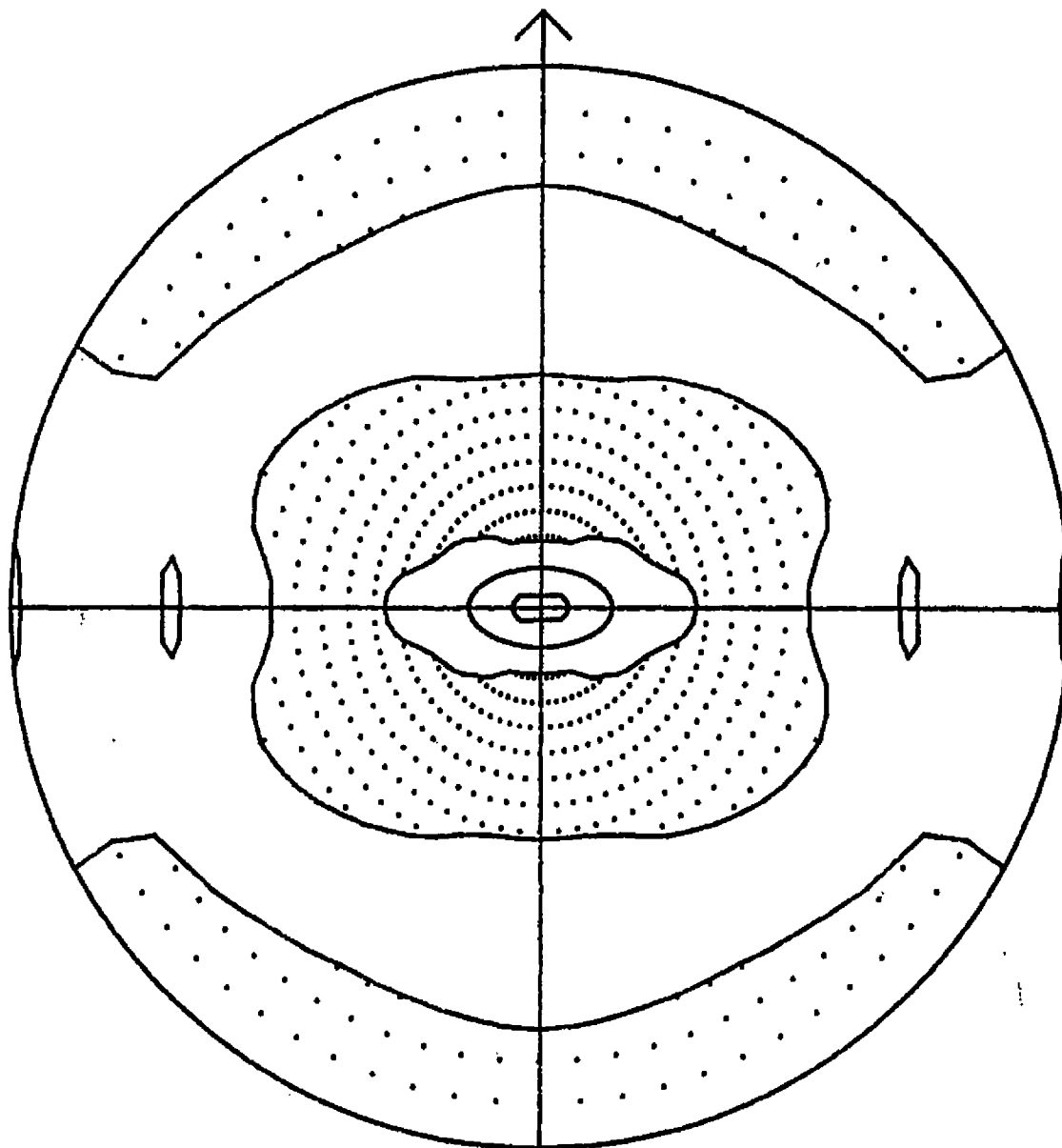
Contours at .50 1.00 1.50 2.00 2.50



#1-CR2
recalc. pole figure 28-NOV-95
(211) Stereographic Projection
Contours at .90 1.00 1.10 1.20 1.30

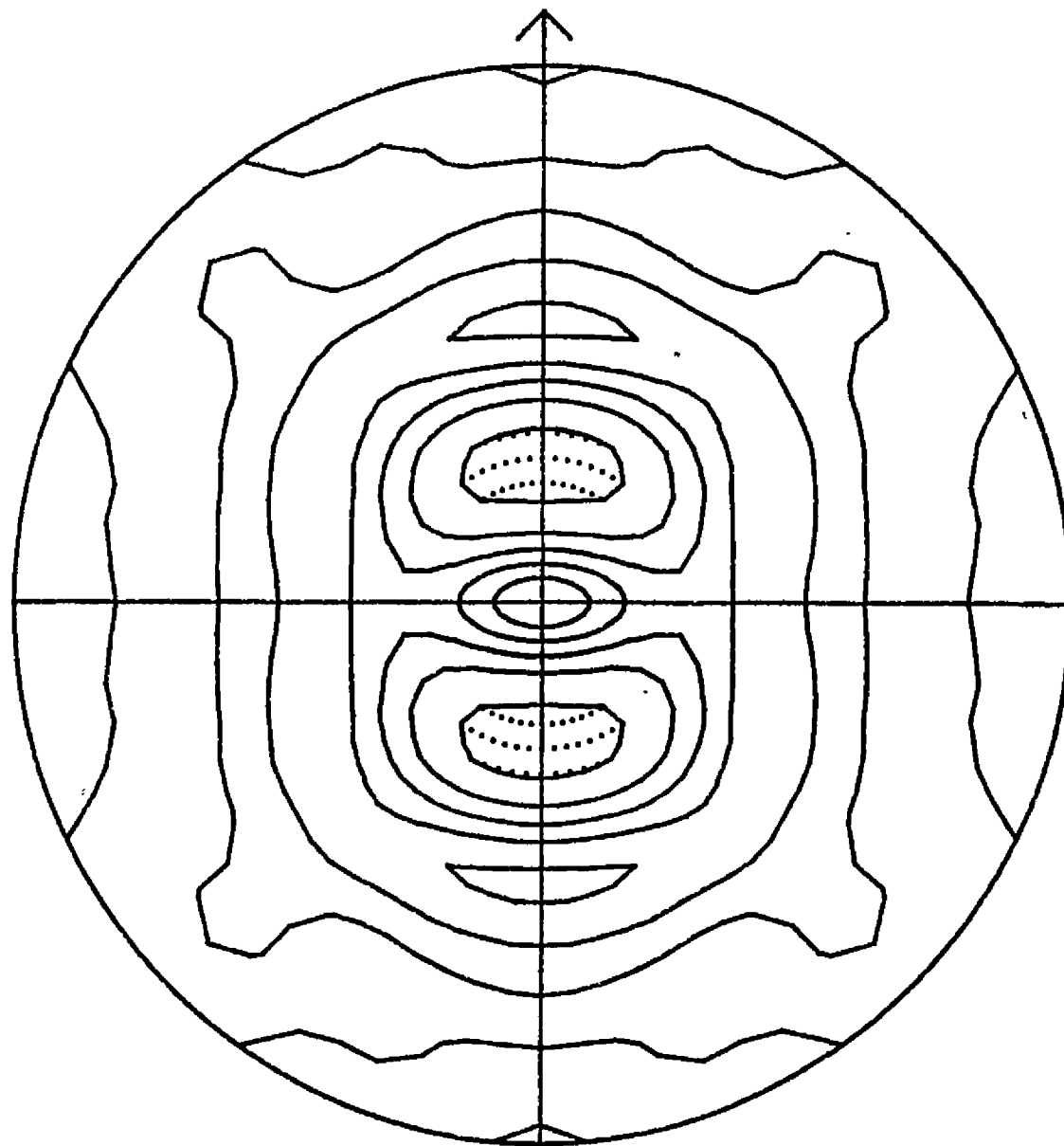
28-NOV-95
. Expanded

11



#1-CR2
recalc. pole figure 28-NOV-95
(111) Stereographic Projection
Contours at 1 2 3

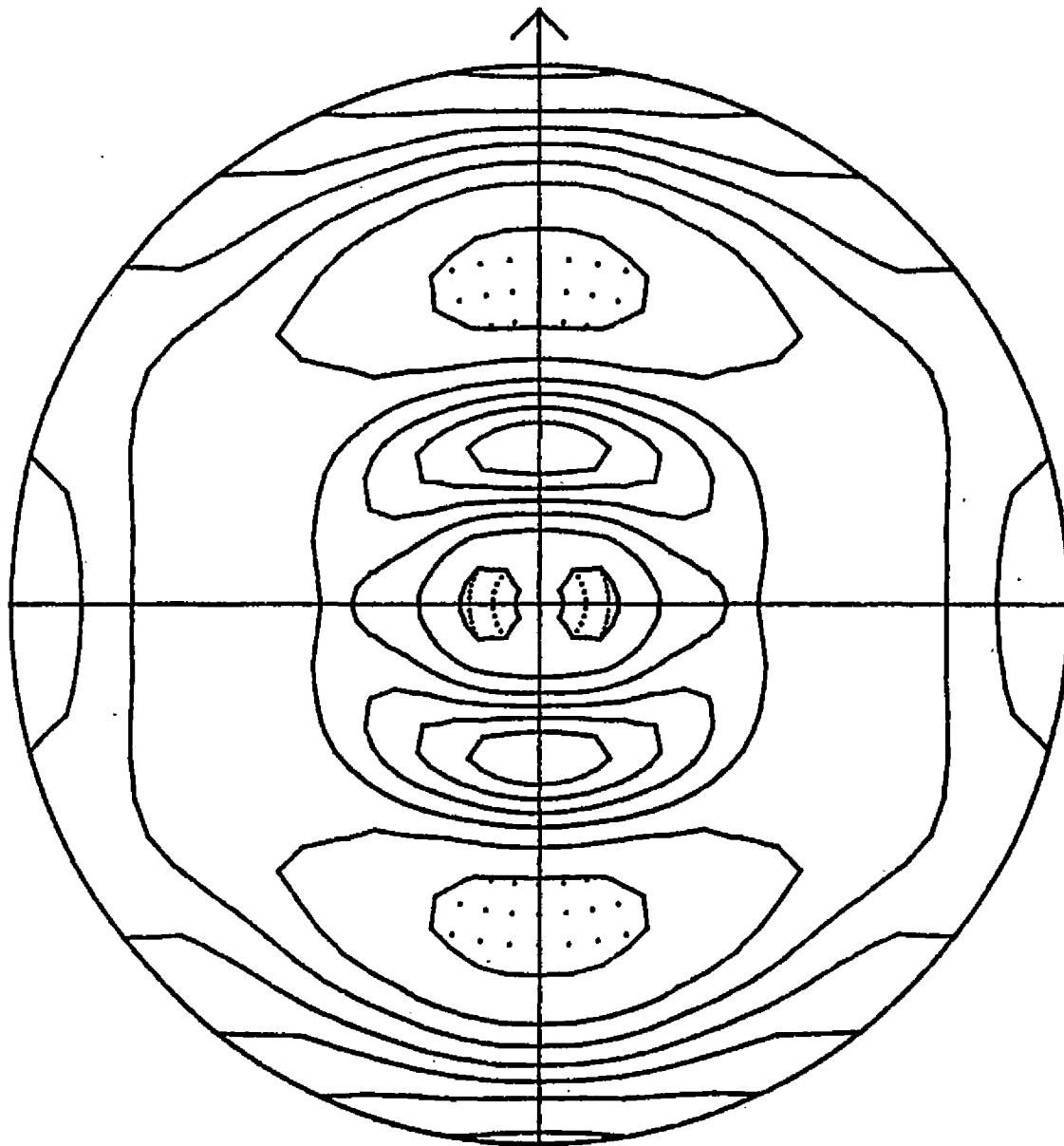
28-NOV-95
. Expanded



#1-CR2
recalc. pole figure 28-NOV-95
(200) Stereographic Projection
Contours at .50 .75 1.00 1.25 1.50

28-NOV-95
, Expanded

a



#1-CR2

28-NOV-95

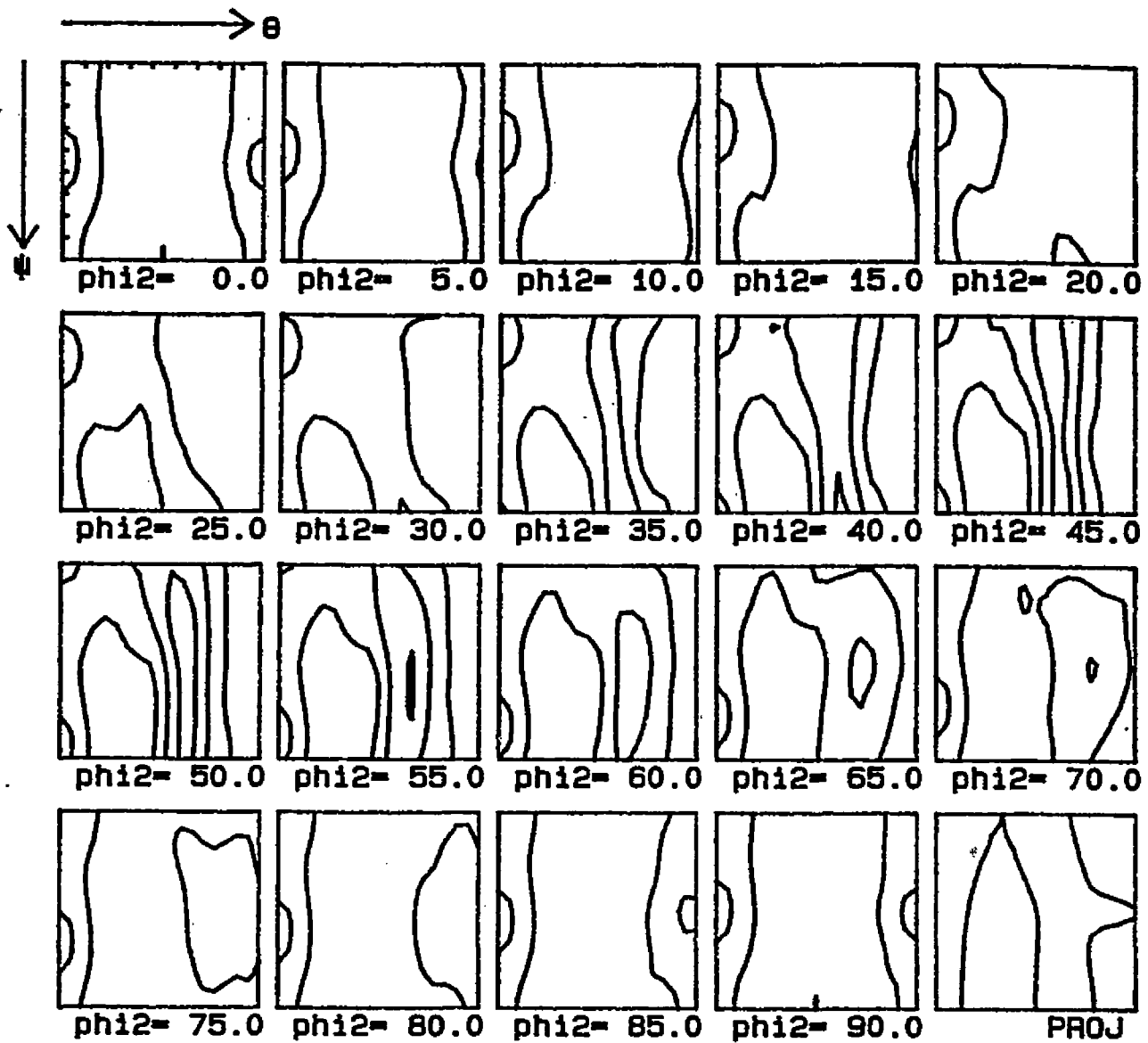
recalc. pole figure 28-NOV-95

. Expanded

(110) Stereographic Projection

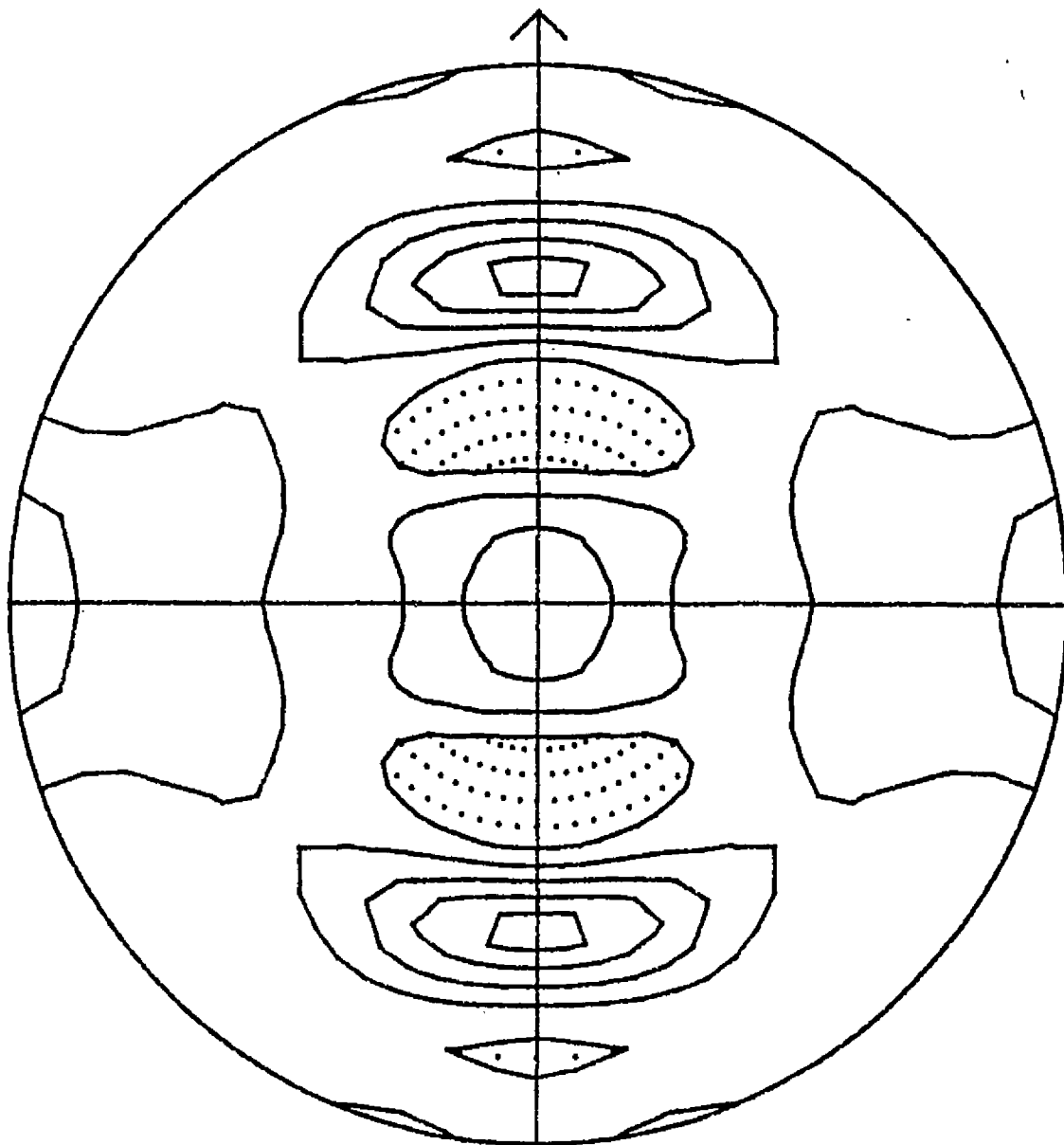
D

Contours at 50 75 1.00 1.25 1.50 1.75 2.00



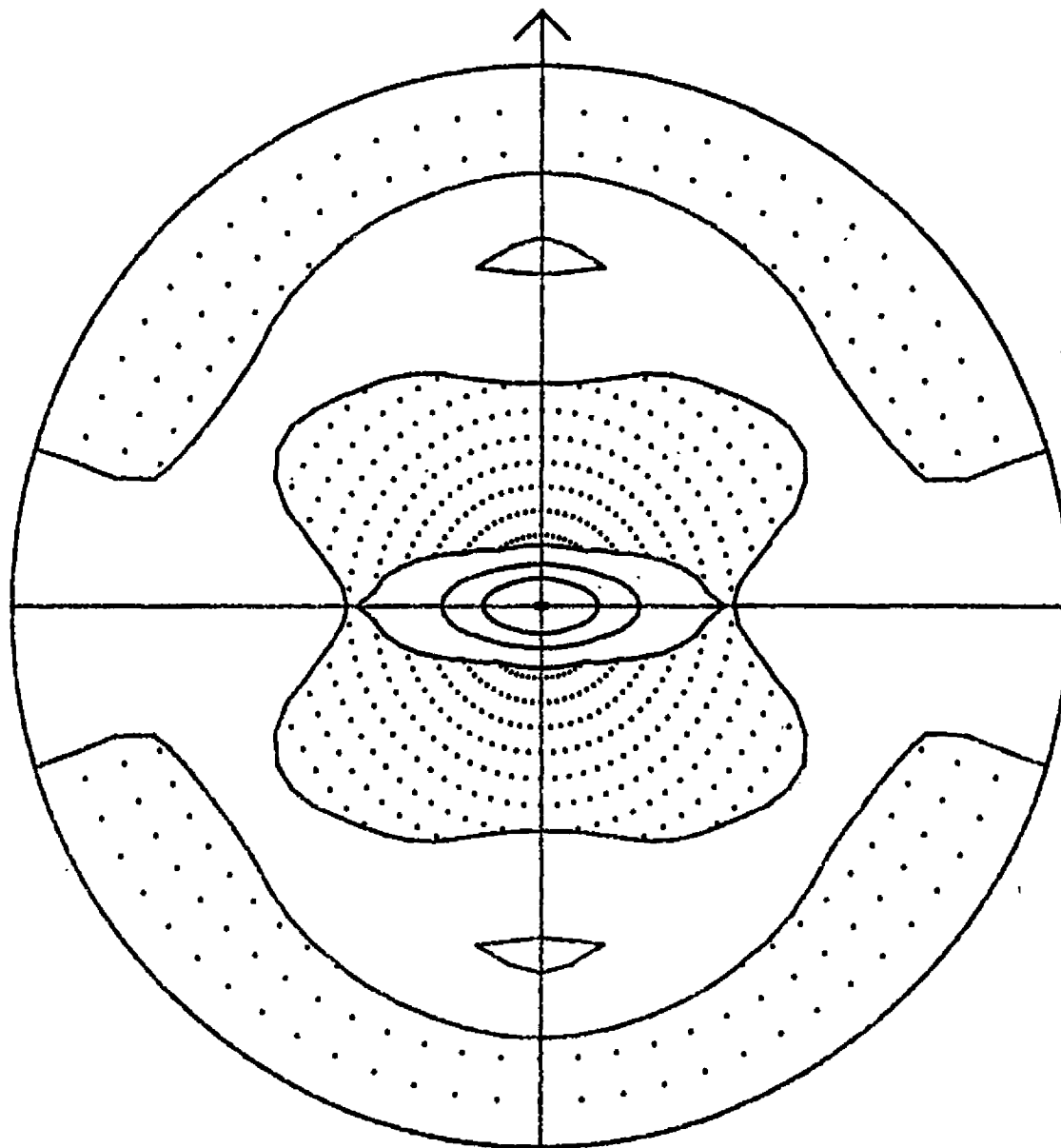
#1-CR2

Contours at 1 2 3



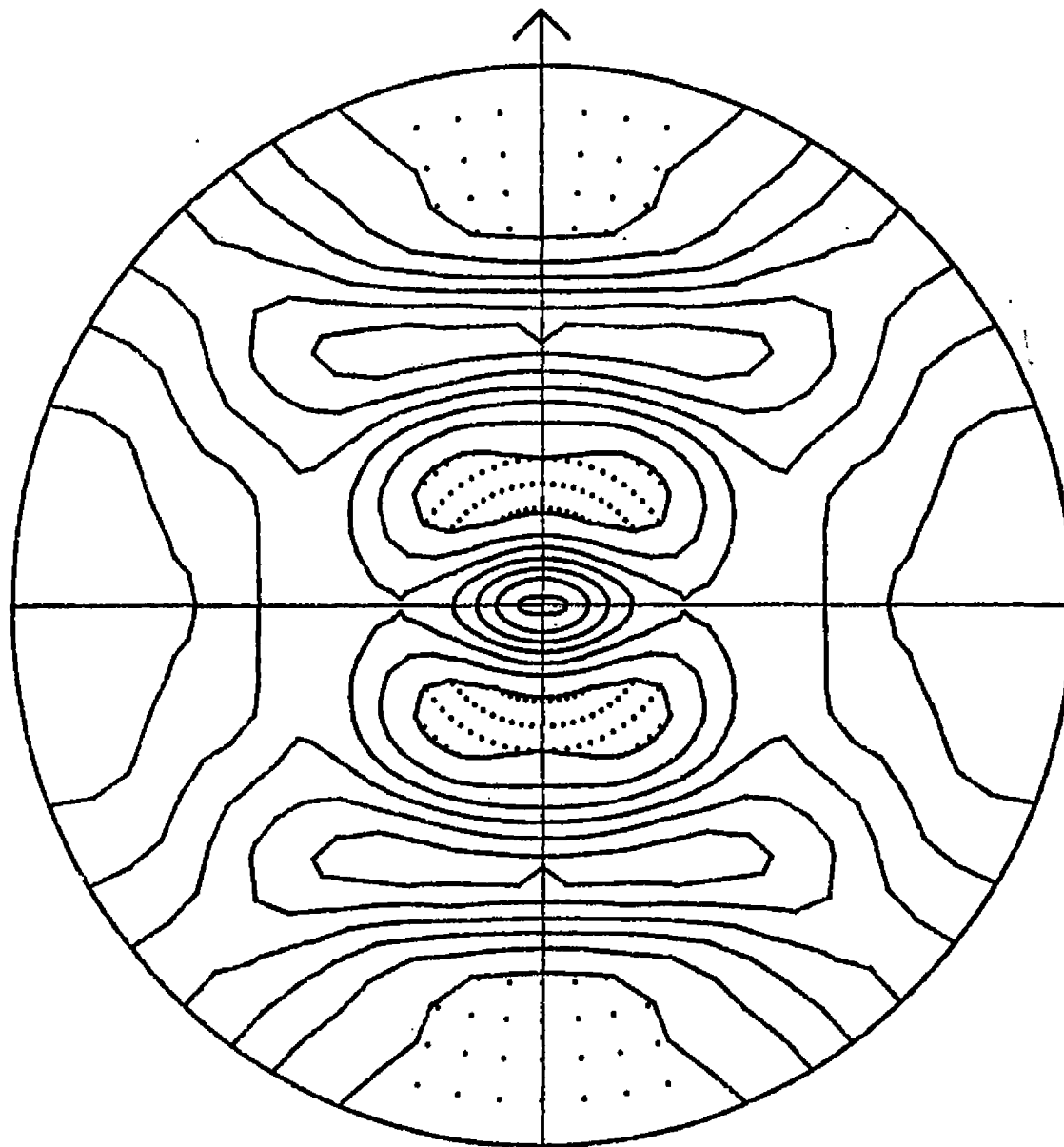
#1-CR3
recalc. pole figure 28-NOV-95
(211) Stereographic Projection
Contours at .80 1.00 1.20 1.40 1.60

28-NOV-95
. Expanded



#1-CR3
recalc. pole figure 28-NOV-95
(111) Stereographic Projection
Contours at 1 2 3 4

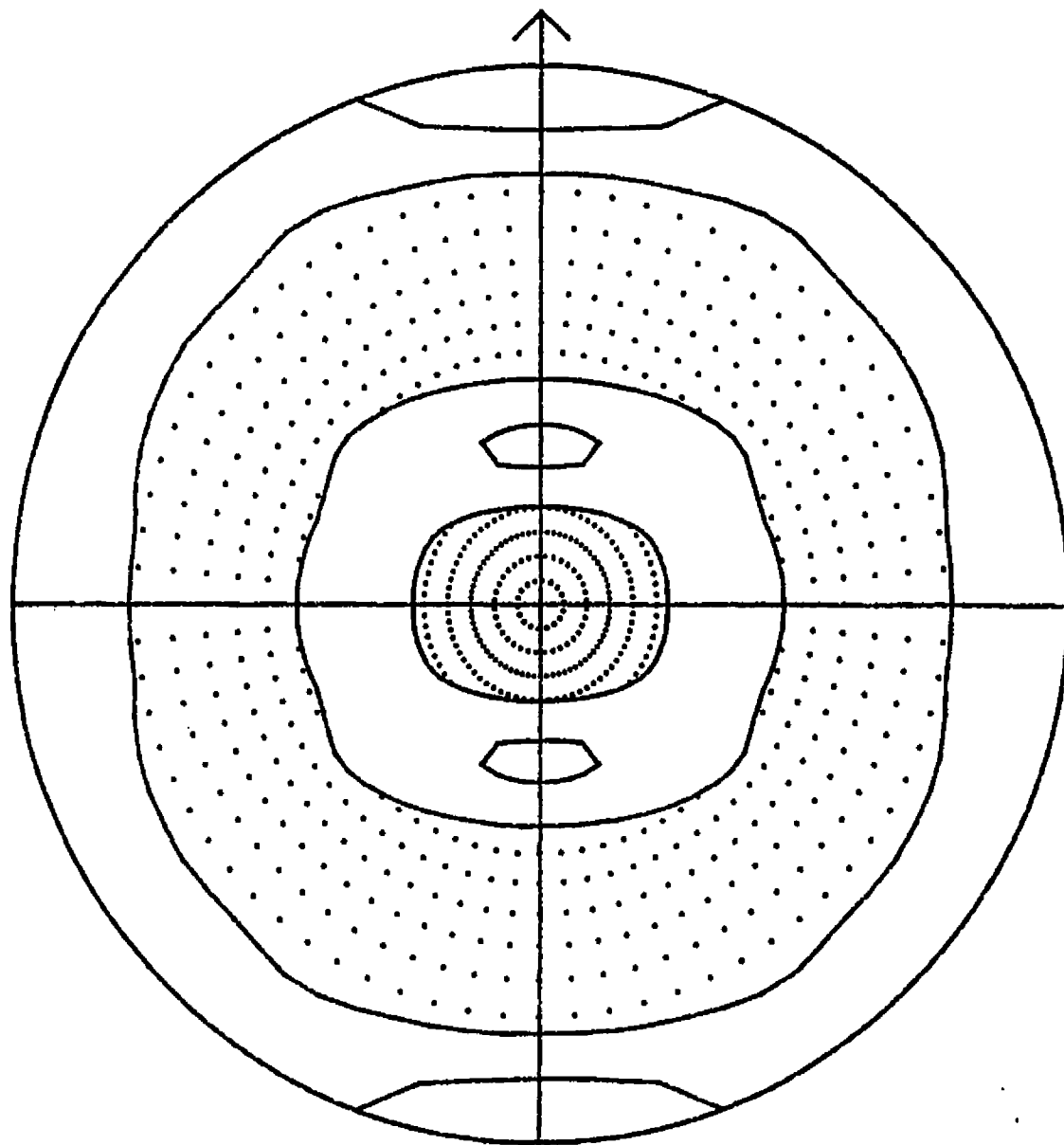
28-NOV-95
, Expanded



#1-CR3
recalc. pole figure 28-NOV-95
(200) Stereographic Projection

28-NOV-95
. Expanded

Contours at .50 .75 1.00 1.25 1.50 1.75 2.00



#1-CR3

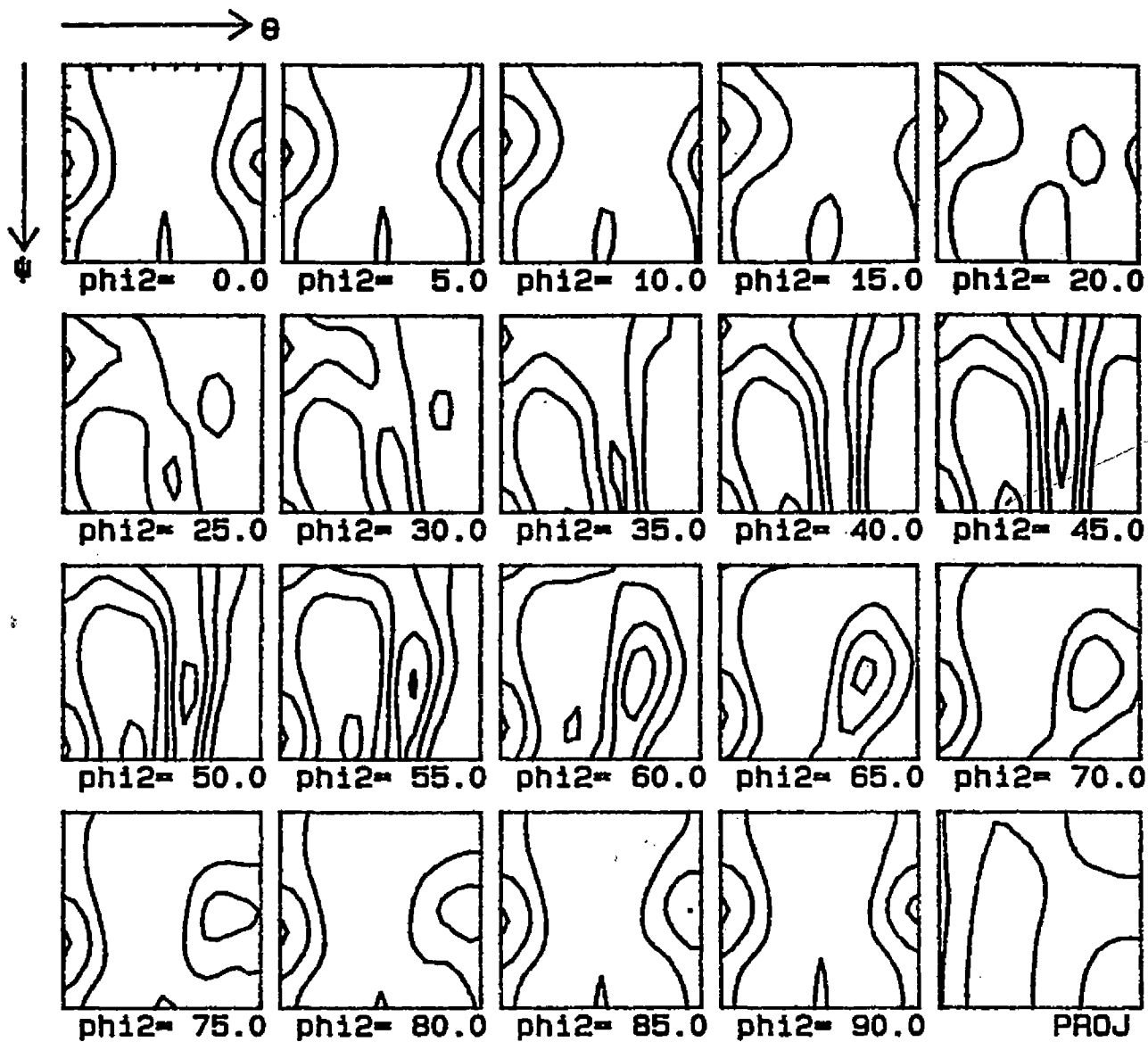
recalc. pole figure 28-NOV-95
(110) Stereographic Projection

28-NOV-95

. Expanded

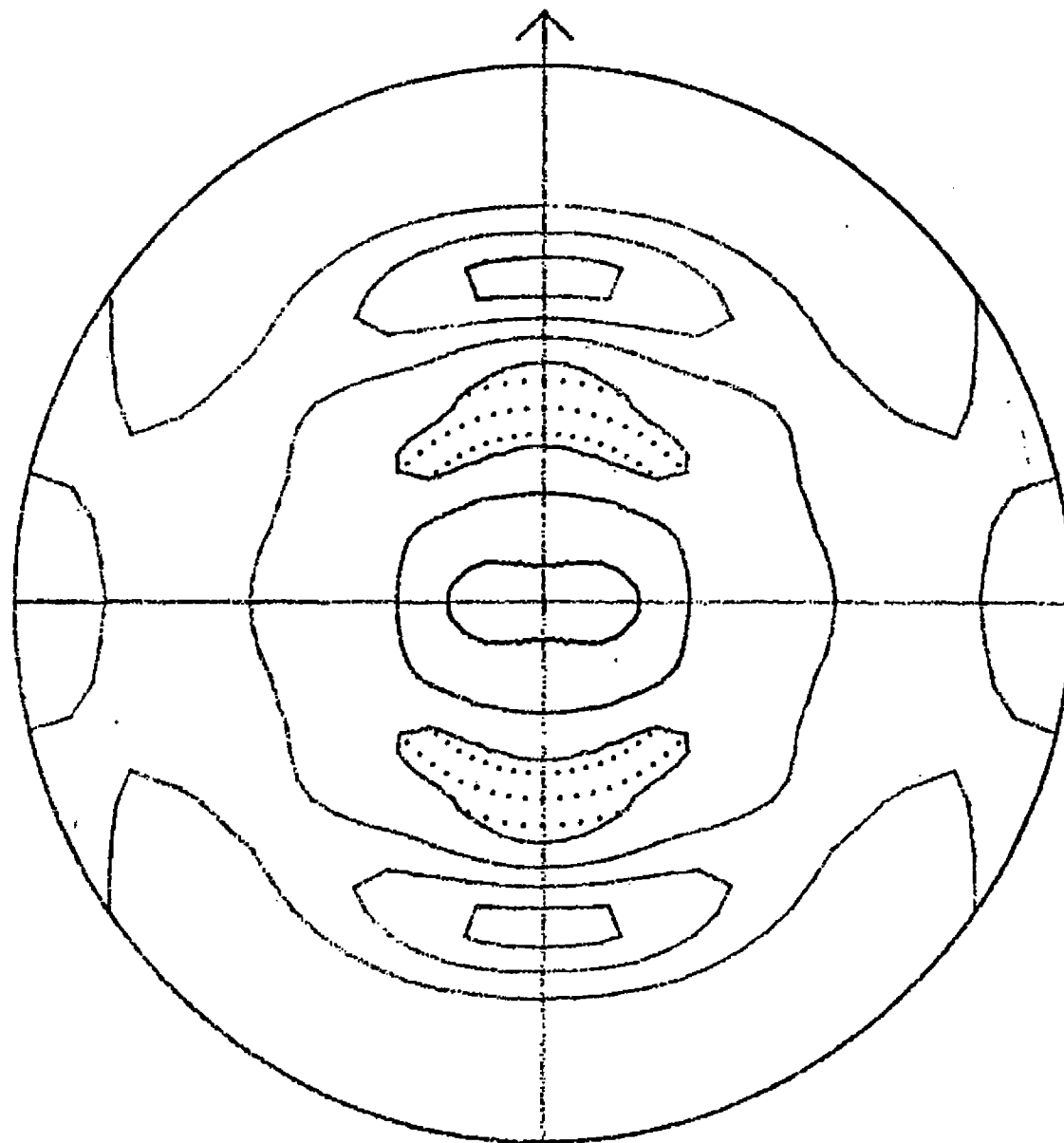
Contours at 1 2 3

0



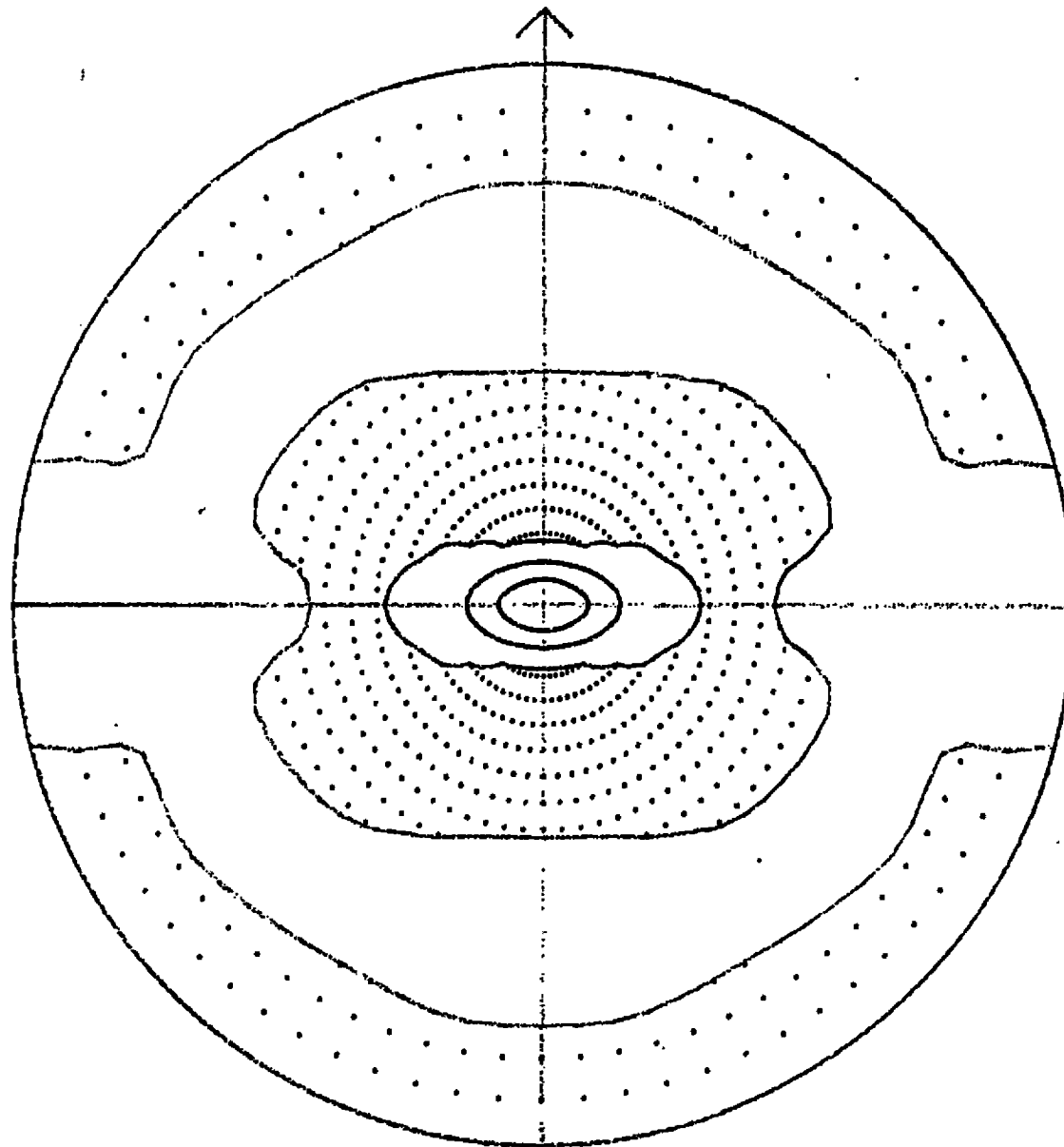
#1-CR3

Contours at 1 2 3 4



#1-CR4
recalc. pole figure 28-NOV-95
(211) Stereographic Projection
Contours at .80 1.00 1.20 1.40

28-NOV-95
. Expanded
D

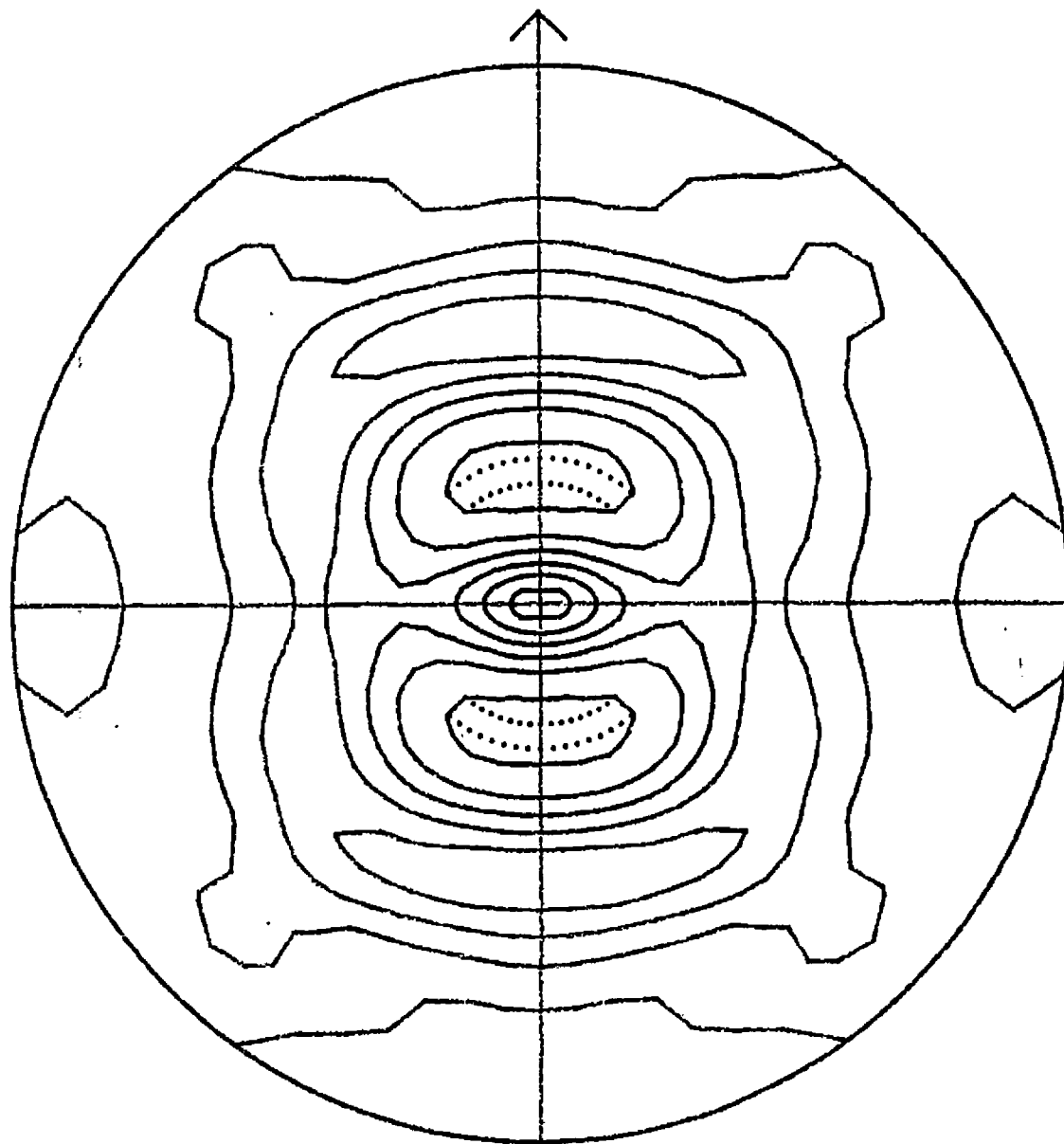


#1-CR4
recalc. pole figure 28-NOV-95
(111) Stereographic Projection

Contours at 1 2 3

28-NOV-95
. Expanded

0



#1-CR4

recalc. pole figure 28-NOV-95

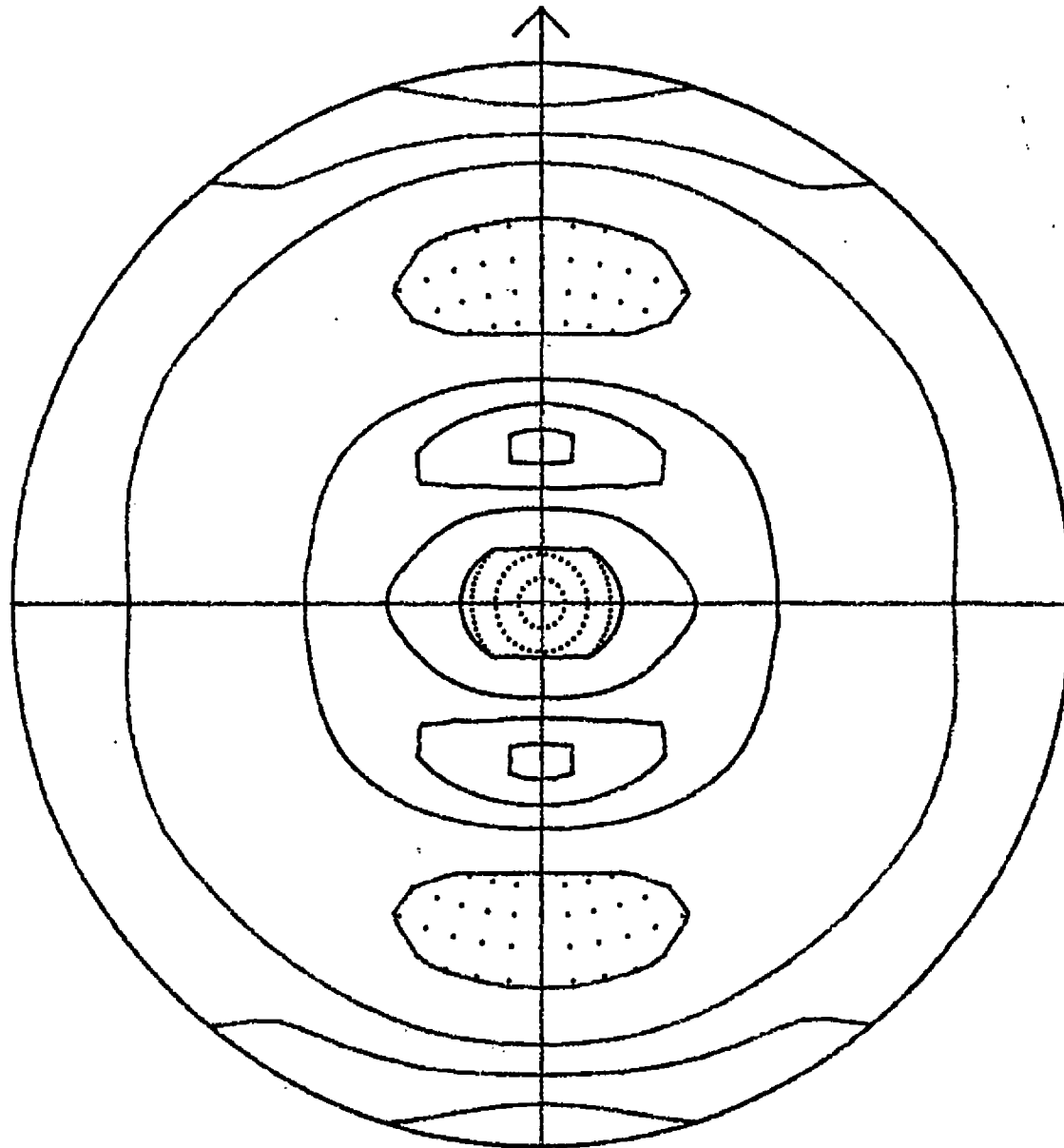
(200) Stereographic Projection

Contours at 50 75 1 00 1.25 1.50 1.75

28-NOV-95

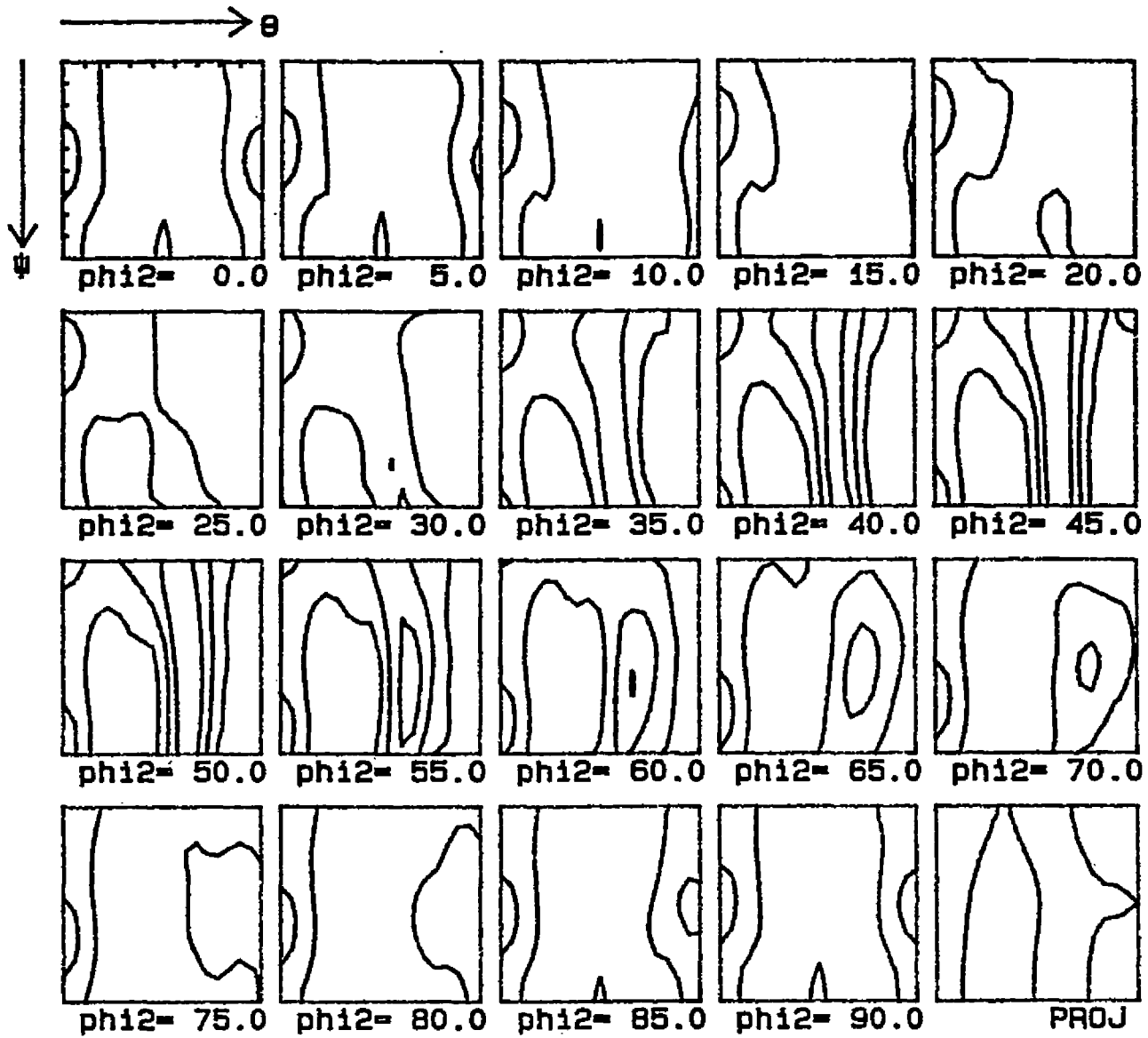
. Expanded

0



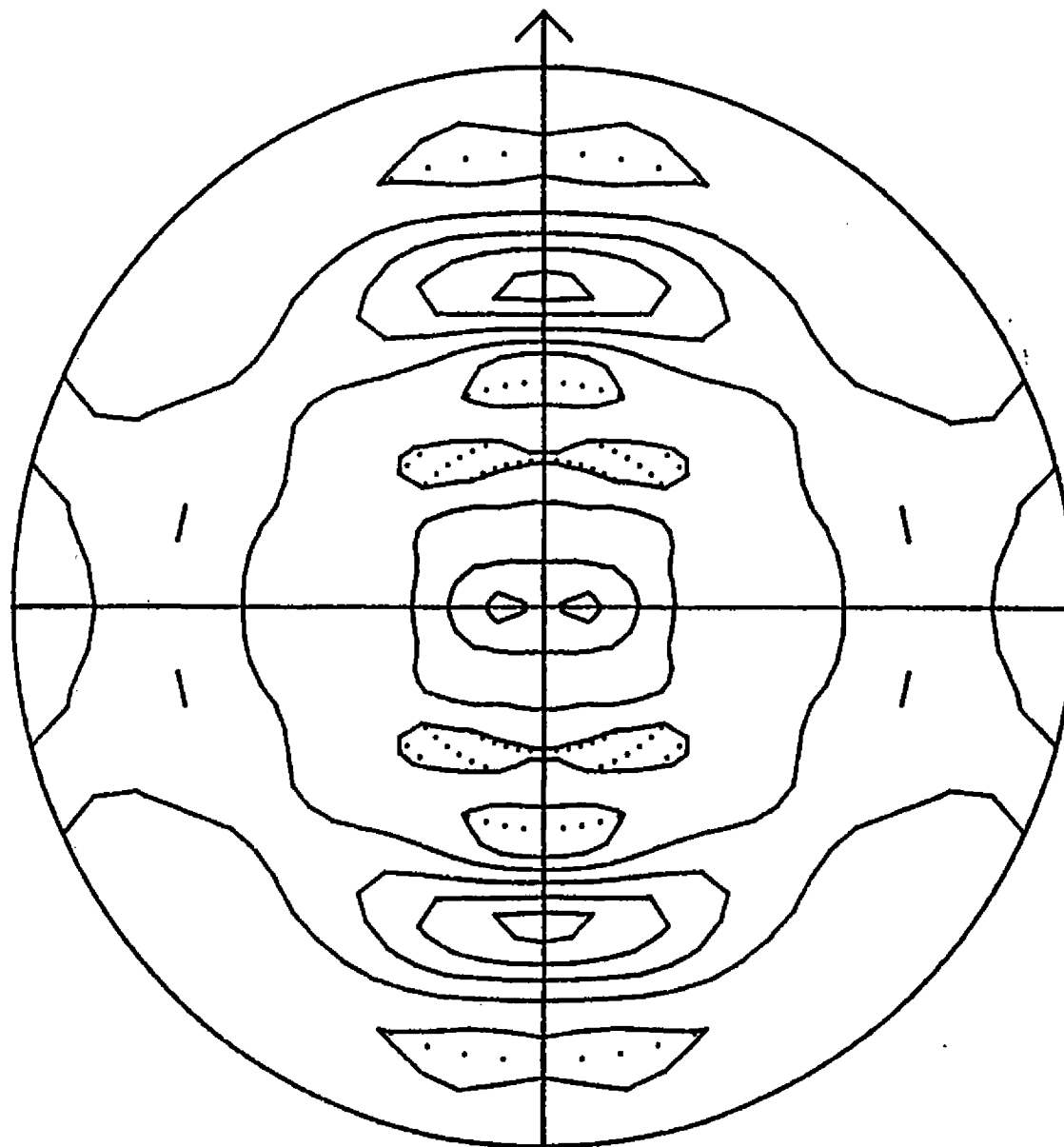
#1-CR4
recalc. pole figure 28-NOV-95
(110) Stereographic Projection
Contours at .50 1.00 1.50 2.00

28-NOV-95
. Expanded



#1-CR4

Contours at 1 2 3



#1-CR5

recalc. pole figure 24-NOV-95

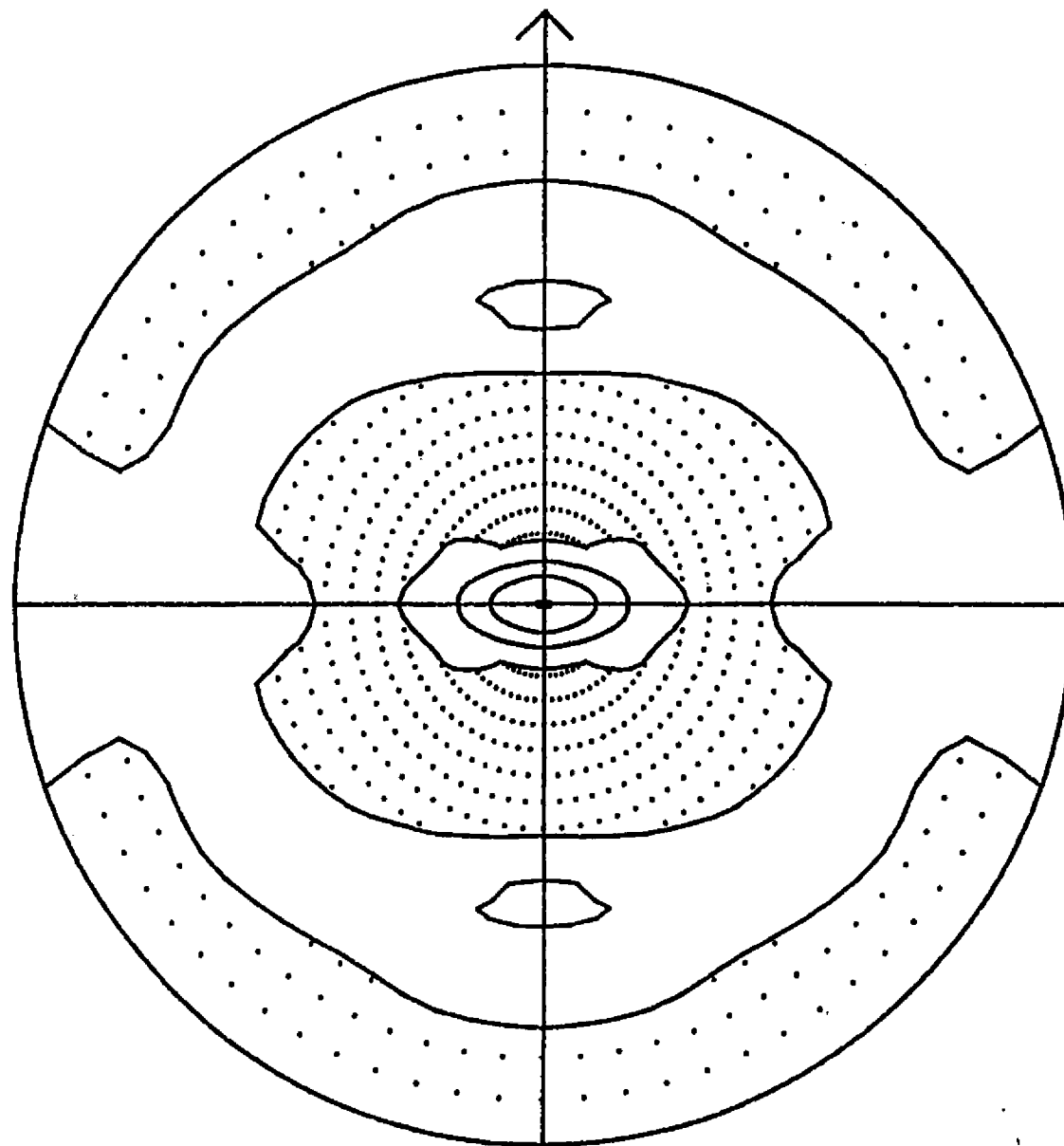
(211) Stereographic Projection

Contours at 80 1.00 1.20 1.40 1.60

24-NOV-95

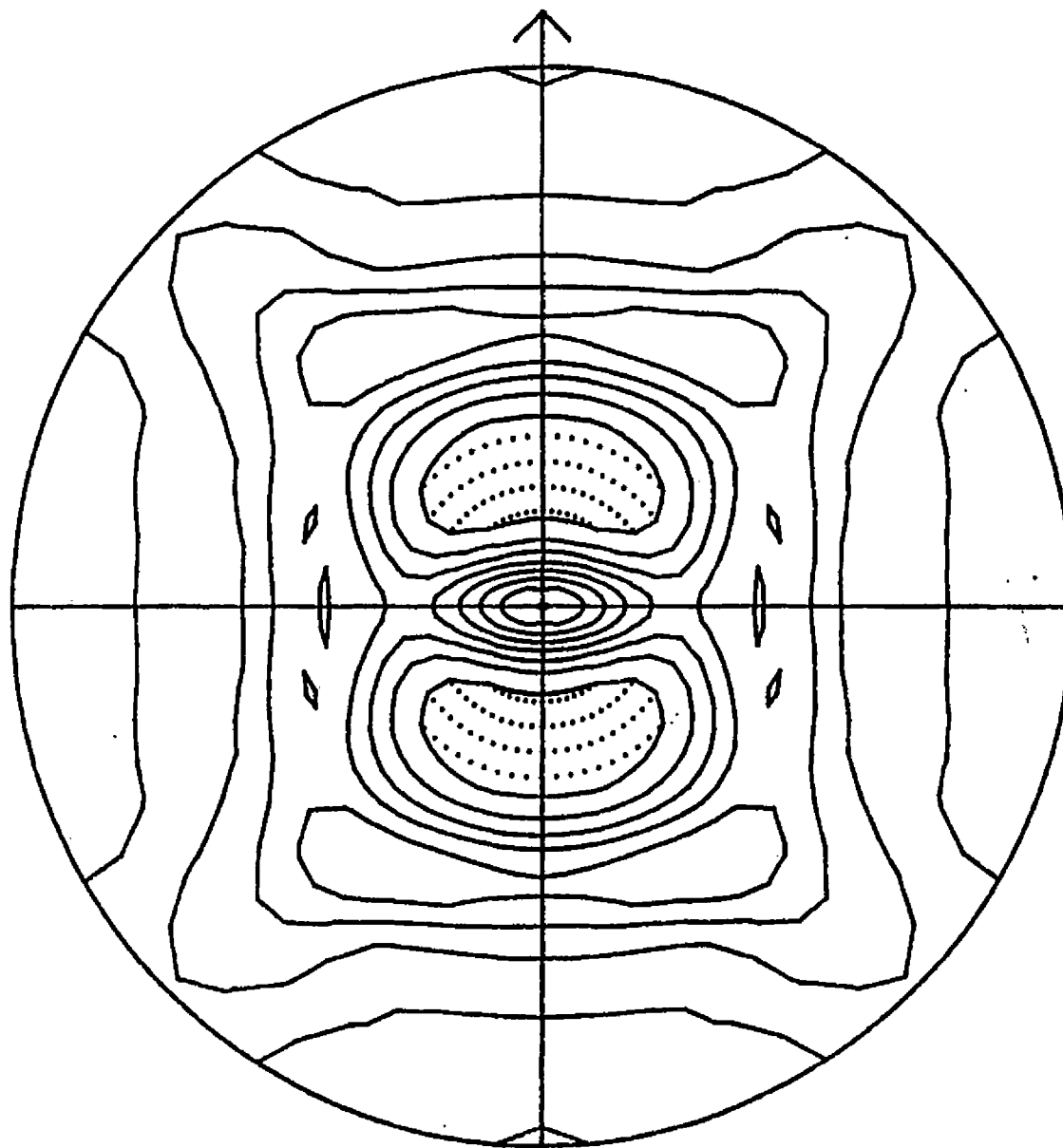
, Expanded

0



#1-CR5
recalc. pole figure 24-NOV-95
(111) Stereographic Projection
Contours at 1 2 3 4

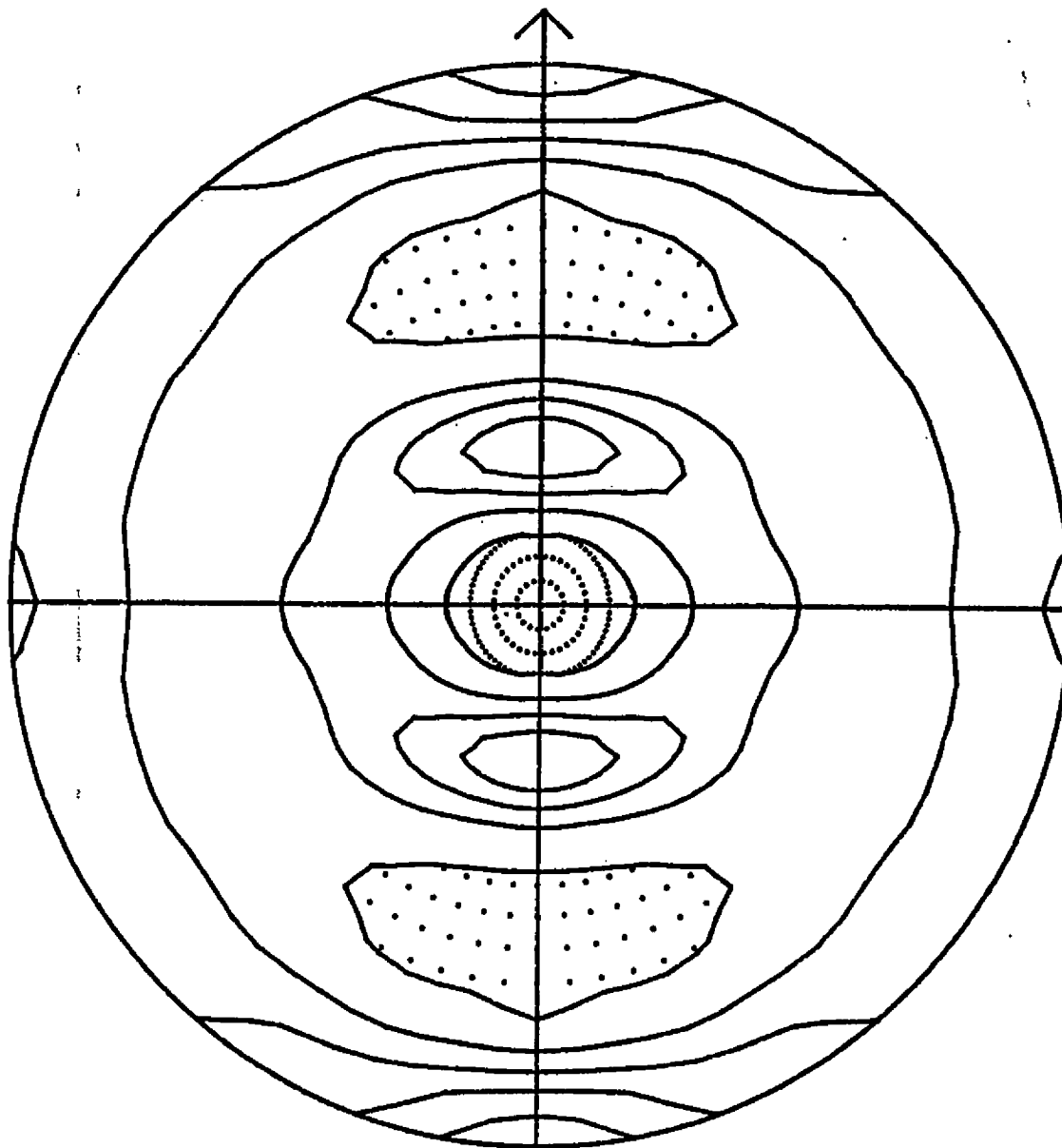
24-NOV-95
. Expanded
ii



#1-CR5
recalc. pole figure24-NOV-95
(200) Stereographic Projection

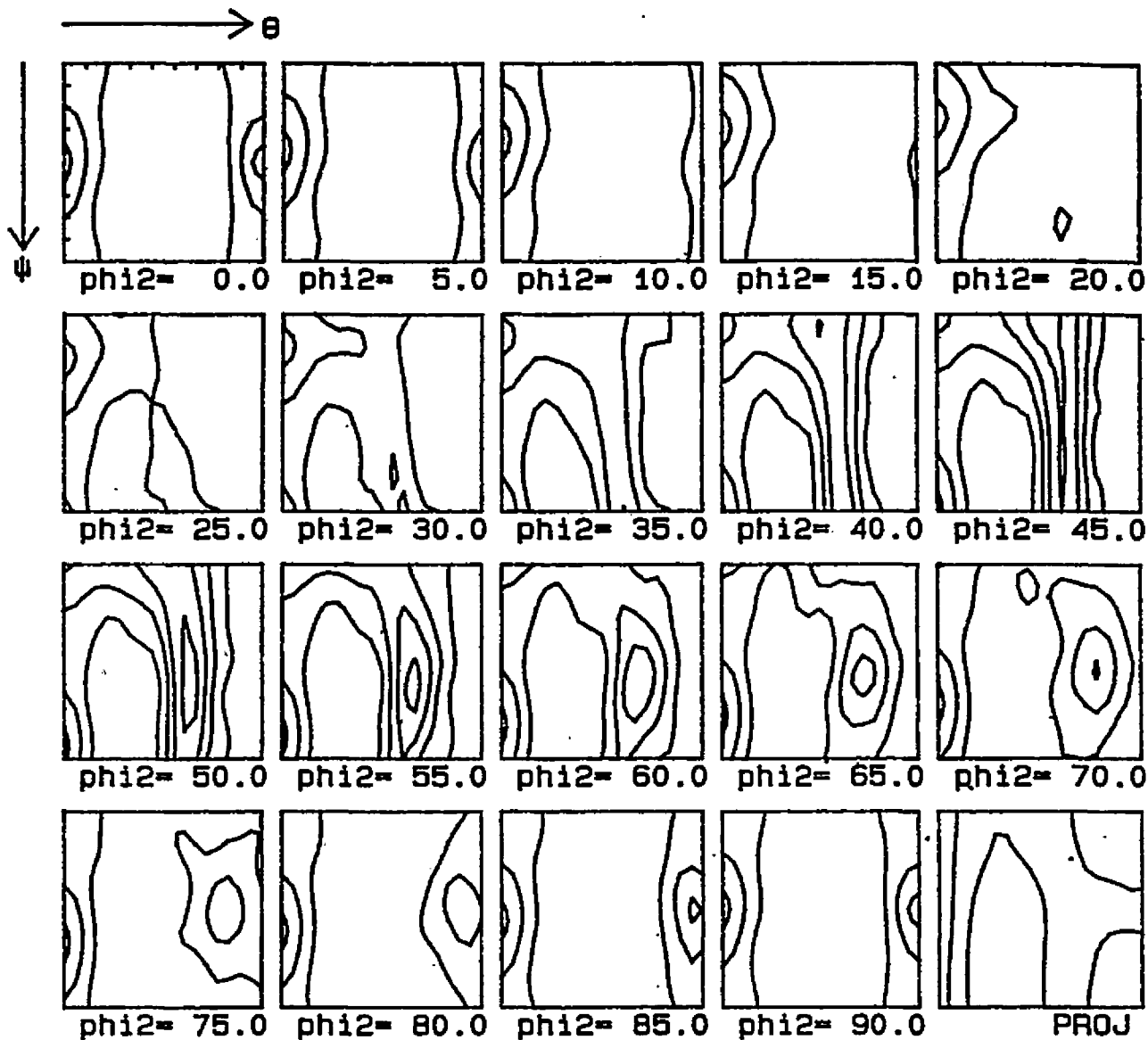
24-NOV-95
. Expanded

Contours at .50 .75 1.00 1.25 1.50 1.75 2.00 2.25



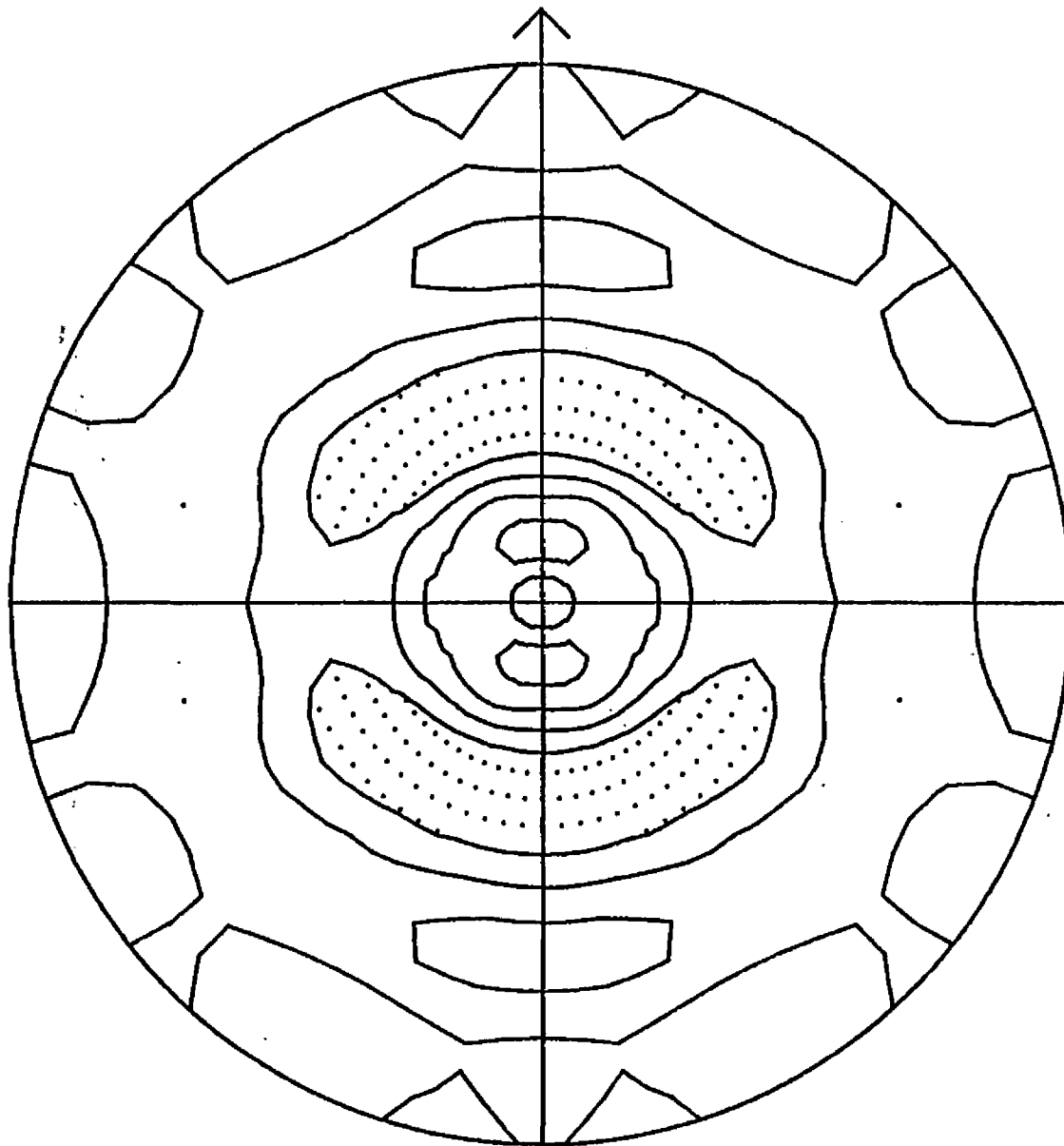
#1-CR5
recalc. pole figure 24-NOV-95
(110) Stereographic Projection
Contours at .50 1.00 1.50 2.00 2.50

24-NOV-95
. Expanded



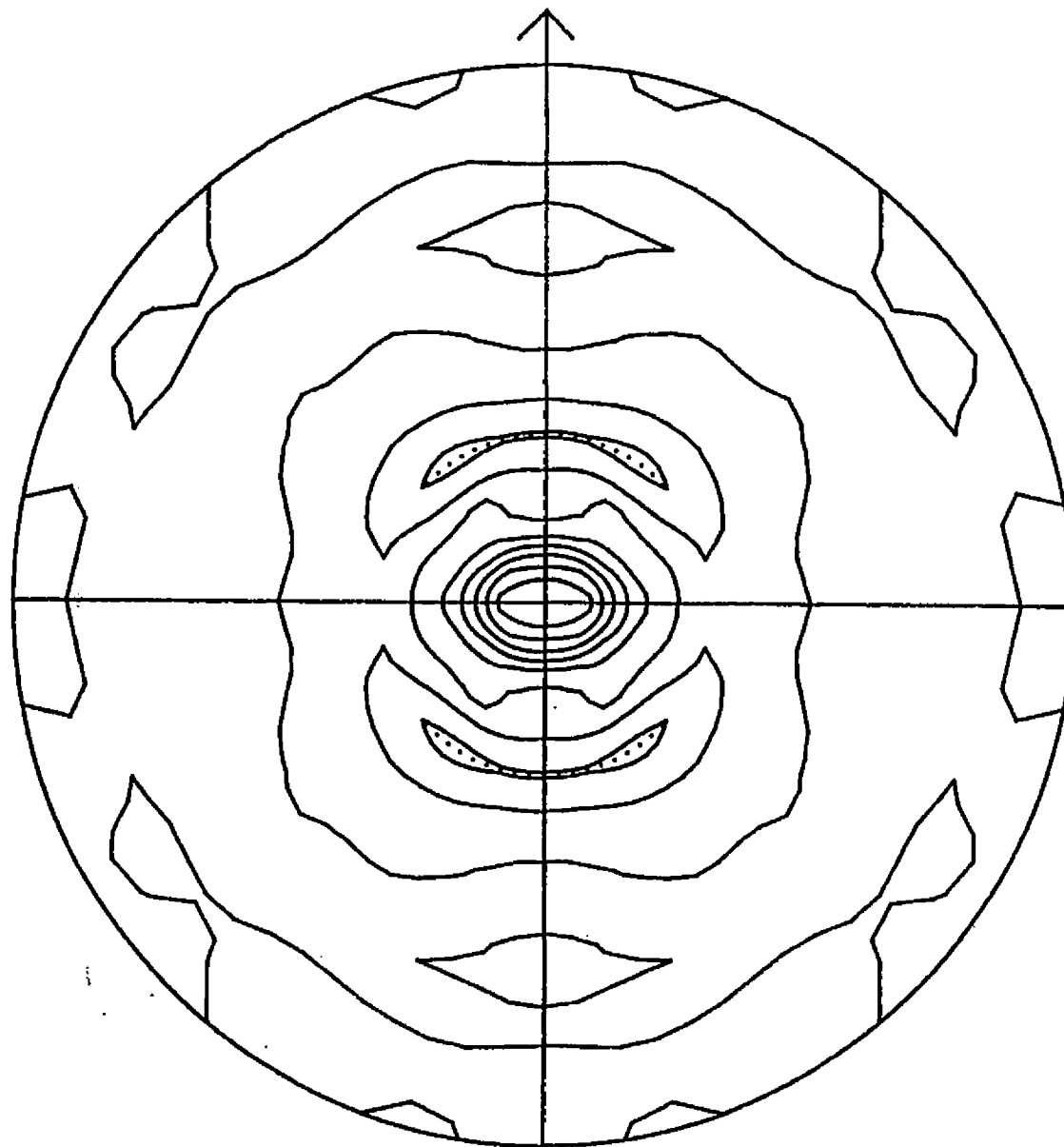
#1-CR5

Contours at 1 2 3 4



#2 HOT-BAND (#6)
recalc. pole figure 27-AUG-96
(211) Stereographic Projection
Contours at 00 1 00 1 10 1 20

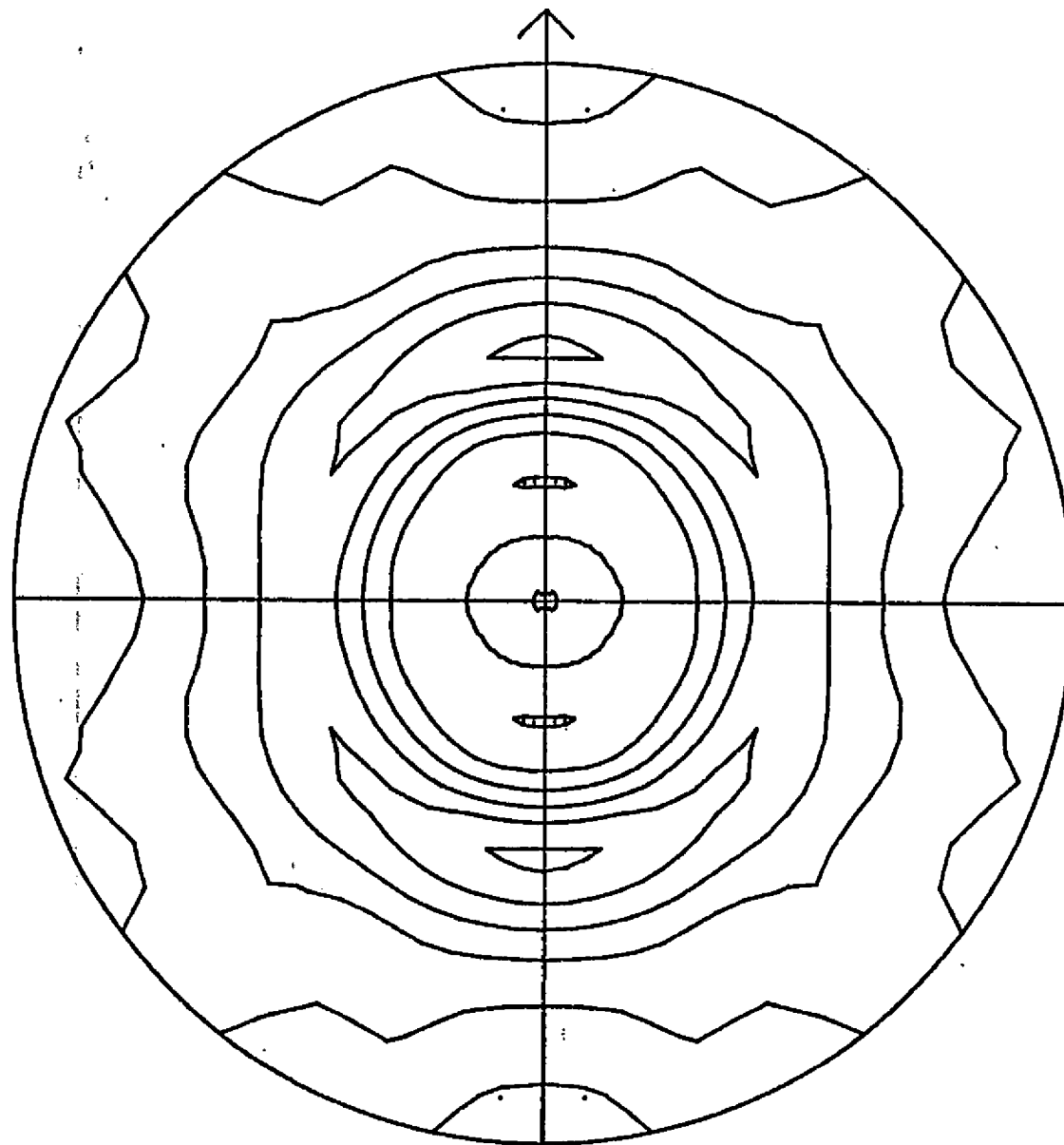
27-AUG-96
, Expanded



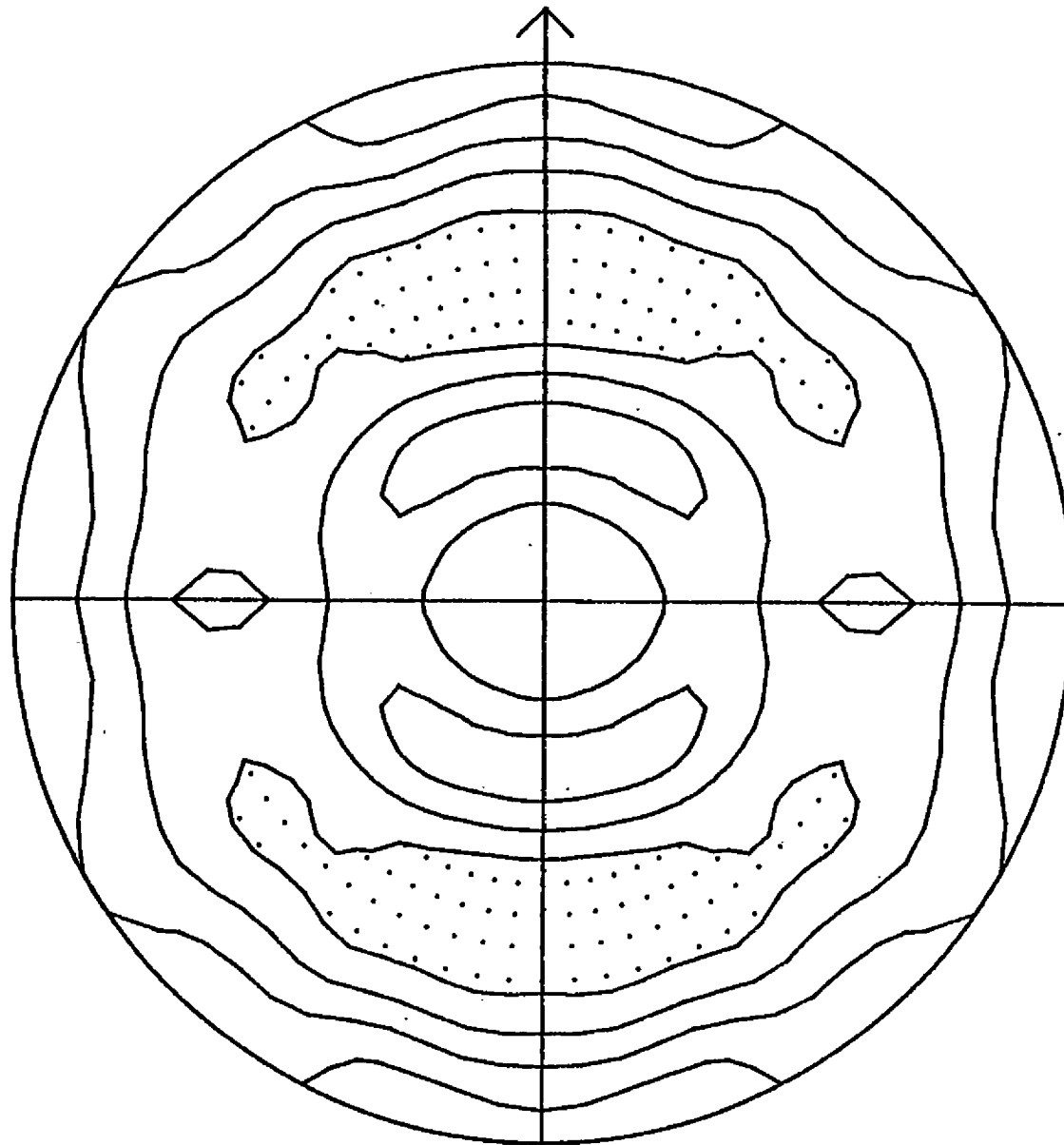
#2 HOT-BAND (#6)
recalc. pole figure 27-AUG-96
(111) Stereographic Projection

27-AUG-96
, Expanded

Contours at .50 .75 1.00 1.25 1.50 1.75 2.00 2.25

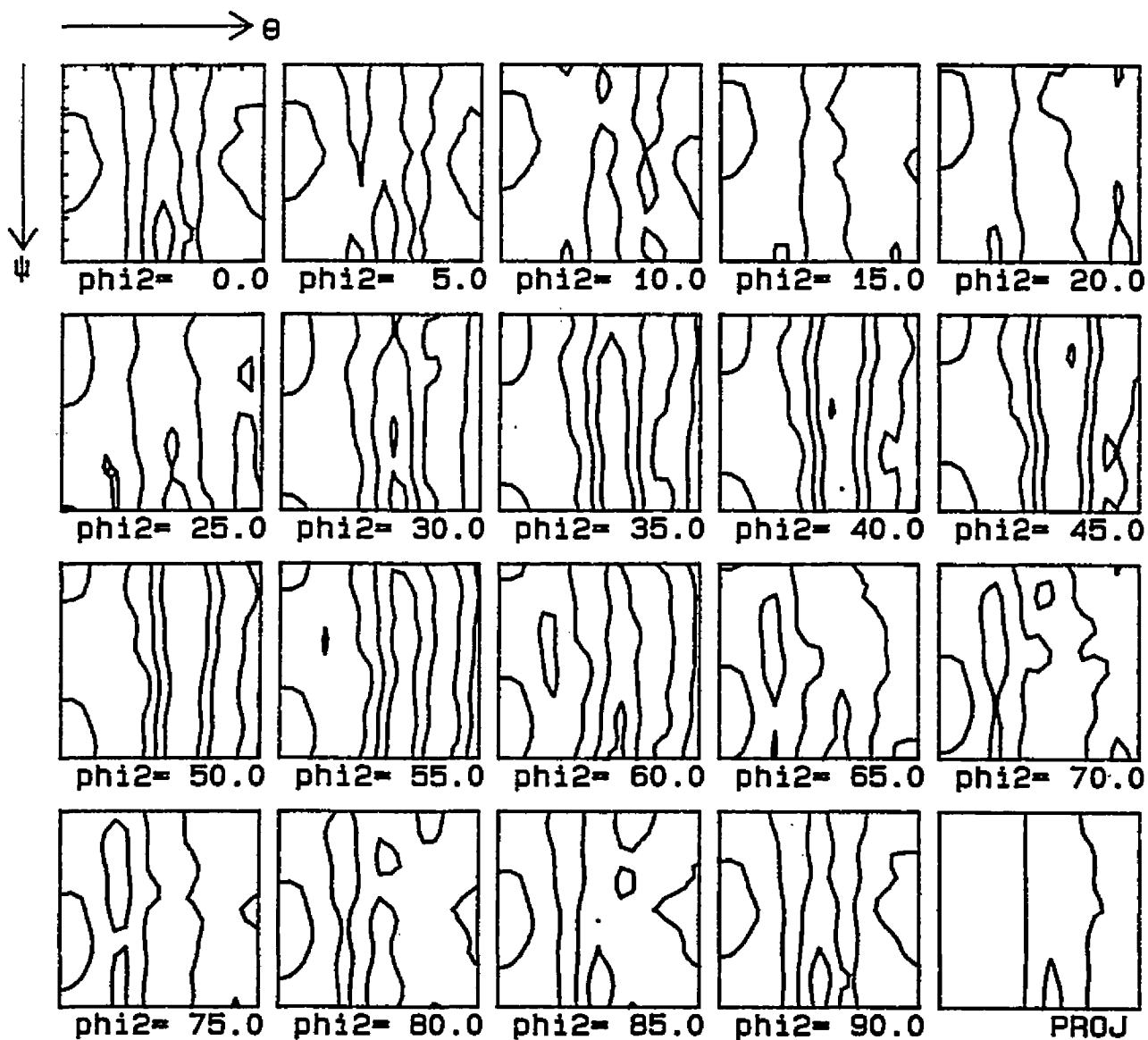


#2 HOT-BAND (#6) 27-AUG-96
recalc. pole figure 27-AUG-96 . Expanded
(200) Stereographic Projection
Contours at .60 .80 1.00 1.20 1.40 1.60



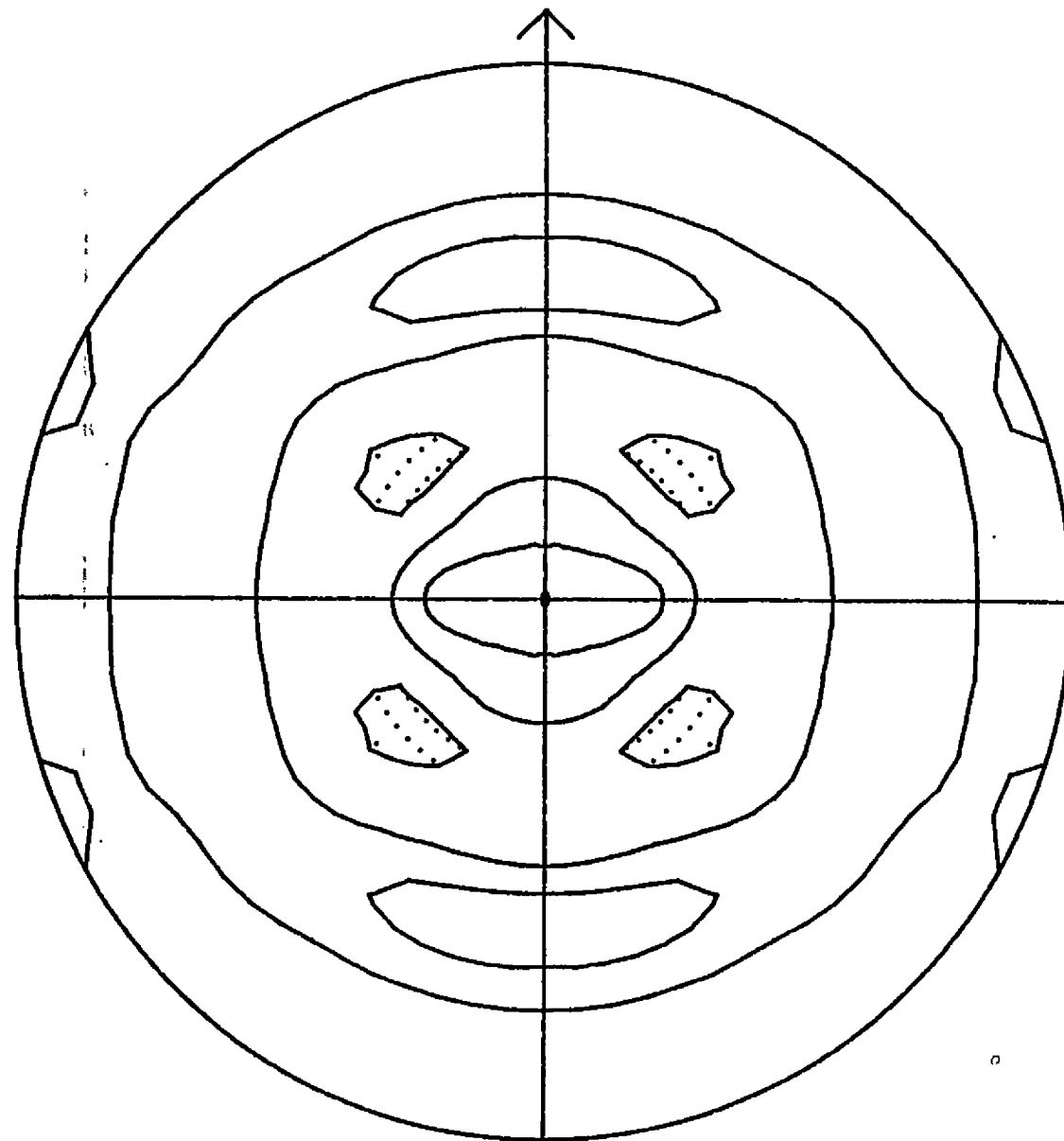
#2 HOT-BAND (#6)
recalc. pole figure 27-AUG-96
(110) Stereographic Projection
Contours at R0 1.00 1.20 1.40

27-AUG-96
, Expanded



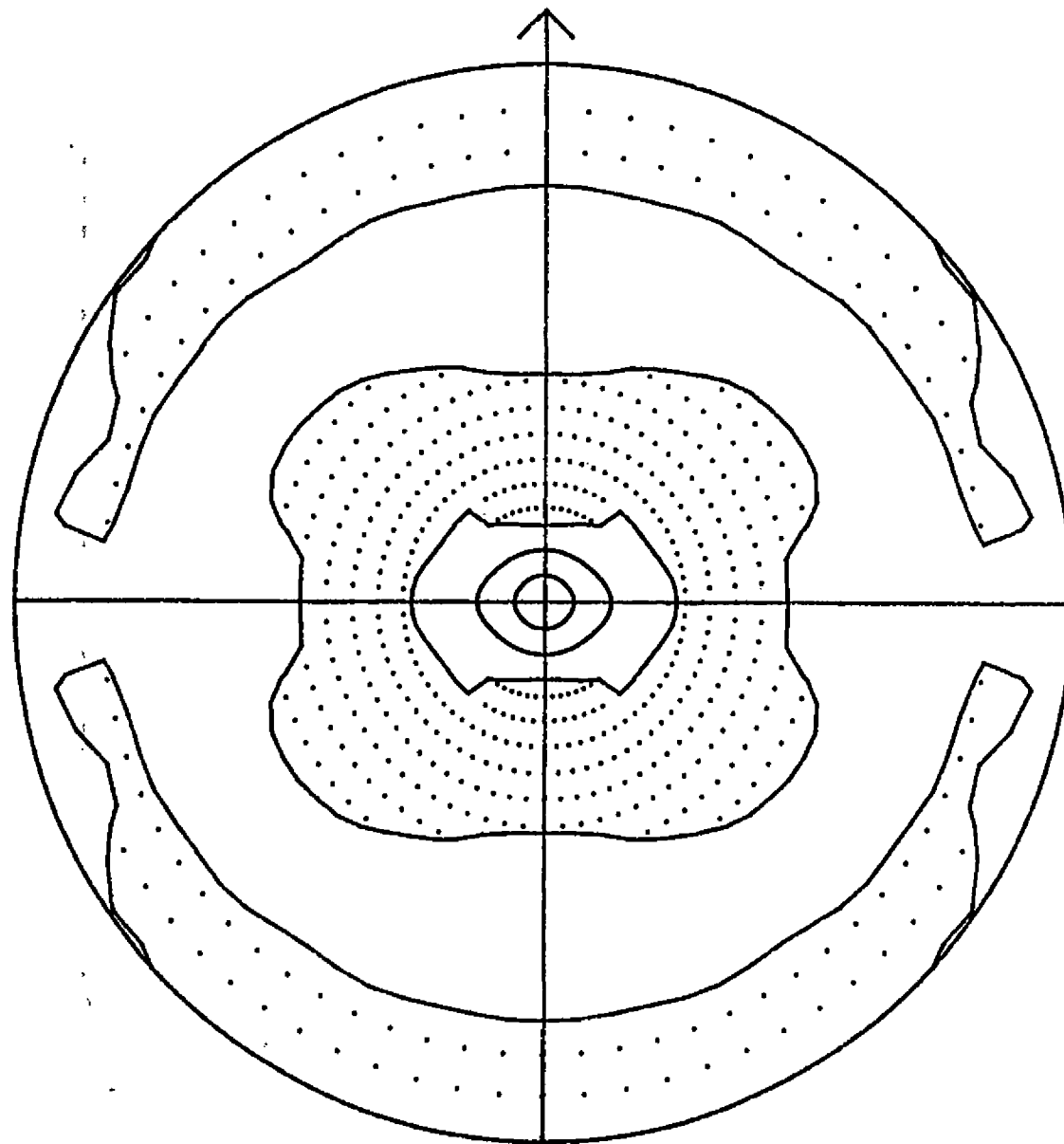
#2 HOT-BAND (#6)

Contours at .50 1.00 1.50 2.00 2.50



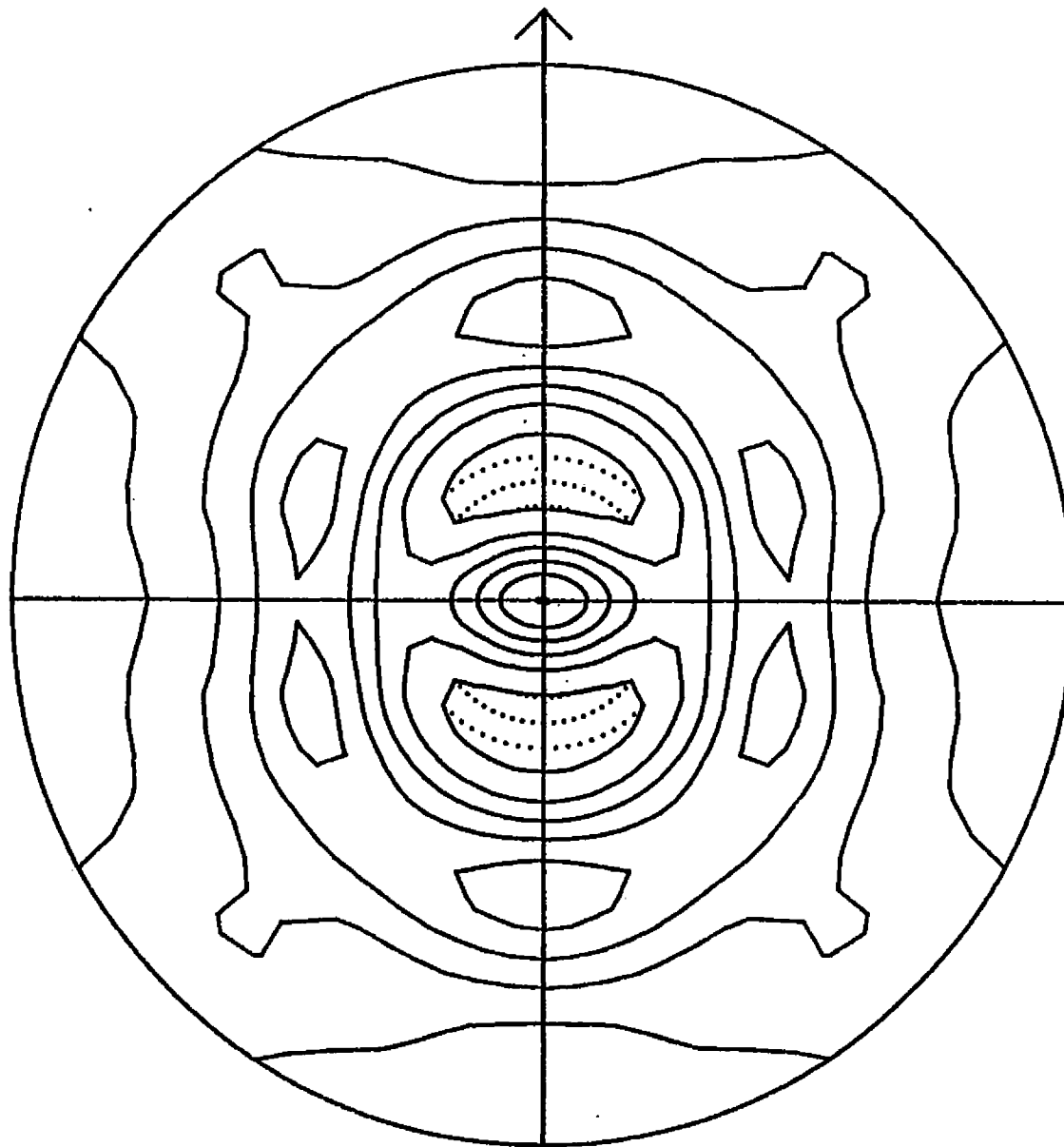
#2-CR1
recalc. pole figure 27-AUG-96
(211) Stereographic Projection
Contours at .80 1.00 1.20

27-AUG-96
, Expanded



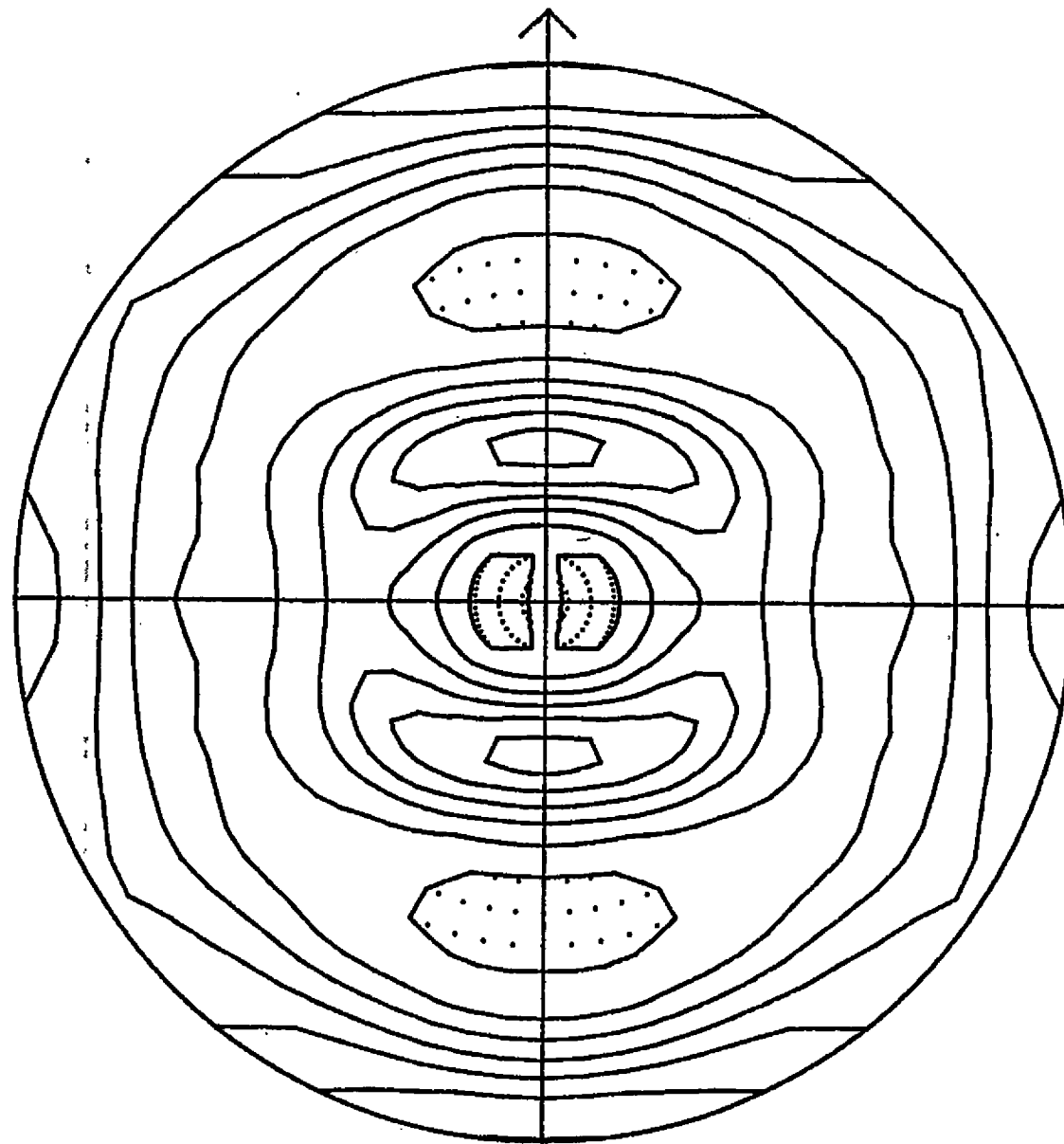
#2-CR1
recalc. pole figure 27-AUG-96
(111) Stereographic Projection
Contours at 1 2 3

27-AUG-96
, Expanded



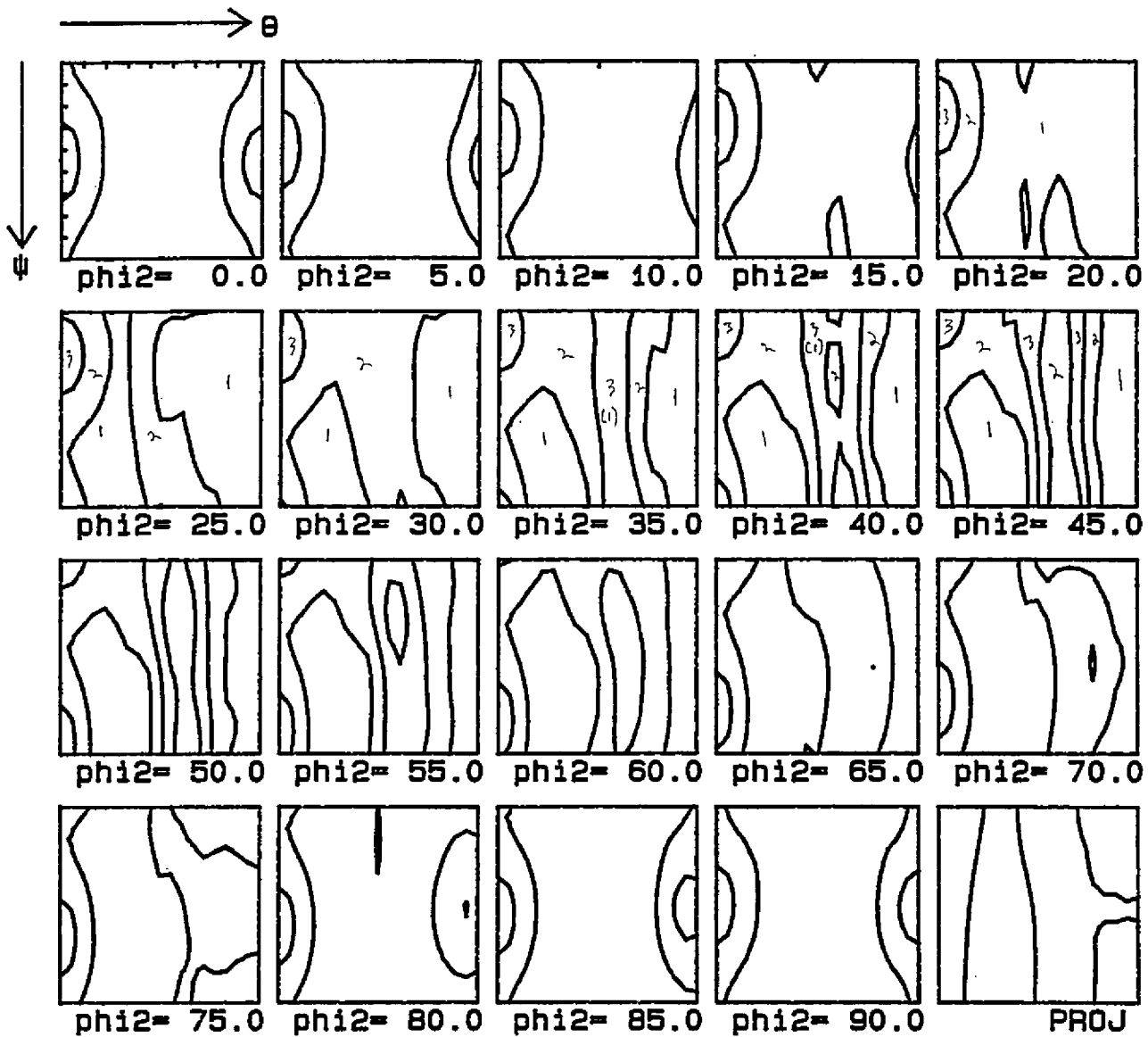
#2-CR1
recalc. pole figure 27-AUG-96
(200) Stereographic Projection
Contours at .50 .75 1.00 1.25 1.50 1.75

27-AUG-96
, Expanded



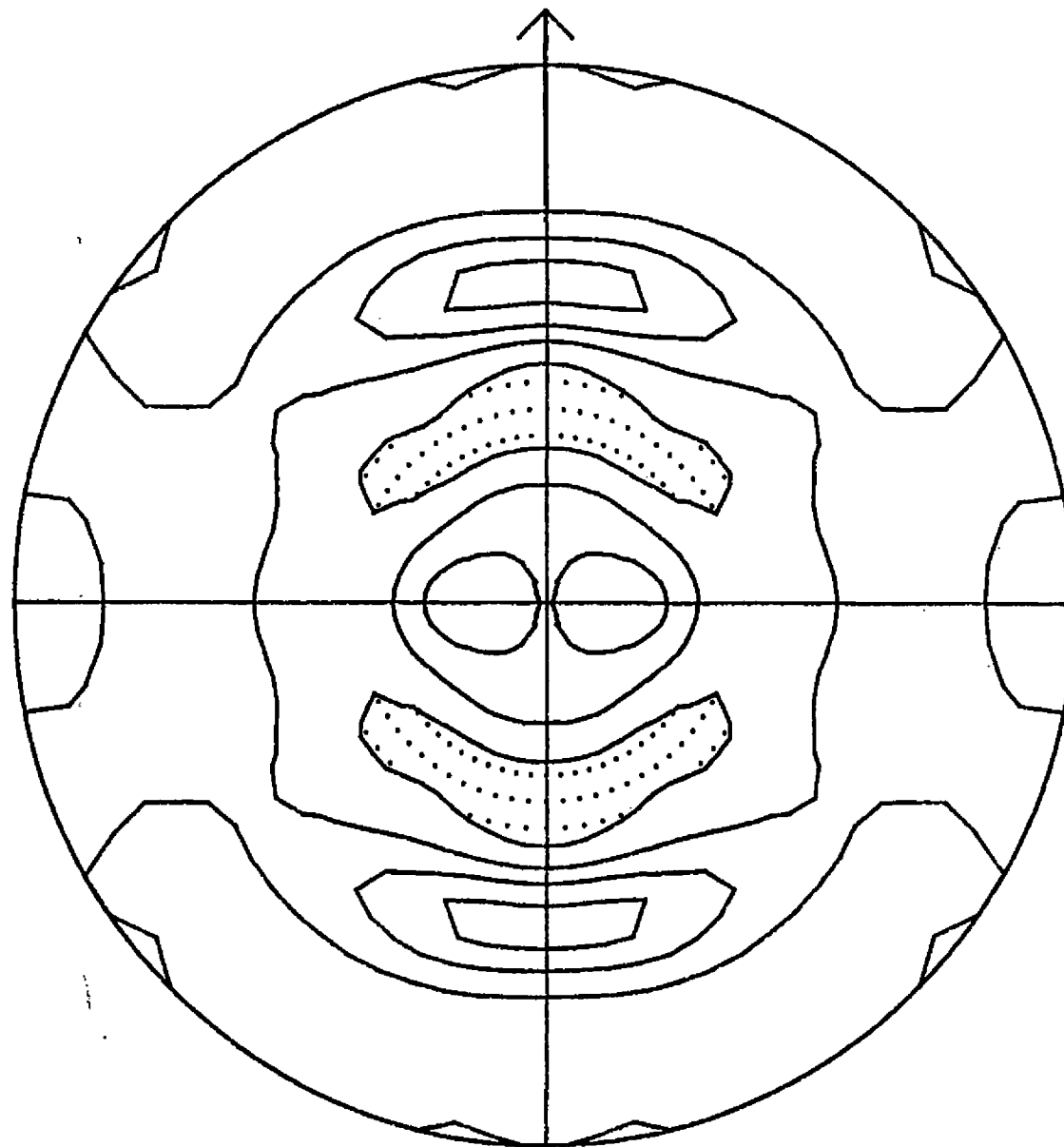
#2-CR1
recalc. pole figure
(110) Stereographic Projection
Contours at .50 .75 1.00 1.25 1.50 1.75 2.00

27-AUG-96
, Expanded



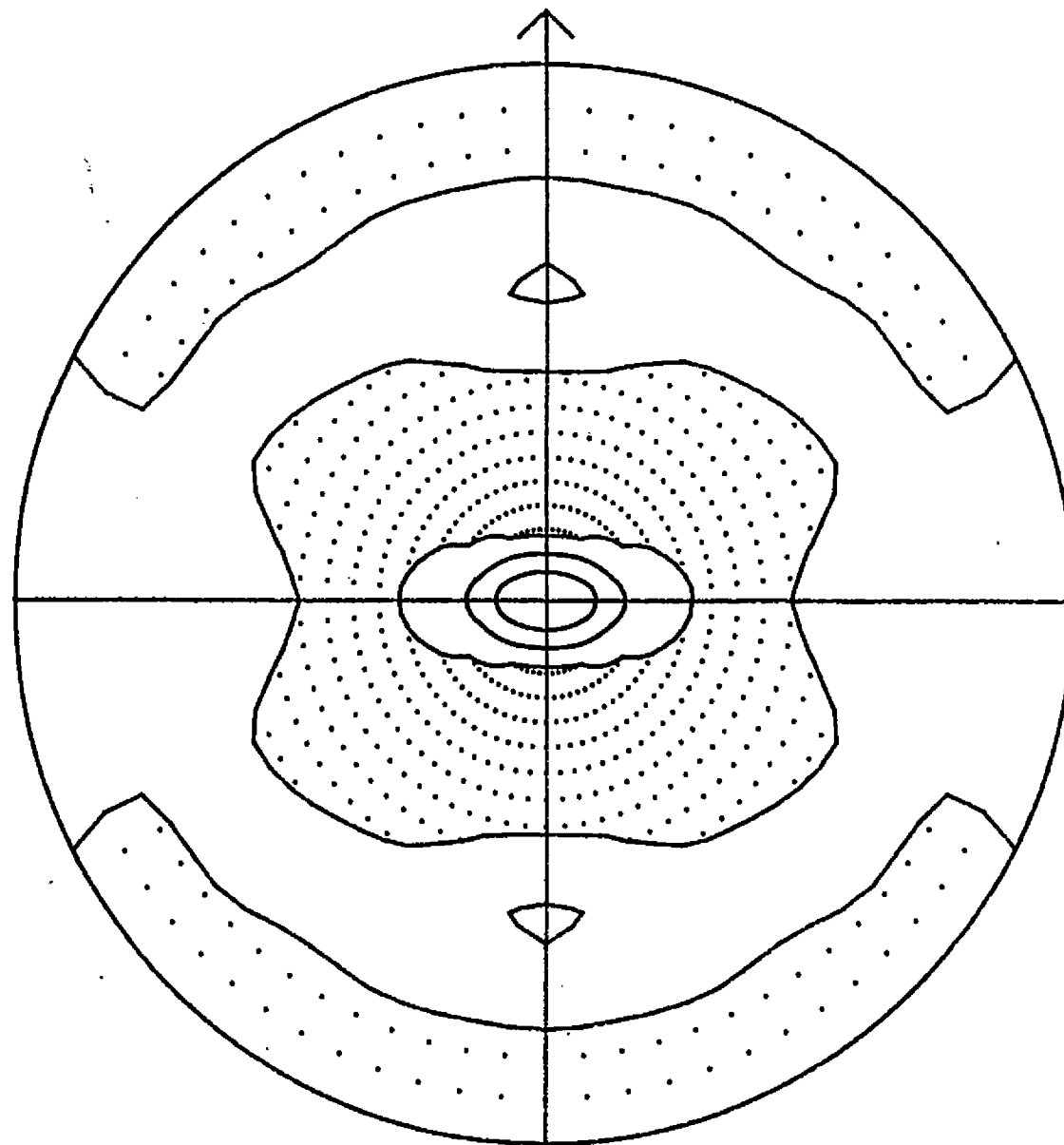
#2-CR1

Contours at 1 2 3



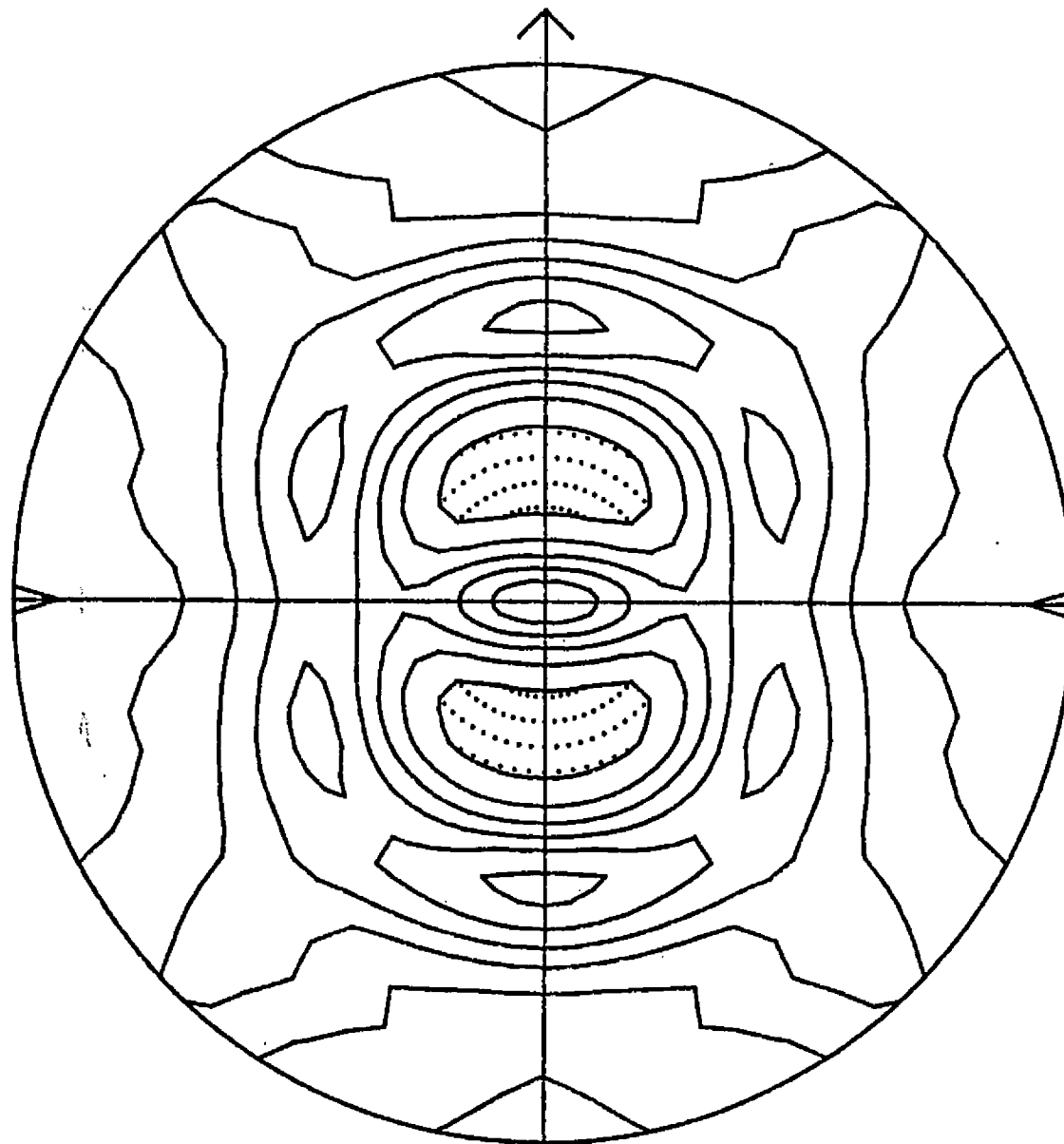
#2-CR2
recalc. pole figure 27-AUG-96
(211) Stereographic Projection
Contours at .80 1.00 1.20 1.40

27-AUG-96
. Expanded



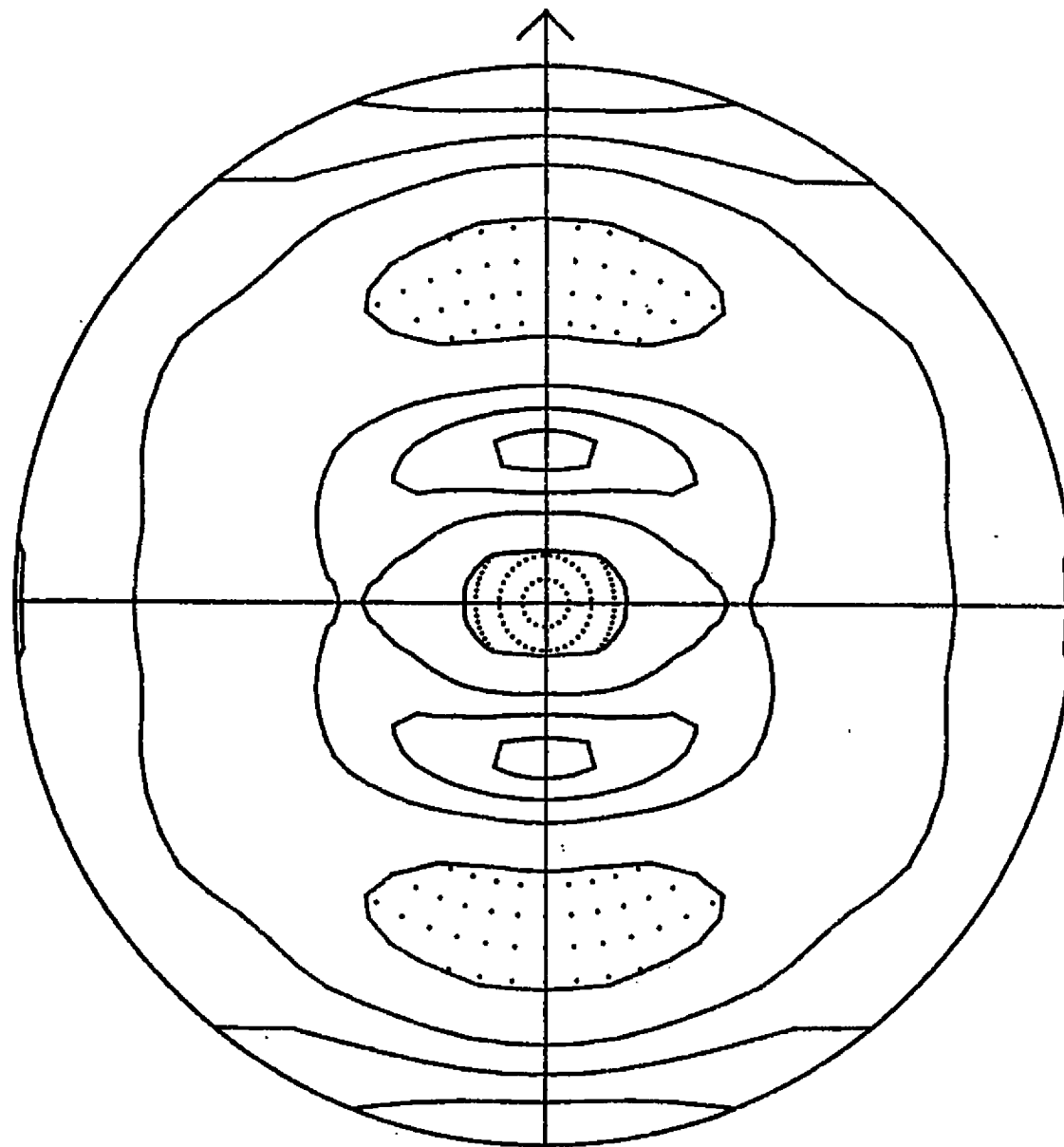
#2-CR2
recalc. pole figure 27-AUG-96
(111) Stereographic Projection
Contours at 1 2 3

27-AUG-96
. Expanded



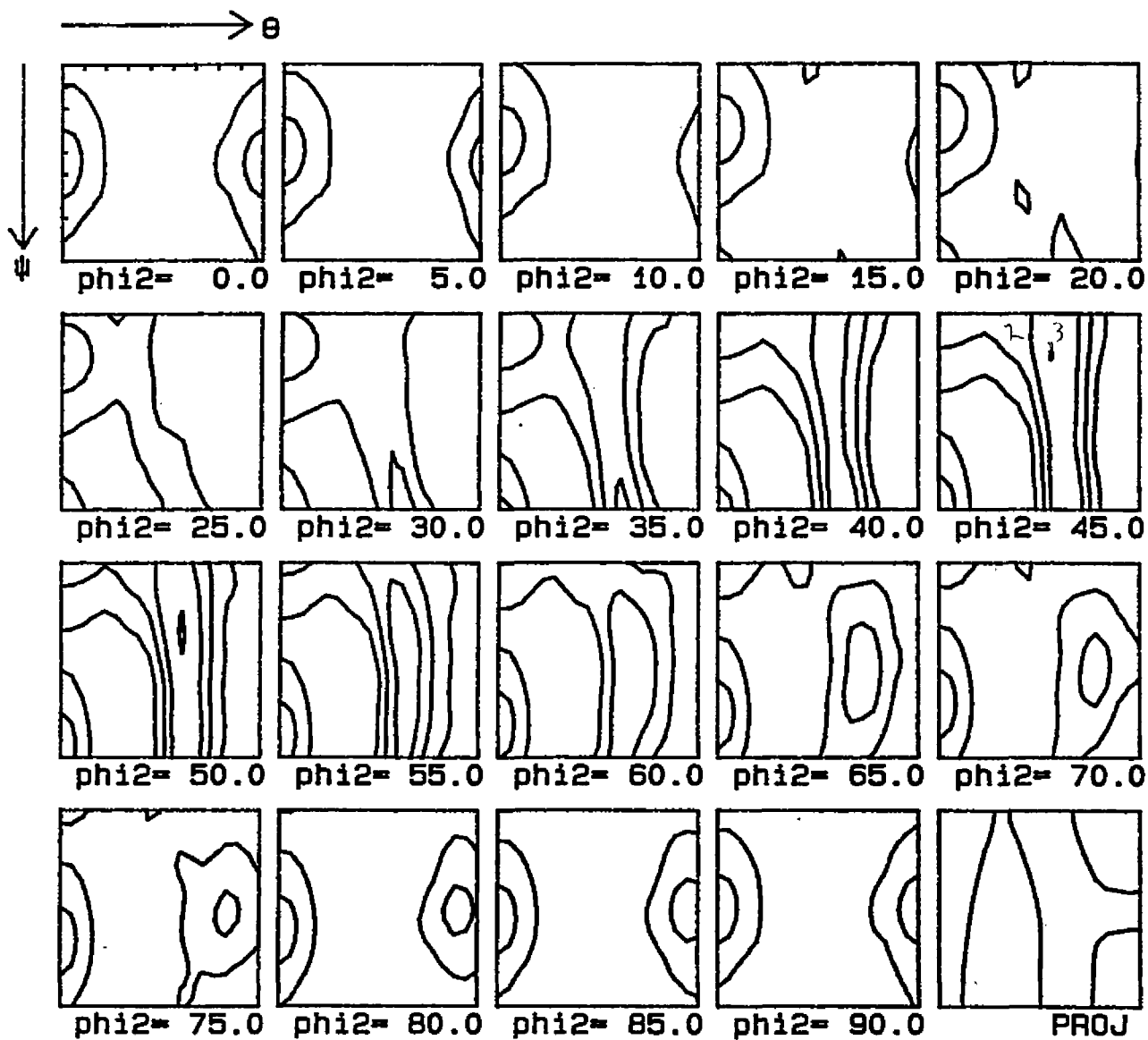
#2-CR2
recalc. pole figure
(200) Stereographic Projection
Contours at .50 .75 1.00 1.25 1.50 1.75

27-AUG-96
. Expanded



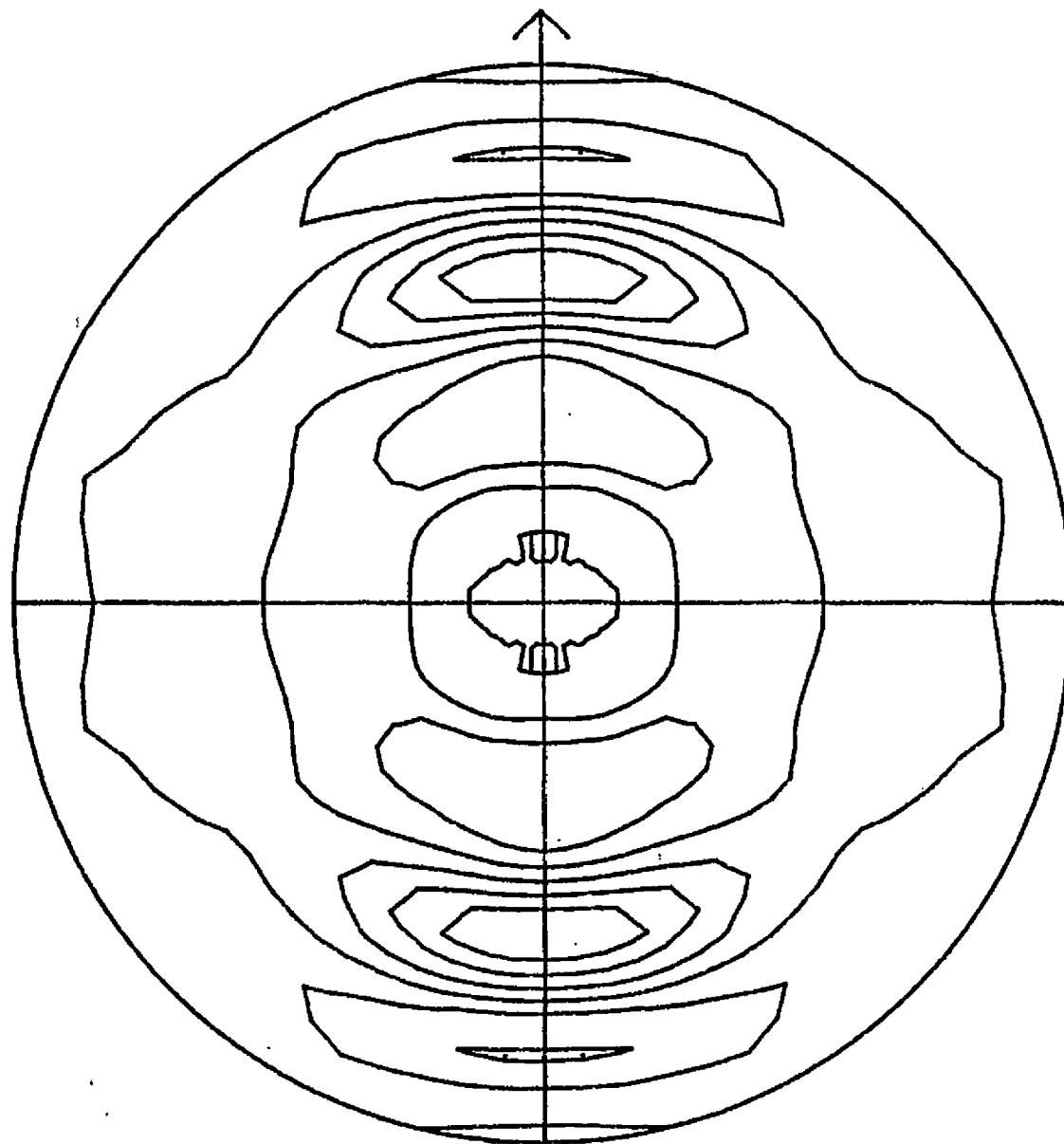
#2-CR2
recalc. pole figure 27-AUG-96
(110) Stereographic Projection
Contours at 50 1 00 1 50 2 00

27-AUG-96
, Expanded



#2-CR2

Contours at 1 2 3 4



#2-CR3

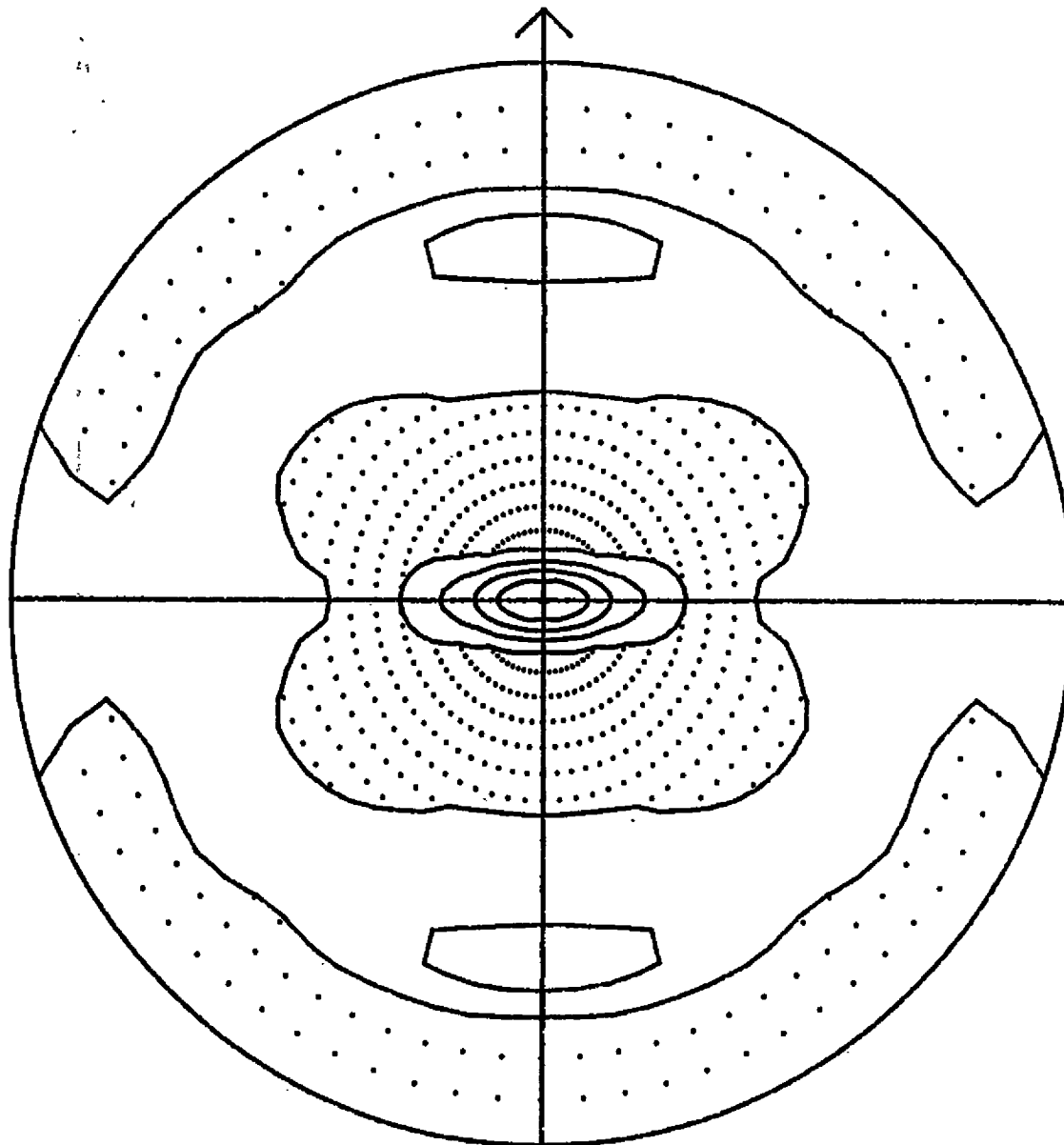
27-AUG-96

recalc. pole figure 27-AUG-96

. Expanded

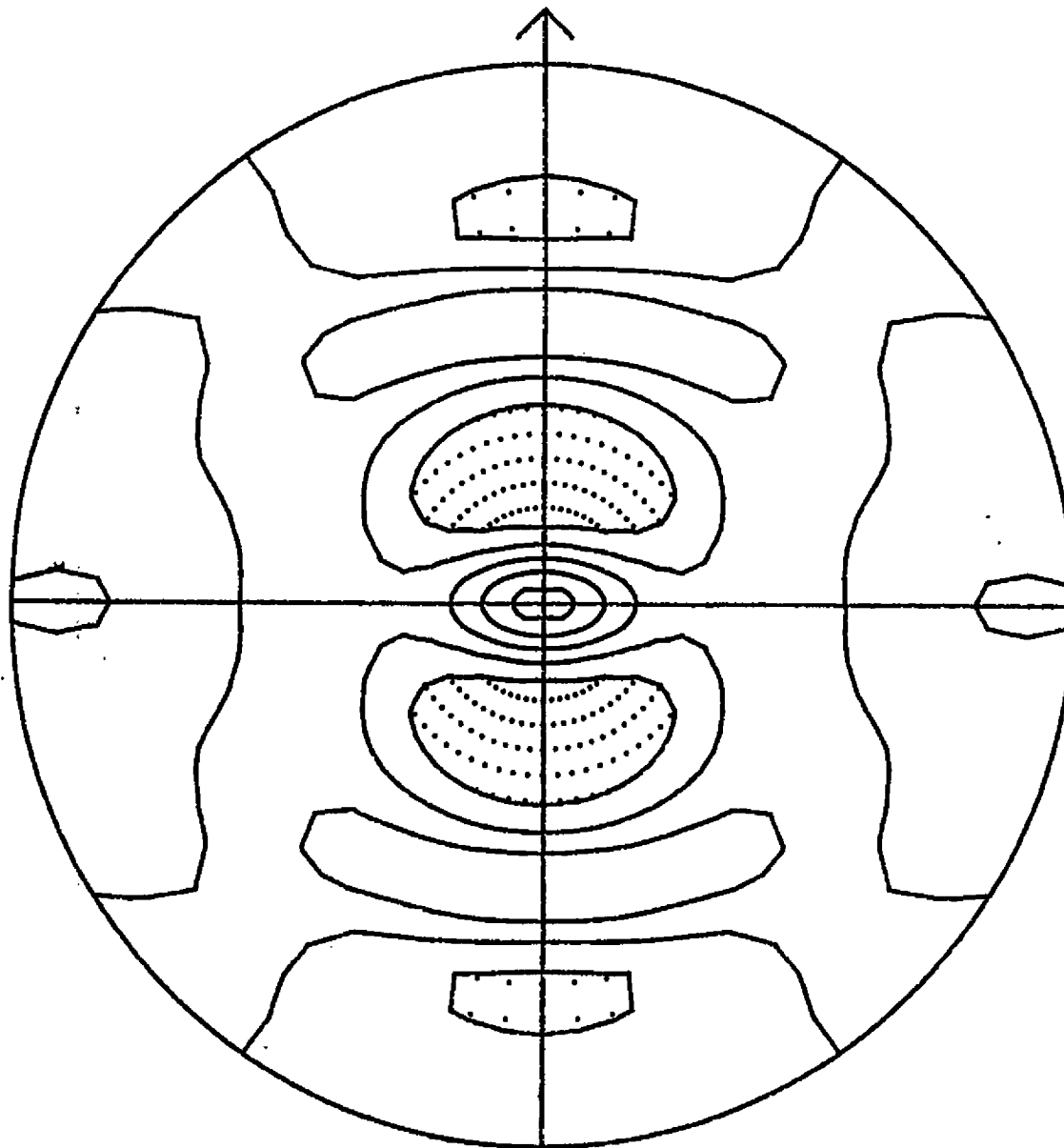
(211) Stereographic Projection

Contours at .60 .80 1.00 1.20 1.40 1.60



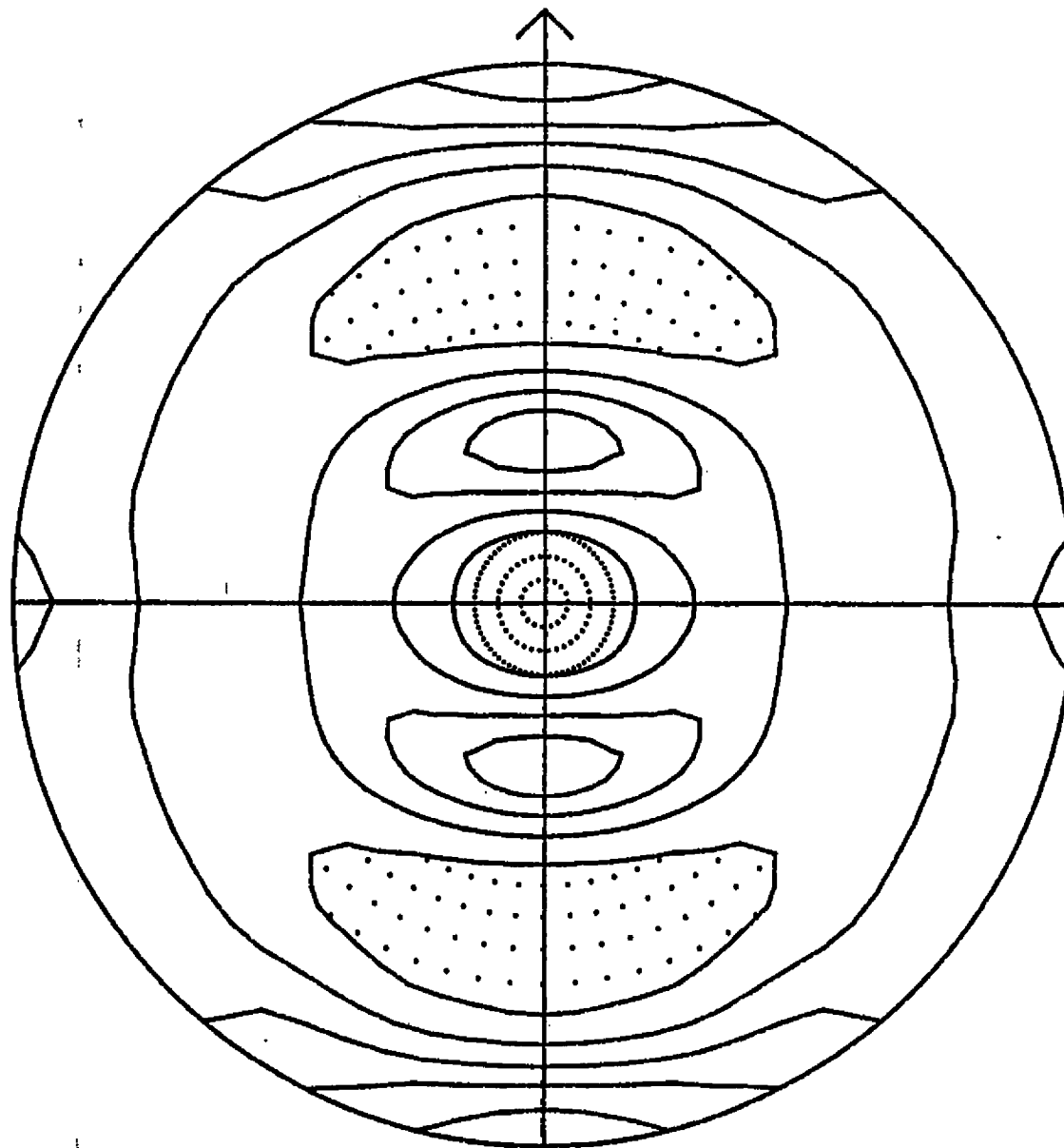
#2-CR3
recalc. pole figure 27-AUG-96
(111) Stereographic Projection
Contours at 1 2 3 4 5

27-AUG-96
. Expanded



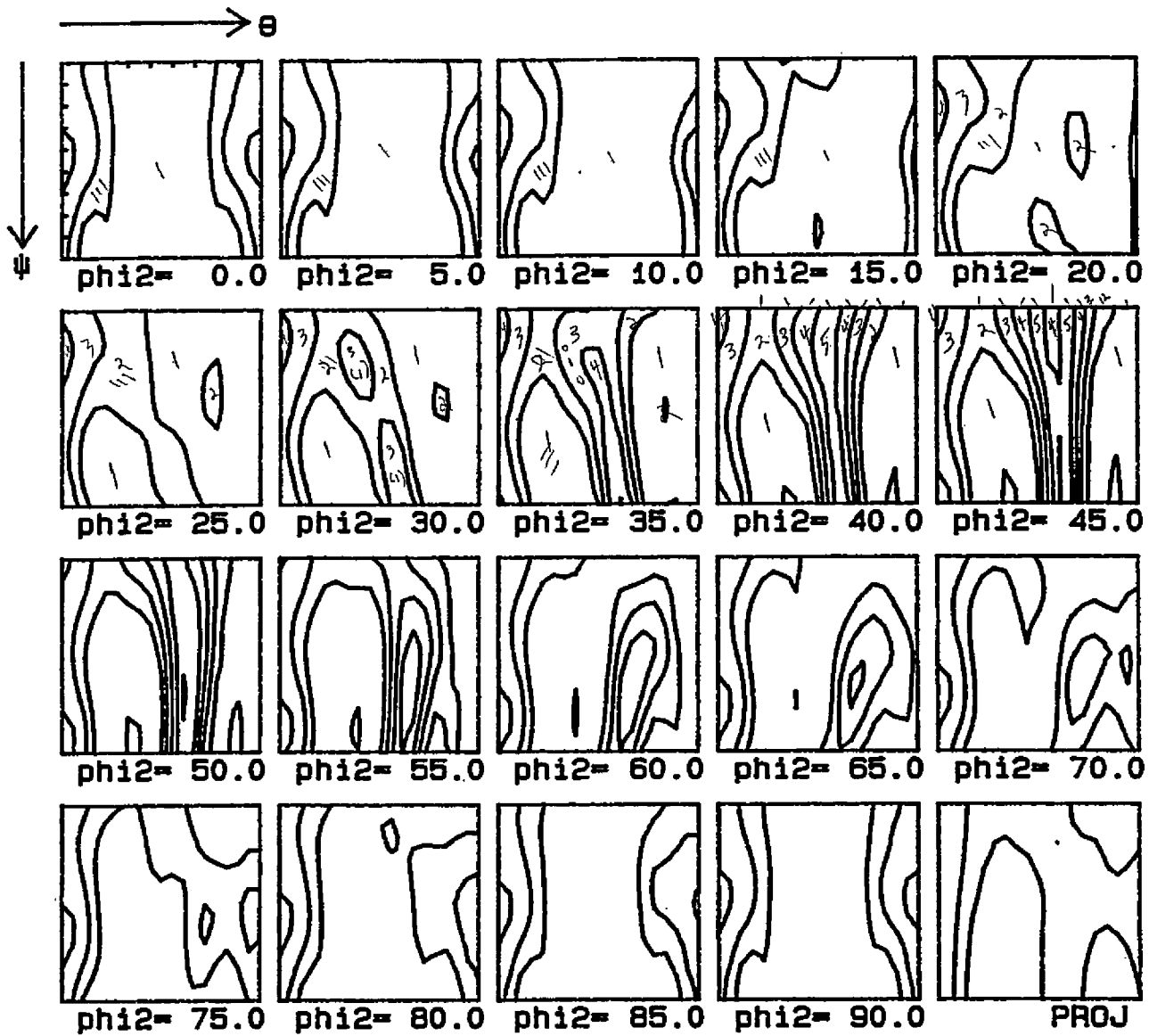
#2-CR3
recalc. pole figure 27-AUG-96
(200) Stereographic Projection
Contours at .50 1.00 1.50 2.00 2.50

27-AUG-96
. Expanded



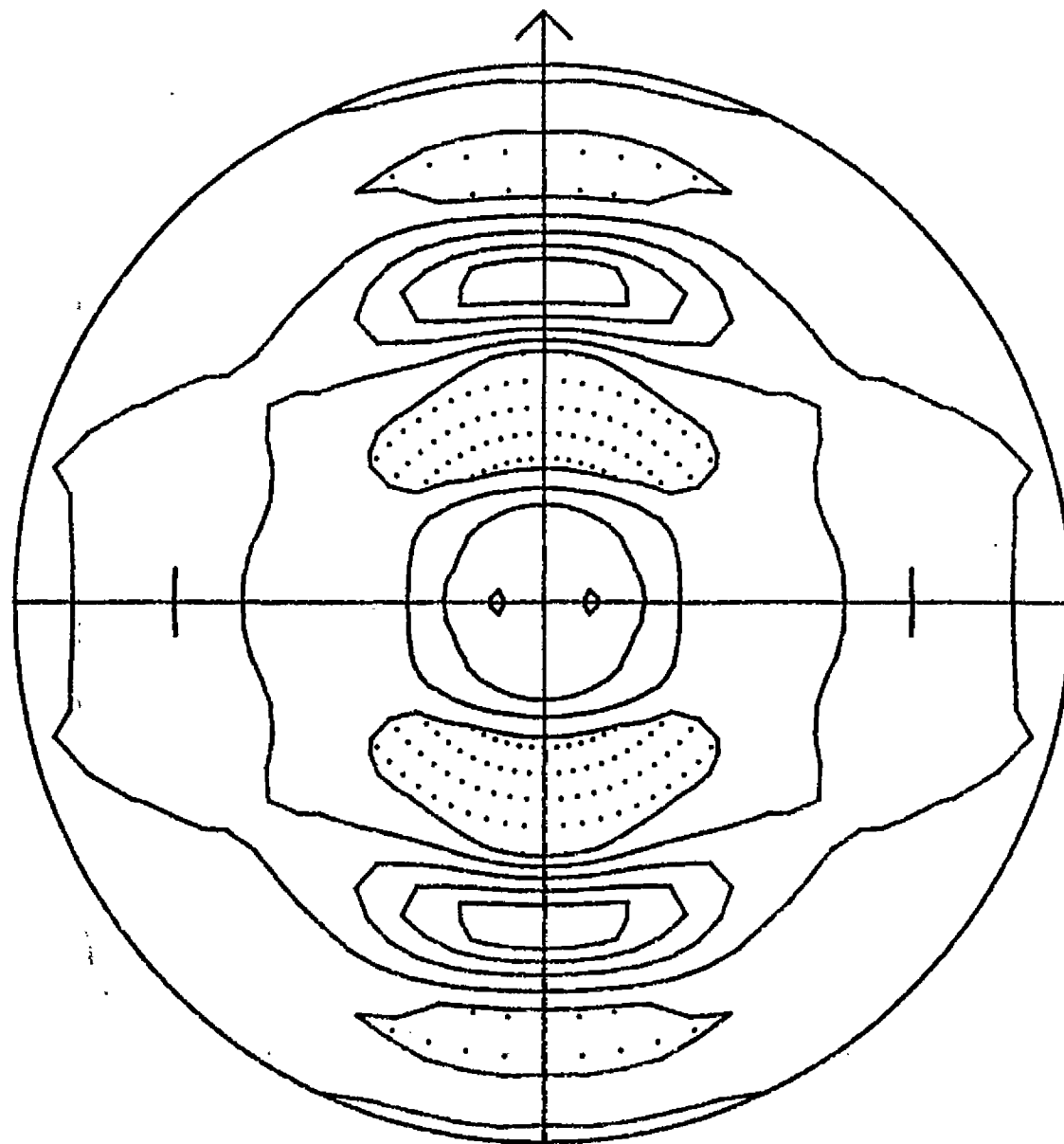
#2-CR3
recalc. pole figure 27-AUG-96
(110) Stereographic Projection
Contours at .50 1.00 1.50 2.00 2.50

27-AUG-96
. Expanded



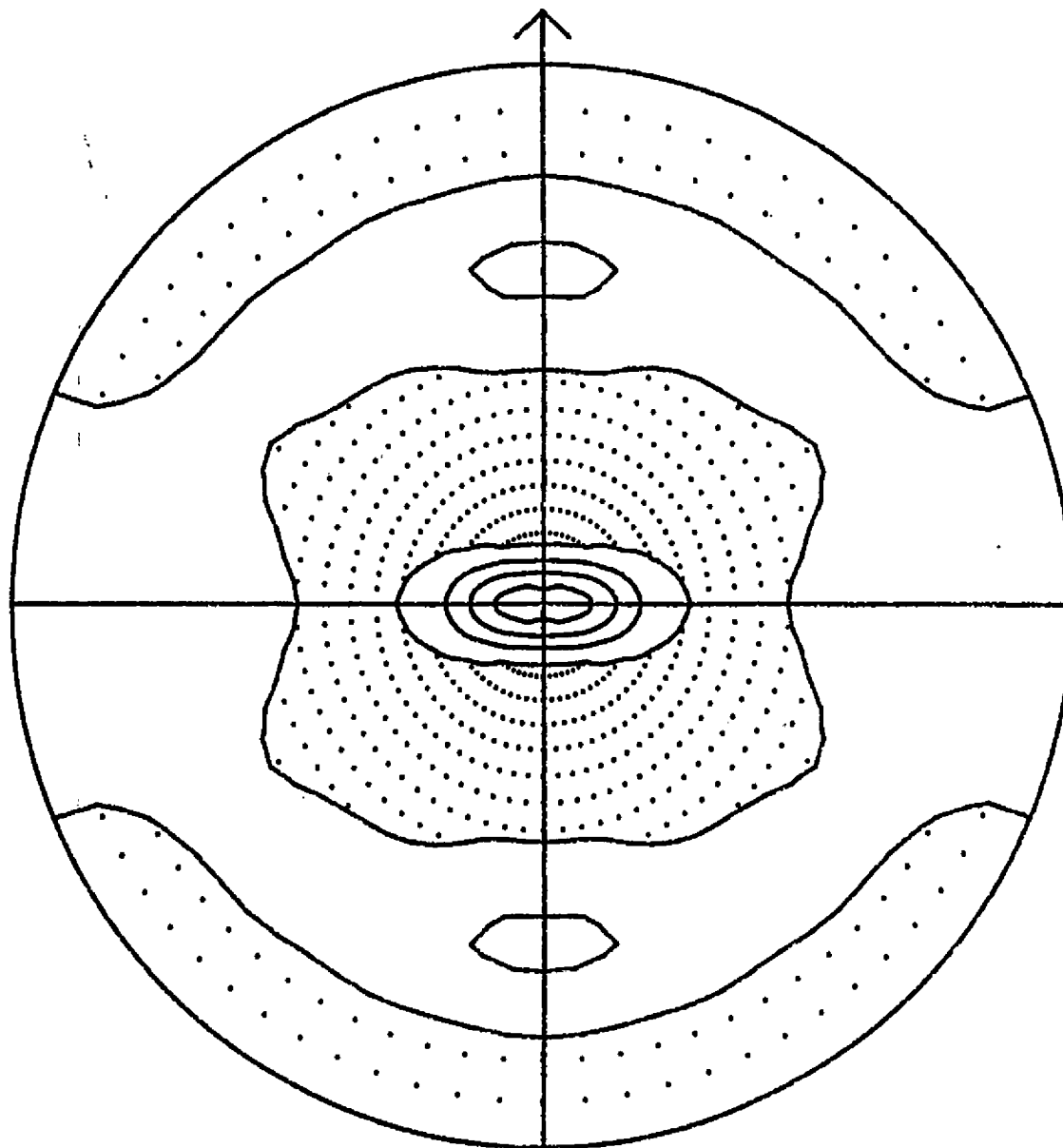
#2-CR3

Contours at 1 2 3 4 5



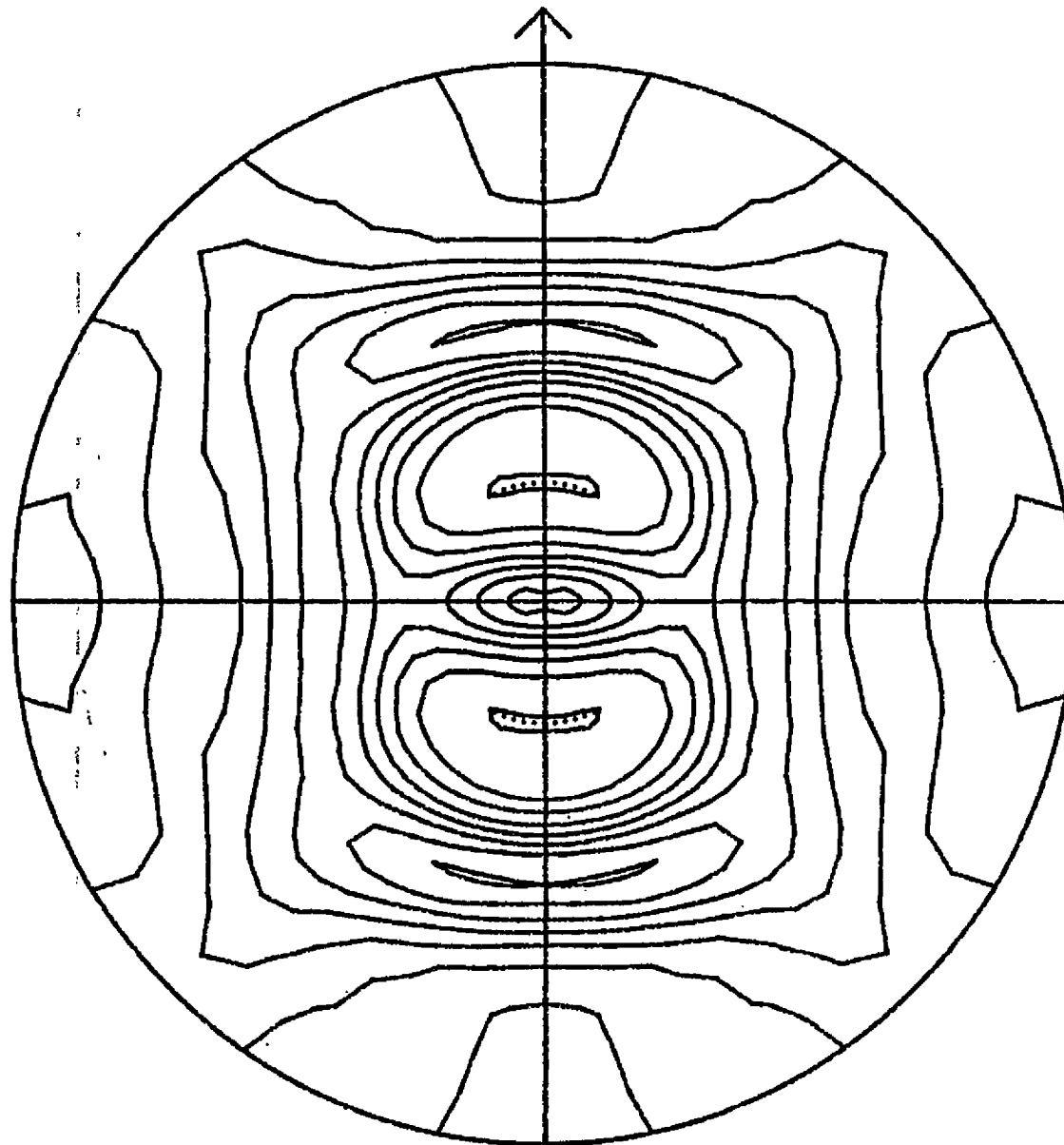
#2-CR4
recalc. pole figure 27-AUG-96
(211) Stereographic Projection
Contours at .80 1.00 1.20 1.40 1.60

28-AUG-96
, Expanded

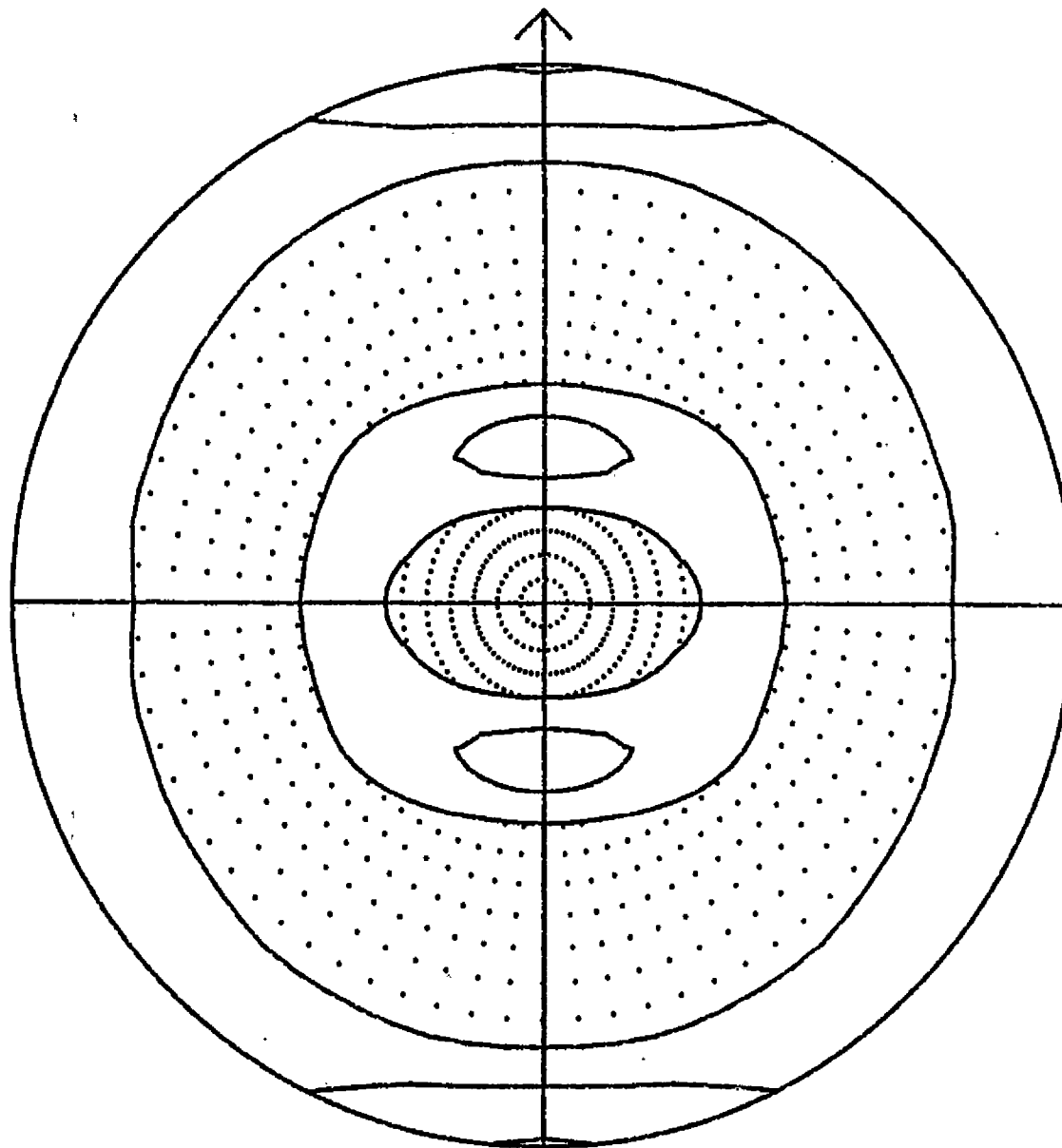


#2-CR4
recalc. pole figure 27-AUG-96
(111) Stereographic Projection
Contours at 1 2 3 4

28-AUG-96
. Expanded



#2-CR4 **28-AUG-96**
recalc. pole figure27-AUG-96 **. Expanded**
(200) Stereographic Projection
Contours at .25 .50 .75 1.00 1.25 1.50 1.75 2.00



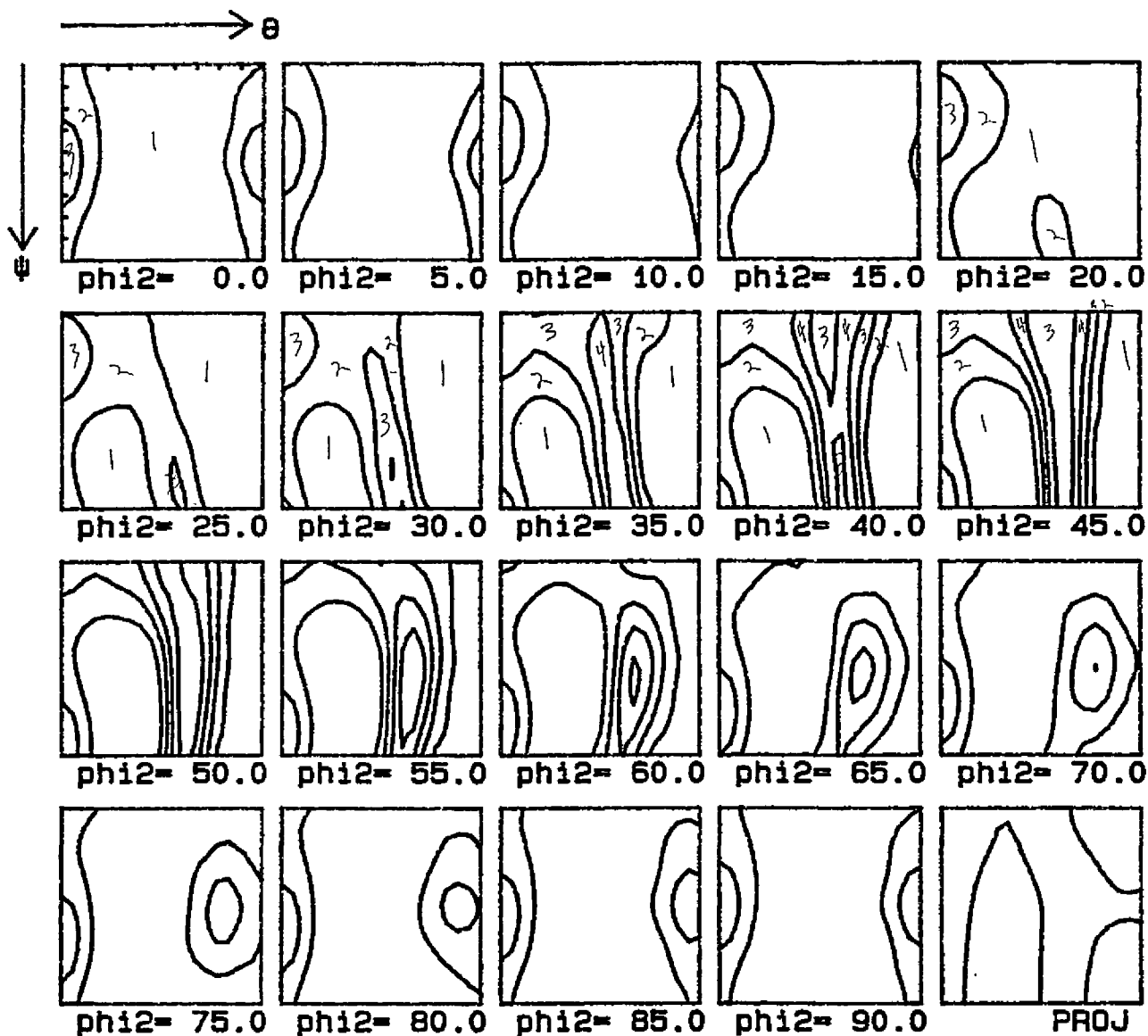
#2-CR4

recalc. pole figure 27-AUG-96
(110) Stereographic Projection

Contours at 1 2 3

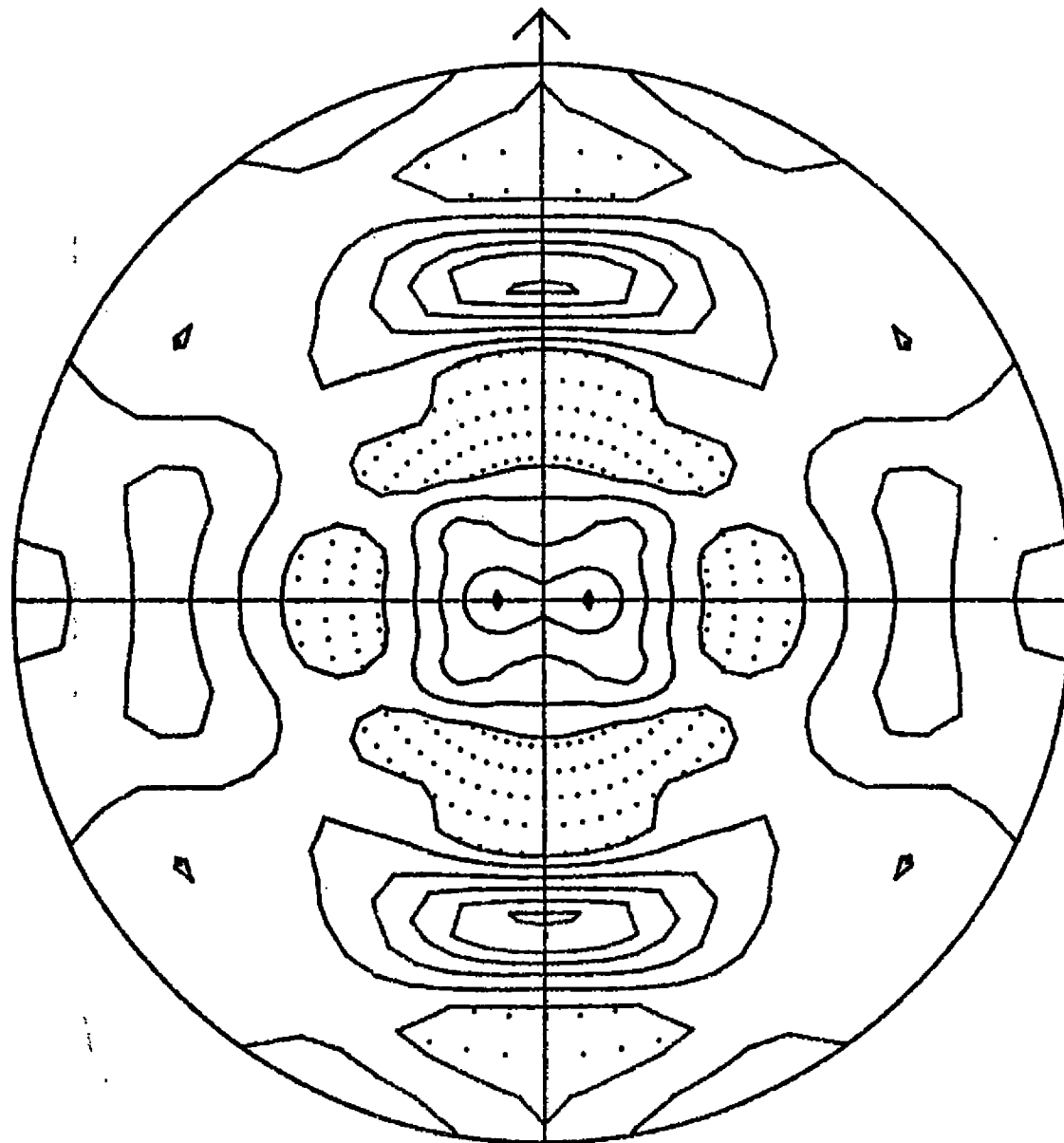
28-AUG-96

, Expanded



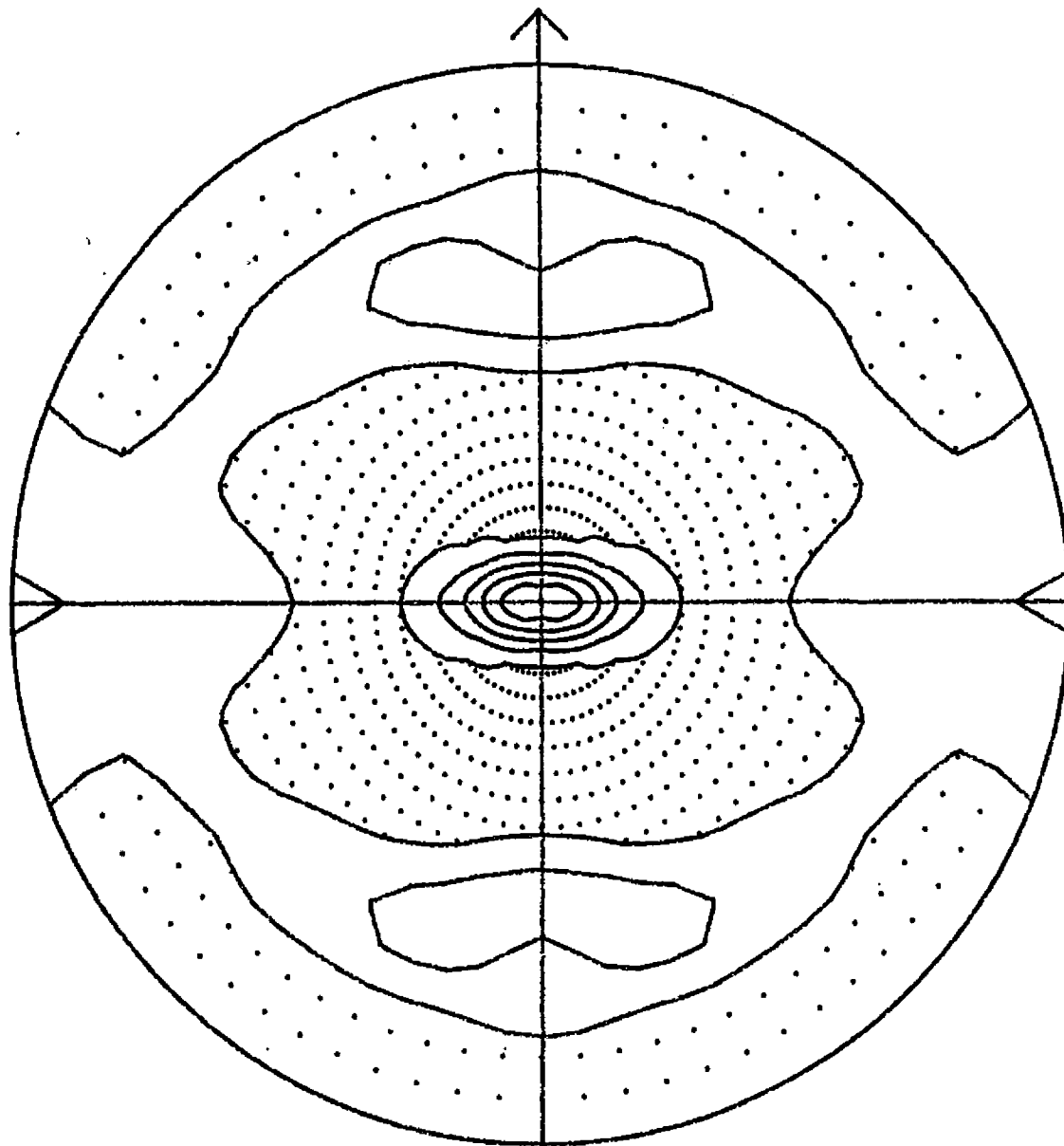
#2-CR4

Contours at 1 2 3 4



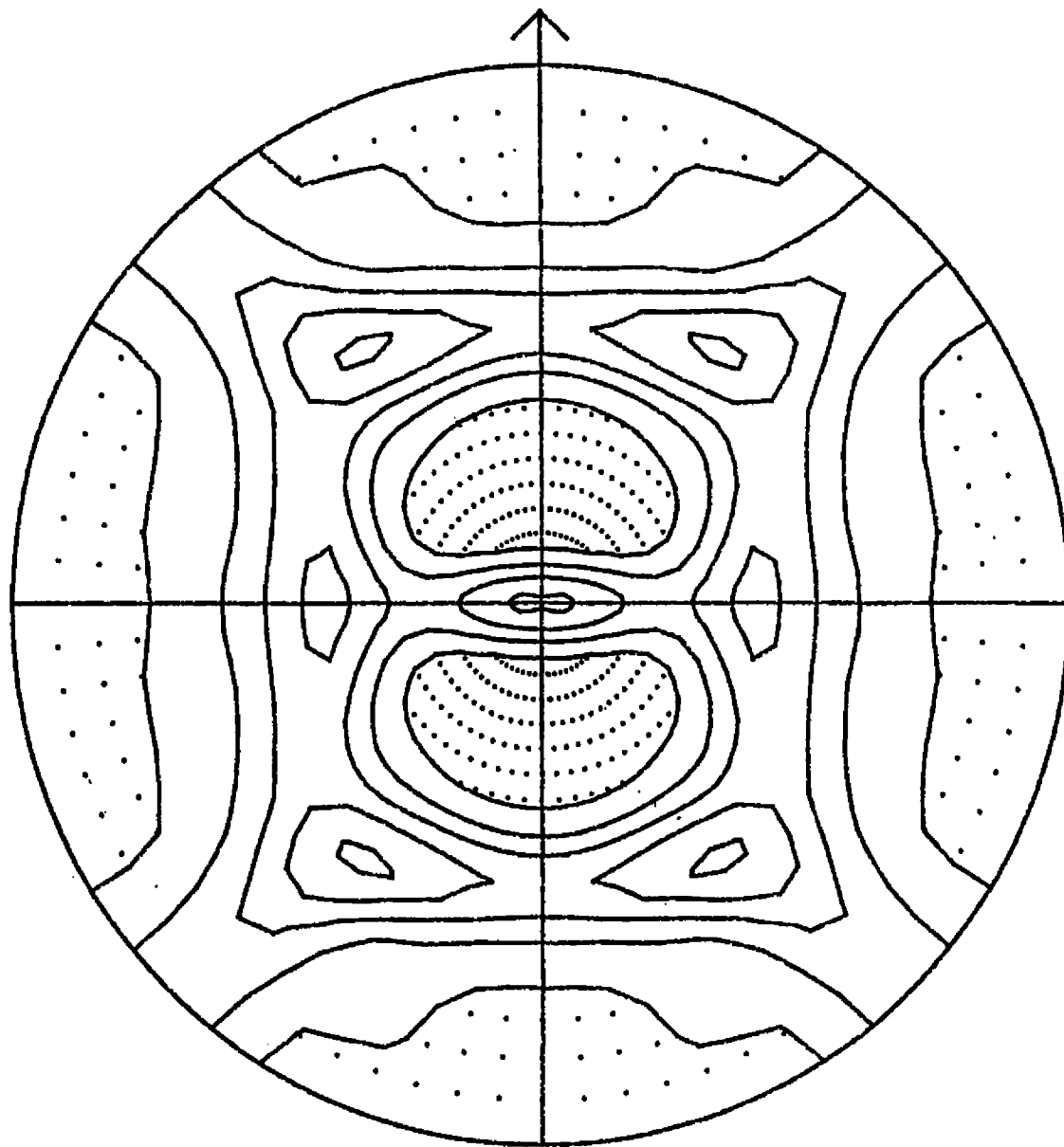
#2-CR5
recalc. pole figure 27-AUG-96
(211) Stereographic Projection
Contours at .75 1.00 1.25 1.50 1.75 2.00

28-AUG-96
, Expanded



#2-CR5
recalc. pole figure 27-AUG-96
(111) Stereographic Projection
Contours at 1 2 3 4 5

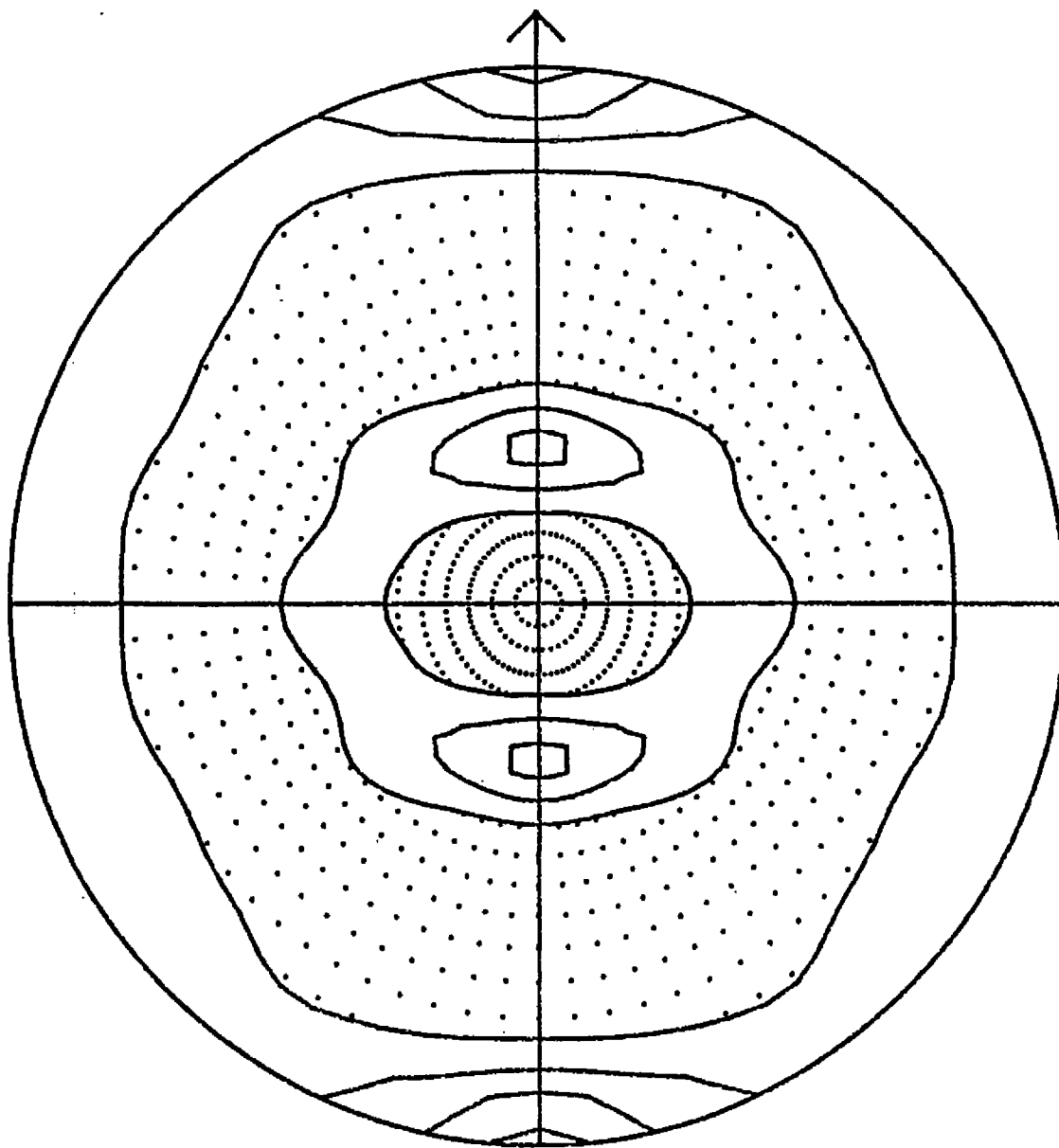
28-AUG-96
. Expanded



#2-CR5
recalc. pole figure 27-AUG-96
(200) Stereographic Projection

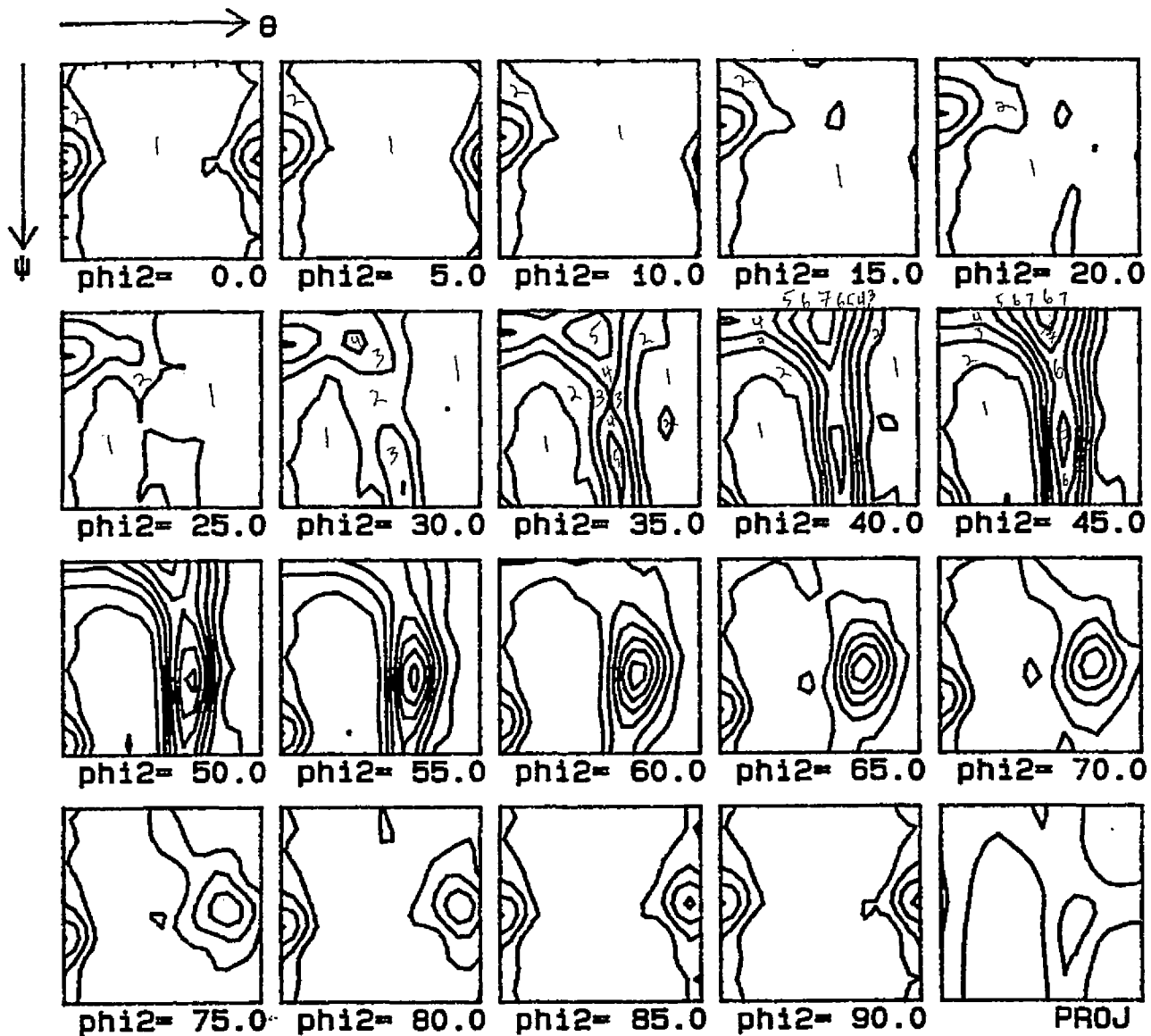
28-AUG-96
. Expanded

Contours at 50 1 00 1.50 2.00 2.50



#2-CR5
recalc. pole figure 27-AUG-96
(110) Stereographic Projection

28-AUG-96
, Expanded



#2-CR5

Contours at 1 2 3 4 5 6 7